

May 2018

Design Optimization and Control of a Fully Actuated Hexrotor UAV for Use in Aerial Manipulation Applications

Jameson Yau Sung Lee
jyskl180@gmail.com

Follow this and additional works at: <https://digitalscholarship.unlv.edu/thesesdissertations>

 Part of the [Mechanical Engineering Commons](#)

Repository Citation

Lee, Jameson Yau Sung, "Design Optimization and Control of a Fully Actuated Hexrotor UAV for Use in Aerial Manipulation Applications" (2018). *UNLV Theses, Dissertations, Professional Papers, and Capstones*. 3279.
<https://digitalscholarship.unlv.edu/thesesdissertations/3279>

This Dissertation is brought to you for free and open access by Digital Scholarship@UNLV. It has been accepted for inclusion in UNLV Theses, Dissertations, Professional Papers, and Capstones by an authorized administrator of Digital Scholarship@UNLV. For more information, please contact digitalscholarship@unlv.edu.

DESIGN OPTIMIZATION AND CONTROL OF A FULLY ACTUATED HEXROTOR UAV FOR USE
IN AERIAL MANIPULATION APPLICATIONS

By

Jameson Yau Sung Lee

Bachelor of Science – Mechanical Engineering
University of Nevada, Las Vegas
2013

A dissertation submitted in partial fulfillment
of the requirements for the

Doctor of Philosophy – Mechanical Engineering

Department of Mechanical Engineering
Howard R. Hughes College of Engineering
The Graduate College

University of Nevada, Las Vegas
May 2018

April 2, 2018

This dissertation prepared by

Jameson Yau Sung Lee

entitled

Design Optimization and Control of a Fully Actuated Hexrotor UAV for Use in Aerial
Manipulation Applications

is approved in partial fulfillment of the requirements for the degree of

Doctor of Philosophy – Mechanical Engineering
Department of Mechanical Engineering

Woosoon Yim, Ph.D.
Examination Committee Chair

Kathryn Hausbeck Korgan, Ph.D.
Graduate College Interim Dean

Kwang J. Kim, Ph.D.
Examination Committee Member

Mohamed B. Trabia, Ph.D.
Examination Committee Member

Pushkin Kachroo, Ph.D.
Examination Committee Member

Sahjendra Singh, Ph.D.
Graduate College Faculty Representative

Abstract

This work addresses the issue of controller complexity in the application of a special class of multirotor in aerial manipulation tasks. Much of the current research concerning aerial manipulation involves the modeling and control of highly coupled multirotor and manipulator systems. This is a consequence of the platform's under-actuation condition. To accommodate the rejection of arbitrary wrench disturbances brought about by the environment, multirotor must perform deliberate attitude tracking to affect forward and lateral maneuvers mid-flight. The manipulator end-effector tracking is highly affected by this, thus, their performance in general aerial manipulation is limited. To address these limitations, a special class of fully-actuated hexrotor platform was developed in this work. First, a classification system for multirotor models was introduced, and the analytical solution for all multirotor classes capable of expressing a decoupled wrench was derived. Design metrics were developed based on non-dimensional comparisons of traditional multirotor of the same form-factor. In this way, a qualitative assessment of fully-actuated multirotor performance can be compared to traditional platforms. In addition, the constraint spaces for force production and general attitude production were developed. It was shown through analysis that wrench production is inherently dependent on direction of allocation, since there are a finite number of rotors in any given multirotor build. Lastly, nonlinear control and prototype development were discussed as they relate to firmware development. The compliance of the firmware with the existing ArduPilot Mega (APM) firmware, provide a reasonable justification for commercial use.

Acknowledgements

The material presented in this work was partially supported by the National Science Foundation's (NSF) Partnership for Innovation Program, Grant No. 1430328, and a grant from the Savannah River Nuclear Solutions, LLC under contract No. 0000217400.

Table of Contents

Abstract.....	iii
Acknowledgements.....	iv
List of Tables	viii
List of Figures.....	ix
List of Symbols.....	xiv
Acronyms.....	xvi
1 Introduction	1
1.1 Motivation and Objectives.....	1
1.2 State-of-the-Art.....	1
1.2.1 Multicopter Modeling and Control	2
1.2.2 Aerial Manipulation.....	4
1.3 Contributions of this Work	6
2 Modeling of Non-Parallel Hexrotor.....	9
2.1 Motor Model.....	9
2.2 Non-Parallel and Parallel Models.....	11
2.3 Kinematics	20
2.4 Dynamics	21
2.4.1 External Effects	21
2.4.2 Production of Rotor Force and Torque.....	23
2.4.3 Dynamic Formulation.....	24

3	Physical System Design.....	26
3.1	Defining the UAV Motor Map.....	26
4	Optimization and Rotor Saturation.....	38
4.1	Power and Force Efficiency Metrics.....	38
4.2	Rotor Speed Constraints and Saturation	43
4.2.1	Arbitrary Force Constraints	43
4.2.2	Throttle, Roll, Pitch, and Yaw Constraints.....	46
4.3	Cross-span Compensation Design	70
5	Fully-Actuated UAV Control	73
5.1	Deterministic Control.....	73
5.2	The Disturbance Vector and Manipulator Dynamics.....	77
6	Prototype Development and Experimentation.....	81
6.1	Physical System Design.....	82
6.2	Flight Hardware	86
6.3	Simulation Testing.....	87
6.3.1	Simulated Hexrotor Flight and Arbitrary Wrench Production	87
6.3.2	Manipulation and Wrench Estimates Using the Iterative Newton-Euler Algorithm.....	94
6.3.3	Discrete Controller Tests using V-Rep and Application based Studies.....	97
6.4	Experimental Verification.....	98
6.4.1	Rotor Testing and Model Verification.....	99
6.4.2	Force Saturation and the Planar Efficiency Metric.....	103

6.4.3	Cross-Span Compensation Case Study.....	108
6.5	Firmware and Reference Control.....	111
6.5.1	APM Flight Stack Modification	111
6.5.2	ROS Integration and Cascade Control.....	116
7	Applications.....	124
7.1	Remote Sensing and Sample Collection	124
7.2	Payload Mass Estimation.....	128
8	Conclusions	135
Appendix A: Kinematic Definitions		137
A.1	Rotation.....	137
A.2	Euler Rates	138
Appendix B: Newton-Euler Dynamics		140
B.1	Newton’s Equation.....	140
B.2	Euler’s Equation.....	141
B.3	Iterative Newton-Euler Dynamic Formulation	142
Appendix C: Backstepping in \mathbb{R}^n		147
C.1	Backstepping 2 nd Order	147
C.2	Extension to 3 rd Order and Integration of Error	149
Bibliography		152
Curriculum Vitae		158

List of Tables

Table 2.1. All Euler frame definitions discussed in this analysis as subsets of the multirotor class m	18
Table 5.1. Denavit-Hartenberg parameters for the custom aerial manipulator	77
Table 6.1. Coefficient table for continuous time fully-actuated hexrotor reference generation.	91
Table 6.2. Experimental platform efficiency compensation for a 550 mm class hexrotor with db ratio 0.0155m, and a design tilt of $\beta = \pi/6$	109
Table 6.3. Experimental platform efficiency calculations for a 550 mm class hexrotor with propellers of db ratio 0.0155, and a design tilt of $\beta = \pi/6$	110

List of Figures

Figure 2.1. Rotor frame force and torque model (a) where rotor spin is CW. (b) where rotor spin is CCW.
 10

Figure 2.2. The general multirotor unit. This unit consists of some main body-fixed frame \mathcal{B} and some rotor frame \mathcal{M} which are transformed by some predefined static distance and rotation. 11

Figure 2.3. The quadrotor or X4-Flyer is a four-rotor unit parallel multirotor. Its frame network is shown for equiangular rotation parameters $\boldsymbol{\gamma}$ 13

Figure 2.4. The hexrotor is a six-rotor unit parallel multirotor. Its frame network is shown for equiangular rotation parameters $\boldsymbol{\gamma}$ 14

Figure 2.5. The octorotor is an eight-rotor unit parallel multirotor. Its frame network is shown for rotation parameters $\boldsymbol{\gamma}$ 15

Figure 2.6. General formulation of a nonparallel hexrotor of class $\mathcal{FS1}$. Its frame network is shown for rotation parameters $\boldsymbol{\gamma}, \boldsymbol{\alpha}, \boldsymbol{\beta}$ 19

Figure 3.1. Physical correspondence for (a) UAV throttle control. (b) UAV roll control. (c) UAV pitch control. (d) UAV yaw control. 29

Figure 3.2. Four solution sets parameterized by the tilt angle β . (a) CCW propeller spin, with $\alpha = \pi/2$. (b) CW propeller spin, with $\alpha = \pi/2$. (c) CCW propeller spin, with $\alpha = -\pi/2$. (d) CW propeller spin, with $\alpha = -\pi/2$ 37

Figure 4.1. Projection of force constraints for a fully-actuated hexrotor. 45

Figure 4.2. Isometric view of the hexrotor attitude speed constraint space. 48

Figure 4.3. Top view of the hexrotor attitude speed constraint space. 49

Figure 4.4. (a) Front view of the hexrotor attitude speed constraint space. (b) Side view of the hexrotor attitude speed constraint space. 49

Figure 4.5. Isometric view of the hexrotor attitude speed constraints. Roll/pitch constraint plane for a 15% yaw to throttle offset command.	50
Figure 4.6. Top view of the hexrotor attitude speed constraints. Roll/pitch constraint plane for a 15% yaw to throttle offset command.	51
Figure 4.7. Roll/pitch constraint plane for a 15% yaw to throttle offset command. (a) Front view of the hexrotor attitude speed constraints. (b) Side view of the hexrotor attitude speed constraints.	52
Figure 4.8. Isometric view of the hexrotor attitude speed constraints. Roll/pitch constraint plane for a -15% yaw to throttle offset command.	53
Figure 4.9. Top view of the hexrotor attitude speed constraints. Roll/pitch constraint plane for a -15% yaw to throttle offset command.	54
Figure 4.10. Roll/pitch constraint plane for a -15% yaw to throttle offset command. (a) Front view of the hexrotor attitude speed constraints. (b) Side view of the hexrotor attitude speed constraints.	54
Figure 4.11. Isometric view of the hexrotor attitude speed constraints. Roll/pitch constraint plane for a 33% yaw to throttle offset command.	55
Figure 4.12. Top view of the hexrotor attitude speed constraints. Roll/pitch constraint plane for a 33% yaw to throttle offset command.	56
Figure 4.13. Roll/pitch constraint plane for a 33% yaw to throttle offset command. (a) Front view of the hexrotor attitude speed constraints. (b) Side view of the hexrotor attitude speed constraints.	57
Figure 4.14. Isometric view of the quadcopter attitude speed constraints.	59
Figure 4.15. Top view of the quadcopter attitude speed constraints.	60
Figure 4.16. (a) Front view of the quadcopter attitude speed constraints. (b) Side view of the quadcopter attitude speed constraints.	60
Figure 4.17. Projection of force constraints for a fully-actuated octocopter.	61
Figure 4.18. Isometric view of the octocopter attitude speed constraints.	62
Figure 4.19. Top view of the octocopter attitude speed constraints.	63

Figure 4.20. (a) Front view of the octocopter attitude speed constraints. (b) Side view of the octocopter attitude speed constraints.	63
Figure 4.21. Projection of force constraints for a fully-actuated decacopter.	65
Figure 4.22. Isometric view of the decacopter attitude speed constraints.....	66
Figure 4.23. Top view of the decacopter attitude speed constraints.	66
Figure 4.24. (a) Front view of the decacopter attitude speed constraints. (b) Side view of the decacopter attitude speed constraints.	67
Figure 4.25. Projection of force constraints for a fully-actuated duodecacopter.	68
Figure 4.26. Isometric view of the duodecacopter attitude speed constraints.....	69
Figure 4.27. Top view of the duodecacopter attitude speed constraints.	69
Figure 4.28. (a) Front view of the duodecacopter attitude speed constraints. (b) Side view of the duodecacopter attitude speed constraints.	70
Figure 4.29. Approximate cross-span model compensation isoclines as a function of design tilt.....	72
Figure 5.1. Example manipulator workspace and expected position of CG with varying payloads.....	78
Figure 5.2. Static hover considerations for manipulator configurations.	79
Figure 5.3. Decoupled control diagram for an aerial manipulator.	80
Figure 6.1. UNLV indoor flight volume equipped with an Optitrack motion capture system.	81
Figure 6.2. UNLV outdoor flight volume used for flight experiments requiring GPS localization.....	82
Figure 6.3. Completed fully-actuated hexrotor prototype.....	83
Figure 6.4. Custom motor mounts built with a design tilt of $\beta = \pi/6$	84
Figure 6.5. Manipulator mounting configuration.....	85
Figure 6.6. Side view of manipulator and lower mounting hardware.....	85
Figure 6.7. Real-time servo controller Arbotix-M, and the mounting and power distribution board.....	86
Figure 6.8. Top view of the fully-actuated hexrotor. Peripheral and controller hardware shown.	87
Figure 6.9. Completed aerial manipulator simulation in the Simulink environment.	88
Figure 6.10. UAV dynamic and controller simulation subsystem.	89

Figure 6.11. Primitive visualization of the fully-actuated hexrotor aerial manipulation platform in the Simscape Multibody environment.	90
Figure 6.12. Simulated position and attitude of the fully-actuated hexrotor with no manipulator.	92
Figure 6.13. Simulation filtered and saturated rotor effort.	93
Figure 6.14. Control effort of the simulated hexrotor.	94
Figure 6.15. Primitive visualization of the manipulator system using Simscape Multibody, and the final prototype manipulator system.	95
Figure 6.16. Simscape Multibody base reaction forces and torques developed from the physical simulation of the aerial manipulator.	96
Figure 6.17. Iterative Newton-Euler algorithm estimation of base reactions.	96
Figure 6.18. Error of the iterative Newton-Euler algorithm estimate.	97
Figure 6.19. Discrete controller testing in the V-Rep environment.	98
Figure 6.20. T-Motor MN4006 AntiGravity Brushless motor and Multistar Timber T-Style Propeller 13x4.4 mounted to an ATI mini-45 6-axis F/T sensor.	99
Figure 6.21. Measure F/T data for the MN4006 and Multistar Timber T-Style Propeller 13x4.4 pairing	101
Figure 6.22. Experimental Pixhawk flight controller servo timing correlation to rotor speed using an MN4006, Multistar Timber T-Style Propeller 13x4.4, X-Rotor 40A ESC, and 6S Lipo Battery after Calibration.	103
Figure 6.23. Experimental fully-actuated force/torque setup. An ATI min-45 6 axis F/T sensor was used to measure the prototype’s force/torque profiles.	104
Figure 6.24. Side view of the airframe rigidly attached to the mini-45 6 axis ATI F/T sensor.	104
Figure 6.25. Forward force saturation test. All forces recorded.	105
Figure 6.26. APM flight stack saturation test measured force outputs.	107
Figure 6.27. Evaluation of scaled efficiency metric in the APM flight stack test.	108
Figure 6.28. Torque efficiency metrics as a function of design β	111
Figure 6.29. Hexrotor flight testing	113

Figure 6.30. Fully-actuated hexrotor flashed with the custom APM firmware in STABILIZE mode.	114
Figure 6.31. Unmixed force/torque time history for the fully-actuated hexrotor in STABILIZE.	114
Figure 6.32. Fully-actuated hexrotor flashed with the custom APM firmware in FULLY_ACT mode...	115
Figure 6.33. Unmixed force/torque time history for the fully-actuated hexrotor in FULLY_ACT mode.	116
Figure 6.34. An example messaging diagram in simple ROS implementations.	117
Figure 6.35. General framework for system control using ROS. Since ROS is not a real-time system, it cannot provide any stability guarantees in implementation.	118
Figure 6.36. Early development of the prototype and localization using a camera.	119
Figure 6.37. QR code detection and pose estimation of the target.	119
Figure 6.38. Cartesian control of a 3R manipulator. The manipulator is controlled via reference command of end-effector tip position.	120
Figure 6.39. Closed-loop parallel hexrotor aerial manipulation test.	121
Figure 6.40. Nonparallel hexrotor flight test towards aerial manipulation.	122
Figure 6.41 Position and orientation of the fully-actuated hexrotor in a closed-loop test.	123
Figure 7.1. Octocopter aerial manipulator platform setup with plug-and-play sensor and manipulator peripherals.	125
Figure 7.2. Sensor and manipulator communications network for the octocopter aerial manipulator.	125
Figure 7.3. Manipulator power distribution and reference generation for the end-effector.	126
Figure 7.4. Custom GUI for remote control of the octocopter aerial manipulator.	127
Figure 7.5. Flight simulation of UAV position localization and control using a moving color coded target.	127
Figure 7.6. Camera and overhead view of the localization and positioning simulation.	128
Figure 7.7. Center of mass estimation simulation.	133

List of Symbols

X, Y, Z	principle Cartesian axes
x, y, z	global position in earth frame Cartesian space
u, v, w	body-fixed velocity in Cartesian space
ϕ	global roll orientation about X
θ	global pitch orientation about Y
ψ	global yaw orientation about Z
p, q, r	body-fixed angular velocity
m^*	UAV mass
J^*	UAV inertia
\mathcal{B}	The UAV body-fixed frame
\mathcal{E}	The inertial frame
\mathcal{M}	Motor frame
\mathcal{J}	Euler Z motor definition of a parallel multirotor
\mathcal{S}	Euler ZZX and ZZY motor definition of a nonparallel multirotor
\mathcal{Q}	Euler ZXY , ZXZ , ZYX , and ZYZ motor definition of a nonparallel multirotor

\mathcal{K}	Euler ZX and ZY motor definition of a nonparallel multirotor
\mathcal{F}	Multirotor class descriptor

Acronyms

UAV	Unmanned Aerial Vehicle
BFF	Body-Fixed Frame
BEMT	Blade Element Momentum Theory
ESC	Electronic Speed Controller
PWM	Pulse Width Modulation
APM	ArduPilot Mega
HAL	Hardware Abstraction Layer
V-TOL	Vertical Take-Off and Landing
DOF	Degree of Freedom
LQR	Linear Quadratic Regulator
COM	Center of Mass

1 Introduction

In this section, the motivations and objectives of this work were presented within the context of the state-of-the-art in implementation, modeling and control of multirotor unmanned aerial vehicles (UAV). The intended contributions of this work were then introduced as they relate to aerial manipulation and airframe design of a special class of UAV.

1.1 Motivation and Objectives

The objective of this research was the development of a novel model and flight stack for a special class of fully-actuated multirotor for use in aerial manipulation tasks. Aerial manipulation is a field of study which has seen limited advances in recent years due in part to the prolific use of underactuated multirotor UAV in aerial manipulation studies. Traditional multirotor are affordable, require little pilot training, possess vertical take-off-and-landing (V-TOL) capabilities, and are backed by a massive developer community, thus, they make a convenient choice for platform development. This convenience comes at a cost, however, as under-actuated airframes often require complex and robust control strategies to support aerial manipulation functionality. In addition, the stability restrictions imposed on the system by under-actuation limit the range of viable use-cases for a multirotor aerial manipulator. The motivation of this work is to provide a reasonable solution to the aerial manipulation problem without the introduction of non-reproducible overly complex design elements. This was achieved by taking advantage of the large developer code base of traditional multirotor, modifying it, and developing a fully-actuated compliant flight stack.

1.2 State-of-the-Art

The state-of-the-art in small UAV has seen great advances in the past decade. Transistor technologies have improved and seen massive form factor and price reductions, which have in-turn promoted accessibility of small UAV to the public at large. In this section the history of development and implementation of these

small UAV are introduced to provide some context for the study of the special class of UAV developed in this work. Throughout this section control and design strategies of several UAV are presented and discussed as they relate to aerial manipulation.

1.2.1 Multirotor Modeling and Control

One of the earliest known publications on modern multirotor UAV can be found in [1]. In this work a model for a four-rotor V-TOL aerial vehicle known as an X4-flyer was described. The construction of the X4-flyer was that of a rigid cross frame, which possessed four fans. The motor model was simplified from blade element momentum theory (BEMT), where motor frame thrust and drag are described as proportional mappings of square rotor speed. The rigid-body dynamics in this work utilized the Newton-Euler formulism, and the control architecture was based on Lyapunov principles in the form of a backstepping scheme. A contemporary article by [2] developed a similar model for the X4-flyer, where a prototype was fabricated and tested. Gyroscopic, gravitational, and rotor effects were considered forcing functions in the formulation of the UAV rigid-body dynamics, and the model was linearized before developing a controller. In the described experiment a double lead compensator was proposed.

The introduction of these nonlinear models and experiments prompted more studies into the behavior of the X4-flyer using different control strategies. [3] compared a sliding-mode controller to a backstepping controller and found the robust sliding-mode controller to be of average quality in performance favoring the backstepping scheme. The author went on to write a fairly comprehensive thesis further developing the model of the X4-flyer [4].

Some authors focused on improving certain aspects of sensing and feedback. A quaternion based attitude controller was introduced by [5]. While there certainly is merit in the elimination of singularity states present in the typically used Euler rotation schemes, Euler equivalent orientation angles are required for state feedback in practical application. Thus, on some user-interface level, conversion into equivalent Euler

roll, pitch, and yaw was necessary. Typical use of multirotor require roll/pitch regulation, thus, the justification for this type of control requires more analysis as stated by the author.

Control strategies were not the only focus of research in the robotics community. Improvements to the multirotor model were introduced by [6] with the addition of propeller flex in the motor model. The author sought to identify what role propeller dynamics played in the performance of the dynamic model by expanding on the simplified one of [1] and his contemporaries. The author provided a clear case study for its use, while admitting that the platform is certainly controllable with the simplified model. Another model based contribution to the field was that of [7], who introduced a novel control allocation scheme for developing over-actuation in UAV flight. The study employed a hexrotor, and provided useful insight into the over-actuation condition of UAV. Hexrotor as described by the author are considered over-actuated concerning the 4DOF subsystem of throttle, roll, pitch, and yaw, while remaining under-actuated in general 6DOF wrench production. Essentially, the developed airframe improved controllability within the limited states of throttle, roll, pitch, and yaw. The paper discussed both the classical method of the Moore-Penrose pseudo-inverse [8], and introduced a novel weighted pseudo inverse method.

As technology advanced and implementation became more feasible, many studies began to focus on how these UAV could be used in the field. In 2008 the first known instance of a tethered UAV used in the field was described in [9]. A parking garage had collapsed in a plaza in Jacksonville, Florida. What the study found was that the control techniques used for this specific tethered UAV were not sufficient for close urban deployment. The navigation and sensing technology was simply not advanced enough to provide site personnel with reliable performance. Another application of UAV being used in the field was introduced by [10] for oil spill detection at sea. One major advantage of small V-TOL aircraft is their ability to fly tethered to a slow-moving object such as a ship or ground vehicle. This provides certain advantages concerning restricted airspaces. This work focuses on the development of a coupled model for tether and UAV flight dynamics. As was demonstrated by the results of [9], tethering of small UAV imparts major

instabilities on flight performance of UAV in hover. This result is informative of the effect of environment interactions on under-actuated multirotor.

To improve implementation strategies for multirotor deployments, measures for motor failures were also examined in [11]. In this work, an LQR controller was tested to explore recovery of attitude from a total failure of one or more rotors. The strategy discussed would allow a multirotor to safely land via rotation about some fixed axis measured with respect to the body-fixed frame in the event of such a failure. Unlike helicopters and fixed-wing aircraft, multirotor, at the time of this work's publication, had no method of stabilization after rotor failure. The implications of this work were extremely significant to practical field implementation of multirotor UAV, and robust close quarters deployment.

The work of [12] provided successful results on collaborative UAV in the field. This work demonstrated the capability of multirotor to explore and map a building which had been structurally compromised. Rather than sending in human technicians, multirotor were deployed to inspect the site. The implemented UAV were capable of close urban and indoor deployment. Aerial manipulation requires extreme precision to accomplish dexterous manipulation tasks, and the quality of indoor flight is essential to the development of a successful aerial manipulation system.

1.2.2 Aerial Manipulation

Active manipulation of the environment requires careful consideration concerning under-actuated AV. The study performed by [13] considers an adaptive control scheme for a slung load helicopter. Slung load applications are a very practical control problem often used in the moving of cargo. While not the focus of this study, much work has been done regarding slung loads in overhead crane applications. In [13], a load estimator is used to develop compensation and increase damping of load oscillations for a helicopter in slung load.

The classical usage of helicopter airframes for slung load applications was applied to multirotor UAV in [14]. In this work, the development of a control strategy to reduce oscillations in a slung load was successfully achieved through a coupled dynamic model. Authors such as [15] also investigated the effects of unknown center of mass (COM) and external disturbances on UAV flight, and presented an adaptive scheme to compensate for the uncertainties. Concerning environment interaction, the behavior of UAV under uncertain disturbances must be well understood for successful implementation. Along this line of work, [16] used an adaptive estimator to predict aerodynamic parameters on-line, while not specifically related to environment interactions. This type of control strategy is useful for identifying COM locations for multibody systems as is the case with dexterous aerial manipulator platforms.

Physical interactions with the environment using a UAV were discussed in [17]. In this work, a quadrotor was used to explore multirotor response when interacting with a wall. A mechanical frame was used to stabilize the platform as it expressed force on a test wall. This test showed that it was possible to apply directional force on an object using a multirotor. The work of [18] furthered the study of environment interactions with multirotor by introducing a multirotor controller capable of stabilizing a quadrotor as it grasped an object directly underneath it with a claw. Similarly a helicopter was used to grasp an object from the air in the work described by [19] and [20]. The uncertainties of the placement of the COM were discussed as they relate to stability in these works, respectively.

Aerial manipulation as it pertains to dexterous grasping was discussed in [21] and [22]. The goal of the introduced design was to provide feasible design metrics for dexterous grasping of objects using a manipulator. This work introduced several core concepts directly relevant to the study of fully-actuated hexrotor design. In close quarters UAV are subject to disturbances such as ground effects, and a manipulator would be necessary to grasp objects, since fine motion control of the airframe is not practical. Stable coupled dynamics are necessary and visual servoing is practical as described in this work.

Deployment of aerial manipulators is not an easily achieved task. Rather than focus on the flight performance of the coupled system, authors such as [23] and [24] explored control strategies for the manipulator within a controlled environment, mounting the manipulators to rigid frames. The focus of these studies was the development of hybrid interaction control strategies for aerial manipulator use.

Forwarding the study of experimental aerial manipulation deployment was works such as [25]. In this paper a quadrotor was built with an attached manipulator, and the state response was observed. The contribution of this work was qualitative in nature. As stated by the author, the controller performance was not addressed in this study, rather the feasibility of deployment.

Works such as [26] and [27] tackled the control problem of deployable aerial manipulators by deriving a coupled model for use in the control of a helicopter and quadrotor aerial manipulator, respectively. Adaptive control schemes were introduced in [28] to stabilize the UAV to combat shifts to the model moment of inertia caused by manipulator action. These efforts describe a few of many works on the development of more robust control methods to stabilize under-actuated multirotor aerial manipulator systems.

1.3 Contributions of this Work

This work seeks to expand upon existing flight stacks and provide a compatible fully-actuated airframe. Through the analysis provided in this paper, an analytical solution to the design of such a platform was outlined. The novelty of this design lies in its ability to express full-actuation in flight, while remaining compatible with existing under-actuated control architecture. It accomplishes this through deliberate static rotations of the rotors about the body-fixed frame. Rotation of rotor axes in multirotor applications have been explored in works such as [29], but they had not been expressly considered for the purpose of achieving full-actuation at that time. In [29] a multirotor called a triangular quadrotor was introduced. In this work three rotors were mounted equiangularly about an airframe, where one rotor was used to steer the platform. To improve hover efficiency, a large fourth propeller was added to the center of the platform to

contribute most of required lift. This approach to multirotor airframe development challenged traditional actuation modes of multirotor UAV. A tri-copter controller was also introduced in [30], where the platform achieved forward and lateral force expressions via thrust vectoring. This platform lacked the ability to generate an arbitrary wrench, thus it may not be well-suited to aerial manipulation. A contemporary of this work can be found in [31], where more details on thrust vectoring of a tri-copter are provided.

The first fully-actuated hexrotor was introduced in [32]. The hexrotor, much like, tri-copters and the discussed triangular quadcopter achieved actuation via skewed orientation of the rotor axes. One key assumption made in this work is that the hexrotor motors were assumed to be reversible. While this constraint eliminates most saturation concerns, the reversibility of rotor rotation is not typical of UAV builds. This is due to efficiency losses caused by propeller design. Each propeller blade acts as a wing in the development of aerodynamic properties, and a bidirectional propeller must be fabricated with similar aerodynamic properties concerning lift and drag given reversible directions of air flow. This work was extremely innovative, and developed the first concept of a fully-actuated hexrotor. The first reported fully-actuated hexrotor prototype was built by [33], though no flight data was provided. The concept of dexterous flight was introduced in this work, and provided a template for an ideal candidate aerial manipulator platform, one which could produce an arbitrary wrench to maintain stability in flight.

An altogether novel design of fully-actuated hexrotor was introduced in [34]. The concept design developed a dexterous airframe. The airframe, however was configured such that it shared no commonality with traditional multirotor. This required custom firmware development unlike any stack that could be described as native to the UAV developer community, making its implementation a difficult prospect. A similar multirotor build was discussed in [35], where the airframe configuration was completely novel in design.

The dexterous multirotor designs developed in [32] and [33] were, at the time, exploratory in nature. No airframe like it had existed in the literature, thus, their contributions were extremely innovative. It wasn't until very recently that deeper analyses began to appear concerning the flight characteristics of this platform.

[36] discussed the design and optimization of the fully-actuated hexrotor model using a genetic algorithm. In this work Euler rotations were performed on the rotors, which were placed as they are in traditional multirotor designs, to achieve arbitrary rotor axis skew. The optimization concluded that their design could achieve full-actuation along optimized desired trajectories. Contemporary work by [37] developed a tilted hexrotor model which angled each rotor inwards towards the origin of the body-fixed frame. A commercial example of this kind of design can be seen in the DJI S1000+. This work also claims full-actuation of the platform through model based analysis of rotor tilt. As will be shown in the analysis presented in this paper, designs such as these provide a limited scope of metric based evaluations of fully-actuated hexrotor performance.

In the presented research, a generalized design methodology for fully-actuated hexrotor was developed. It was shown that there are a finite set of fully-actuated hexrotor designs which can produce an arbitrary decoupled wrench, and the form of these designs were developed using a novel analytical model. The design of the firmware also provides full compatibility with existing control architecture, thus complementing works such as [38], which describe a transformable hexrotor capable of both traditional and fully-actuated flight. This work seeks to legitimize the use of the exploratory fully-actuated hexrotor design in the commercial realm, and provide reasonable justification for its use in dexterous aerial manipulation applications.

2 Modeling of Non-Parallel Hexrotor

The design and analysis of the multirotor model was broken into several sections in this chapter. In the first section a generic motor model was developed. Multirotor do not classically incorporate airfoil components in their design, thus actuation is dependent almost exclusively on propeller dynamics. The second section develops the concept of parallel and nonparallel multirotor design. The section classifies several model types to provide context and a sensible methodology for analysis of specific nonparallel multirotor. Using the defined classifications, the UAV kinematic and dynamic model of a special class of hexrotor was then derived and summarized in the final section.

To clarify, vector frame notation in this section is defined as it is in [39], where a vector defining the position of some point A is denoted ${}^A\mathbf{v}$, where the point of interest is described with respect to an origin frame. A vector describing the point A measured with respect to some arbitrary frame $\{B\}$, was denoted explicitly by ${}^B\mathbf{v}_A$. For descriptions of Euler and quaternion rotations refer to Appendix A.

2.1 Motor Model

Propeller dynamics have been well studied in the literature concerning UAV implementation using blade element momentum theory (BEMT). A detailed description of BEMT for use in developing a UAV motor model was provided in [40], thus only a brief overview was provided here for context. In this analysis, the motor frame force ${}^{\mathcal{M}}\mathbf{F}$ and torque ${}^{\mathcal{M}}\boldsymbol{\tau}$ was given by

$$\begin{aligned} {}^{\mathcal{M}}\mathbf{F} &= [0 \quad 0 \quad b\omega_i^2]^T, \\ {}^{\mathcal{M}}\boldsymbol{\tau} &= [0 \quad 0 \quad q_id\omega_i^2]^T, \end{aligned} \tag{2.1}$$

where \mathcal{M} denotes an arbitrary motor frame of the i^{th} rotor belonging to a UAV, b is known as the thrust coefficient $\left(\frac{Ns^2}{rad^2}\right)$, d is the drag coefficient $\left(\frac{Nm^2}{ra^2}\right)$, and ω_i is the i^{th} rotor angular velocity $\left(\frac{rad}{s}\right)$

expressed as a component of propeller angular velocity vector defined by ${}^{\mathcal{M}}\boldsymbol{\omega} = [0 \ 0 \ \omega_i]^T$. The variable $q_i = -\text{sgn}(\omega_i)$ was introduced here to quantify rotor spin. The use of this notation and model was common in early works on quadrotor modeling [1], [2], and persists in current works [3], [7], [15], [11], [16].

A visual representation of this motor model is given in Figure 2.1, where both CW and CCW rotor configurations are presented for spin parameters $q_i = -1$ and $q_i = 1$, respectively. Rotor thrust and drag present colinearly along ${}^{\mathcal{M}}\mathbf{Z}$, while the torque vector ${}^{\mathcal{M}}\boldsymbol{\tau}$ must oppose the velocity vector ${}^{\mathcal{M}}\boldsymbol{\omega}$.

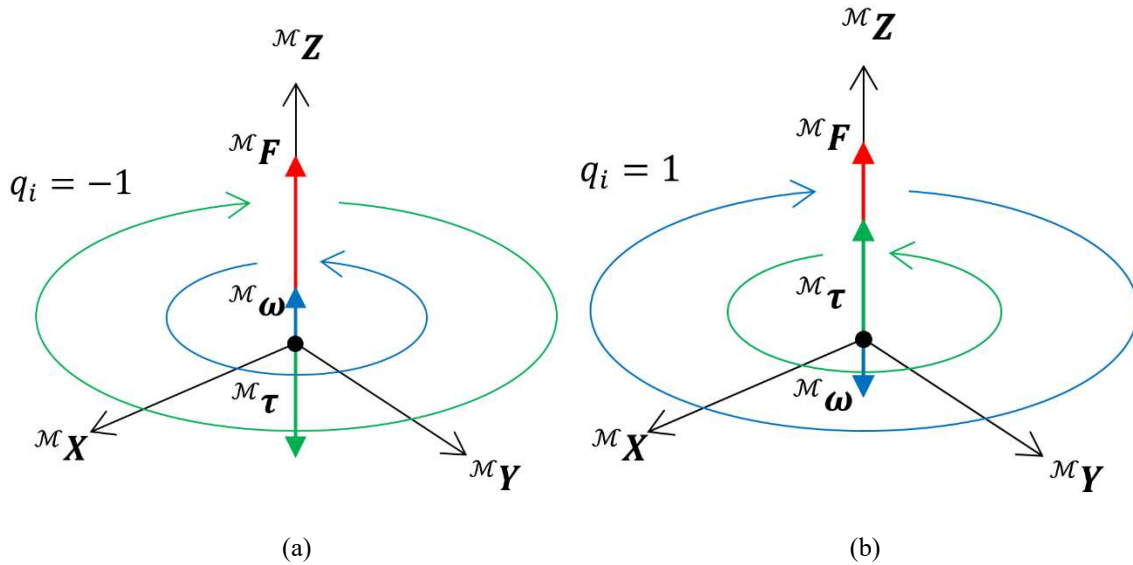


Figure 2.1. Rotor frame force and torque model (a) where rotor spin is CW. (b) where rotor spin is CCW.

Since multirotor airframes do not utilize passive airfoils, UAV models can be generated simply using Newton-Euler principles and the previously introduced motor model without the need for complex numeric aerodynamic simulations. However, the placement and orientation of the platform rotors greatly affects the platform's controllability and performance. Thus, to appropriately evaluate each multirotor model, both parallel and nonparallel models were defined explicitly here via a comprehensive classification system.

2.2 Non-Parallel and Parallel Models

The general model developed in this section describes any vertical take-off-and-landing (VTOL) aerial vehicle (AV), which utilize pure rotor propulsion to produce body-fixed forces and torques. That is, a multirotor model which utilizes external airfoils beyond propeller rotor pairings such as fixed wing aircraft or all anomalous AV of unorthodox configuration such as those in [41] or [42] are explicitly excluded from this analysis. A multirotor in this analysis was defined as any vehicle constructed by n rotor units as described in Figure 2.2, where a rotor unit is a single rotor placed statically at the origin of some frame \mathcal{M} about a UAV body-fixed-frame \mathcal{B} . As previously described in Figure 2.1, a motor will produce some thrust and drag about the z -axis of the frame \mathcal{M} for a given rotor spin ω_i . A net force and torque is then produced about \mathcal{B} , By adding more rotor units at appropriate transformations; stable flight is possible.

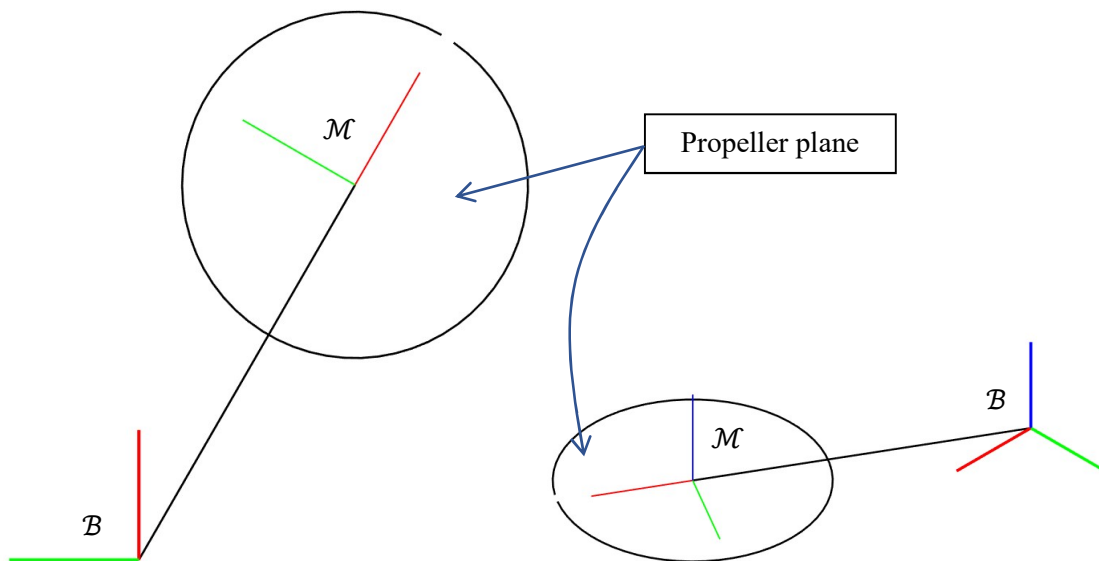


Figure 2.2. The general multirotor unit. This unit consists of some main body-fixed frame \mathcal{B} and some rotor frame \mathcal{M} which are transformed by some predefined static distance and rotation.

In this work, various types of multirotor are compared, where their classifications are distinguished by rotor unit transformations from the UAV body-fixed frame \mathcal{B} to motor frame \mathcal{M} . A classification or family of multirotor models are described by the symbol $\mathcal{F}_{(\cdot)}$ for a multirotor possessing a motor frame descriptor (\cdot) . The largest set of multirotor classes was defined in this analysis by the motor frame descriptor \mathcal{M} for simplicity. Thus, the general multirotor class was denoted $\mathcal{F}_{\mathcal{M}}$, where the transformation of the rotor frame from \mathcal{B} to \mathcal{M} is completely arbitrary, and \mathcal{M} may refer to any rotor frame for $\mathcal{M} = \{1\}, \{2\}, \dots, \{i\}, \dots, \{n\}$ given n rotors assigned to an airframe. In this work, new motor frame designations were adopted for each new classification introduced, and each classification discussed is assumed to be a subset of $\mathcal{F}_{\mathcal{M}}$.

The first model discussed in this analysis is that of parallel multirotor. The class designation $\mathcal{F}_{\mathcal{J}}$ is introduced to differentiate this multirotor type. To fully define the parallel rotor frame \mathcal{J} for $\mathcal{J} = \{1\}, \{2\}, \dots, \{i\}, \dots, \{n\}$, a single set of Euler rotation parameters

$$\boldsymbol{\gamma} = [\gamma_1 \ \gamma_2 \ \dots \ \gamma_i \ \dots \ \gamma_n]^T, \quad (2.2)$$

is introduced. The defining feature of a parallel multirotor is that each rotor unit possess parallel thrust and drag axes for all rotor frames \mathcal{J} , ${}^{\mathcal{B}}\mathbf{Z} \parallel {}^1\mathbf{Z} \parallel {}^2\mathbf{Z} \parallel \dots \parallel {}^i\mathbf{Z} \parallel \dots \parallel {}^n\mathbf{Z}$ for ${}^{\mathcal{B}}\mathbf{Z}$ representing a unit vector aligned with the z axis of \mathcal{B} . For n rotor units, n rotations defined by

$${}^{\mathcal{B}}R_{\mathcal{J}} = R_z(\gamma_i), \quad (2.3)$$

about \mathcal{B} may define all parallel rotor orientations of rotor frame \mathcal{J} arbitrarily. At this point in the analysis, the concept of cross-span L is introduced to fully define translational reference, and classify multirotor size or form factor. The cross-span represents the longest rotor origin to rotor origin distance measurable on a UAV. As a traditional multirotor design was the focus of this study, an assumption on equidistant and planar translation was imposed on all frame translations. The position of \mathcal{J} measured from \mathcal{B} , denoted ${}^{\mathcal{B}}\mathbf{P}_{\mathcal{J}}$, can be constructed then by the vector $\mathbf{v}_a = [L/2 \ 0 \ 0]^T$ in

$${}^B\mathbf{P}_J = {}^B R_J \mathbf{v}_a. \quad (2.4)$$

Platforms such as quadcopters, hexrotors, and octocopters can be considered parallel models as described in [2] and [11].

Using Equations (2.3) and (2.4), a frame network for the most basic four-unit parallel multirotor model can be generated as shown in Figure 2.3. Each rotor is translated by ${}^B\mathbf{P}_J$ and rotated by ${}^B R_J$ for $\gamma_i = (1 - 2i)\frac{\pi}{n}$ given n desired rotor units. In this formulation, adjacent rotations are equiangular.

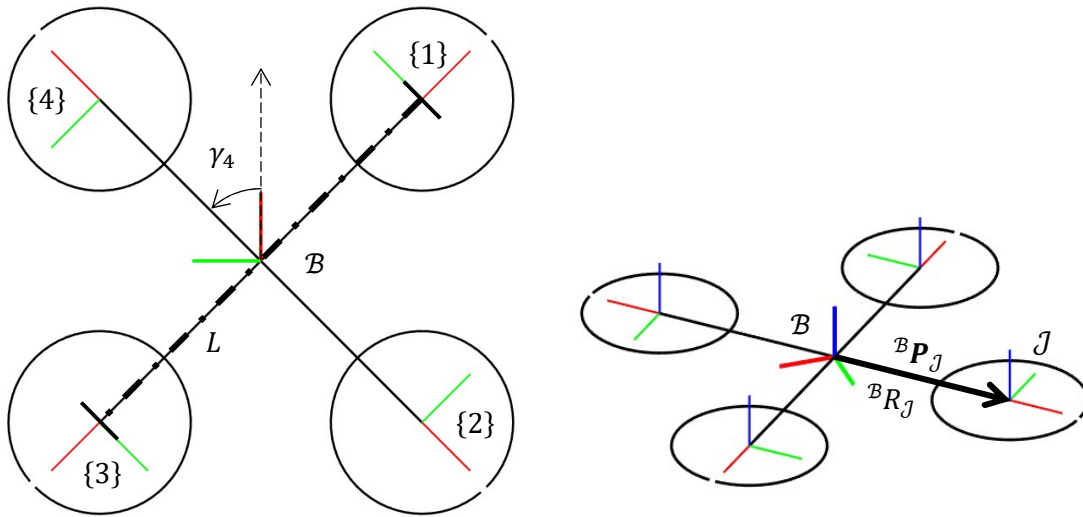


Figure 2.3. The quadrotor or X4-Flyer is a four-rotor unit parallel multirotor. Its frame network is shown for equiangular rotation parameters γ .

By increasing n , the number of rotor units, to six, a basic parallel hexrotor can be made. Figure 2.4 provides visualization of a generic parallel hexrotor model. The parallel hexrotor rotor units are rotated about \mathcal{B} by $\gamma_i = (1 - 2i)\frac{\pi}{n}$ using Equations (2.3) and (2.4) as they were for the X4-flyer in Figure 2.4.

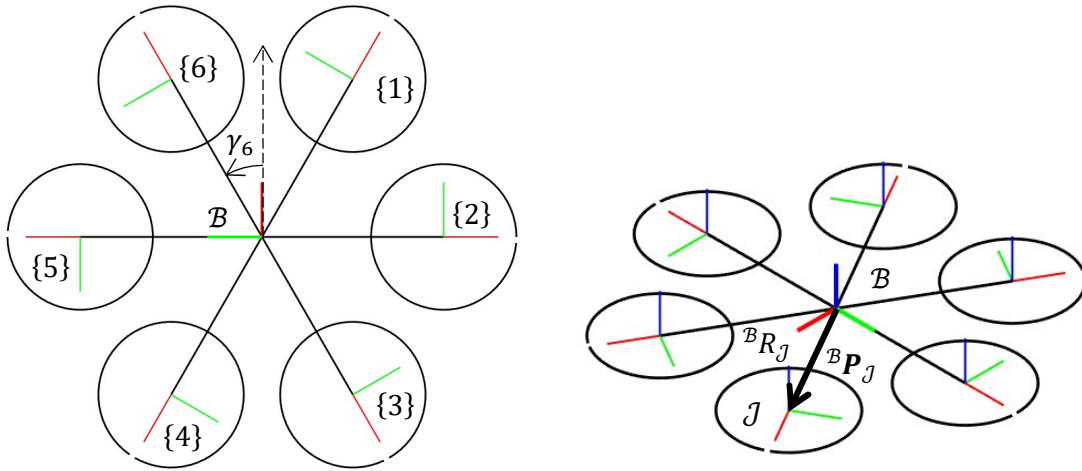


Figure 2.4. The hexrotor is a six-rotor unit parallel multirotor. Its frame network is shown for equiangular rotation parameters γ .

Another common parallel multirotor type is the octocopter. By utilizing $n = 8$ rotor units rotated by ${}^B R_J$ and translated by ${}^B \mathbf{P}_J$ for $\gamma_i = (1 - 2i)\frac{\pi}{n}$, a parallel model can be created as is shown in Figure 2.5.

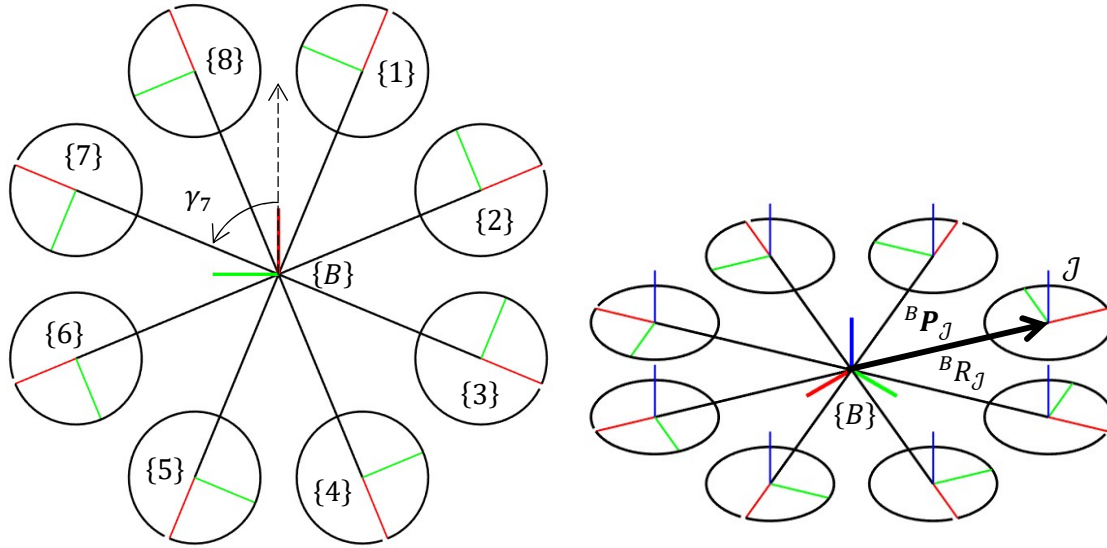


Figure 2.5. The octorotor is an eight-rotor unit parallel multirotor. Its frame network is shown for rotation parameters γ .

A nonparallel multirotor is classified as any platform possessing more than one rotor and propeller pairing, and possesses at least one motor axis which is skewed from at least one other motor axis in its design. Examples of nonparallel multirotor can be found in [37] and [31].

The objective of the model developed in this section is to promote a general framework for fully-actuated nonparallel multirotor design. A key assumption made was that all framework developed must be directly comparable to parallel multirotor designs. Nonparallel multirotor such as [35] were created in a completely novel way. The concept of form factor is not applicable to a design such as this, since the shape of the UAV is entirely different from traditional parallel multirotor. Hence, the emphasis on inclusion of a cross-span definition in the general model discussed thus far for parallel multirotor of class \mathcal{F}_J . This particular definition of form-factor is used commercially, where multirotor are classified by their cross-span [43], thus that convention was used here. Platforms such as the Matrice 600 Pro, Spreading Wings S900, and S1000+ possess cross-spans of 600 mm, 900 mm, and 1000 mm, respectively. Their available payload, and torque production profiles are of widely different classes simply due to their sheer size differences. Thus, a

desirable comparison for this analysis was determined to be between two multirotor of similar cross-span, and identical propeller rotor pairings. In other words, the models compared in this analysis were of the same size, and used the same rotors which possess thrust and drag coefficients b and d . Such a comparison provides a more informative assessment of model performance between parallel models and nonparallel models than that of arbitrary definition. To ensure this type of comparison, the general multirotor model considered in this work possesses rotor units translated by ${}^B\mathbf{P}_{\mathcal{M}} = {}^B\mathbf{P}_J$ for all classes of multirotor $\mathcal{F}_{\mathcal{M}}$.

Since each transformation is considered static, quaternion definitions were ignored in analysis, rather all possible Euler rotations are considered. As discussed, translation of rotors in class $\mathcal{F}_{\mathcal{M}}$ are considered universal for all models compared in this analysis. The rotor orientation of frame \mathcal{M} , however, can be defined in one of several ways using Euler rotations. The first class of nonparallel multirotor described in this analysis utilize two Euler rotations only in the definition of rotor orientation. The class was denoted $\mathcal{F}_{\mathcal{K}_k}$ for rotor frame designations \mathcal{K}_1 and \mathcal{K}_2 . Consider the rotation parameter set

$$\boldsymbol{\alpha} = [\alpha_1 \quad \alpha_2 \quad \dots \quad \alpha_i \quad \dots \quad \alpha_n]^T, \quad (2.5)$$

about a second axis in addition to the body-fixed z-axis rotation parameter $\boldsymbol{\gamma}$ in (2.3). The nonparallel rotor frame designations \mathcal{K}_1 and \mathcal{K}_2 for $\mathcal{K}_k = \{1\}, \{2\}, \dots, \{i\}, \dots, \{n\}$ are defined by the rotations

$${}^B R_{\mathcal{K}_1} = R_z(\gamma_i) R_x(\alpha_i), \quad (2.6)$$

$${}^B R_{\mathcal{K}_2} = R_z(\gamma_i) R_y(\alpha_i). \quad (2.7)$$

These are both nonparallel multirotor classifications of the type described in [38] and [37], respectively. These are the only two-axis Euler rotations possible developed from and considering the parallel model. That is, multirotor class $\mathcal{F}_{\mathcal{K}_k}$ is a subset of $\mathcal{F}_{\mathcal{M}}$ defining nonparallel multirotor with ZX and ZY Euler rotations applied to their motor frames in their orientation models, respectively using the parameters $\boldsymbol{\gamma}$ and $\boldsymbol{\alpha}$. Both authors imply full actuation in their works for hexrotor models augmented by these transformations,

however, these orientation models do not span the set of all possible rotor orientations. For this reason, they are not considered possible general models for nonparallel multirotor. Consider then a third rotation parameter set

$$\boldsymbol{\beta} = [\beta_1 \quad \beta_2 \quad \dots \quad \beta_i \quad \dots \quad \beta_n]^T. \quad (2.8)$$

The third class of nonparallel multirotor introduced in this analysis was denoted \mathcal{F}_{Q_q} for $Q_q = \{Q_1, Q_2, Q_3, Q_4\}$. This class is distinguished by three serial non-repeated axis Euler rotations of varying combinations. That is, each rotor frame is rotated by three serial non-repeated Euler axes of the form ZXY, ZXZ, ZYX, and ZYZ, respectively. One possible general model, which is of the type ZXY was discussed in [36]. In this model the rotation of the motor frame was given to be of the form

$${}^B R_{Q_1} = R_z(\gamma_i) R_x(\alpha_i) R_y(\beta_i). \quad (2.9)$$

While not introduced in any literature to date, the frame definitions Q_2 , Q_3 , and Q_4 defined by rotor rotations

$$\begin{aligned} {}^B R_{Q_2} &= R_z(\gamma_i) R_y(\alpha_i) R_x(\beta_i), \\ {}^B R_{Q_3} &= R_z(\gamma_i) R_y(\alpha_i) R_z(\beta_i), \end{aligned} \quad (2.10)$$

$${}^B R_{Q_4} = R_z(\gamma_i) R_x(\alpha_i) R_z(\beta_i),$$

make up the remaining descriptions of the class \mathcal{F}_{Q_q} . This class defines all nonparallel multirotor with nonconsecutive Euler axis rotations which first consider the parallel model Z rotation by $\boldsymbol{\gamma}$. The final class considered in this analysis are those multirotor with orientation models defined by shared axis rotations. This final class was denoted \mathcal{F}_{S_s} for $S_s = \{S_1, S_2\}$, where the orientation models were defined by

$${}^B R_{S_1} = R_z(\gamma_i + \alpha_i)R_y(\beta_i), \quad (2.11)$$

$${}^B R_{S_2} = R_z(\gamma_i + \alpha_i)R_x(\beta_i). \quad (2.12)$$

These rotation models contain two consecutive z-axis Euler rotations, and span the set of all possible orientations of nonparallel multirotor. As will be shown in this analysis, these two model definitions possess very useful properties concerning rotor performance between parallel and nonparallel multirotor classes.

Table 2.1 provides a compiled description of the models discussed in this section.

Table 2.1. All Euler frame definitions discussed in this analysis as subsets of the multirotor class m .

Class	Rotor Unit Position	Rotor Frame Orientation	Description
\mathcal{F}_J	${}^B \mathbf{P}_J = R_z(\gamma_i)\mathbf{v}_a$	${}^B R_J = R_z(\gamma_i)$	1 Axis Rotation: Euler Z
$\mathcal{F}_{\mathcal{K}_k}$	${}^B \mathbf{P}_{\mathcal{K}_1} = R_z(\gamma_i)\mathbf{v}_a$	${}^B R_{\mathcal{K}_1} = R_z(\gamma_i)R_x(\alpha_i)$	2 Axis Rotations: Euler ZX and ZY
	${}^B \mathbf{P}_{\mathcal{K}_2} = R_z(\gamma_i)\mathbf{v}_a$	${}^B R_{\mathcal{K}_2} = R_z(\gamma_i)R_y(\alpha_i)$	
\mathcal{F}_{Q_q}	${}^B \mathbf{P}_{Q_1} = R_z(\gamma_i)\mathbf{v}_a$	${}^B R_{Q_1} = R_z(\gamma_i)R_x(\alpha_i)R_y(\beta_i)$	3 Non-Consecutive Axis Rotations: Euler ZXY, ZXZ, ZYX, and ZYZ
	${}^B \mathbf{P}_{Q_2} = R_z(\gamma_i)\mathbf{v}_a$	${}^B R_{Q_2} = R_z(\gamma_i)R_x(\alpha_i)R_z(\beta_i)$	
	${}^B \mathbf{P}_{Q_3} = R_z(\gamma_i)\mathbf{v}_a$	${}^B R_{Q_3} = R_z(\gamma_i)R_y(\alpha_i)R_x(\beta_i)$	
	${}^B \mathbf{P}_{Q_4} = R_z(\gamma_i)\mathbf{v}_a$	${}^B R_{Q_4} = R_z(\gamma_i)R_y(\alpha_i)R_z(\beta_i)$	
\mathcal{F}_{S_s}	${}^B \mathbf{P}_{S_1} = R_z(\gamma_i)\mathbf{v}_a$	${}^B R_{S_1} = R_z(\gamma_i + \alpha_i)R_y(\beta_i)$	3 Axis Rotations: Euler ZZY and ZZX
	${}^B \mathbf{P}_{S_2} = R_z(\gamma_i)\mathbf{v}_a$	${}^B R_{S_2} = R_z(\gamma_i + \alpha_i)R_x(\beta_i)$	

Unit vectors

$$\begin{aligned}
{}^B\mathbf{X}_{\mathcal{M}} &= {}^B R_{\mathcal{M}} {}^B\mathbf{X}, \\
{}^B\mathbf{Y}_{\mathcal{M}} &= {}^B R_{\mathcal{M}} {}^B\mathbf{Y}, \\
{}^B\mathbf{Z}_{\mathcal{M}} &= {}^B R_{\mathcal{M}} {}^B\mathbf{Z},
\end{aligned} \tag{2.13}$$

which lie on the x-, y-, and z-axes of \mathcal{M} , can be defined using any of the discussed rotation models in Table 2.1. For this work, all classes of the form $\mathcal{F}_{\mathcal{Q}_q}$ and $\mathcal{F}_{\mathcal{S}_s}$ could be used for definition of a general non-parallel multirotor, however, those belonging to $\mathcal{F}_{\mathcal{S}_s}$ will be chosen, specifically the model defined by $\mathcal{F}_{\mathcal{S}_1}$. The general formulation of a nonparallel hexrotor of class $\mathcal{F}_{\mathcal{S}_1}$ was developed accordingly as in Figure 2.6.

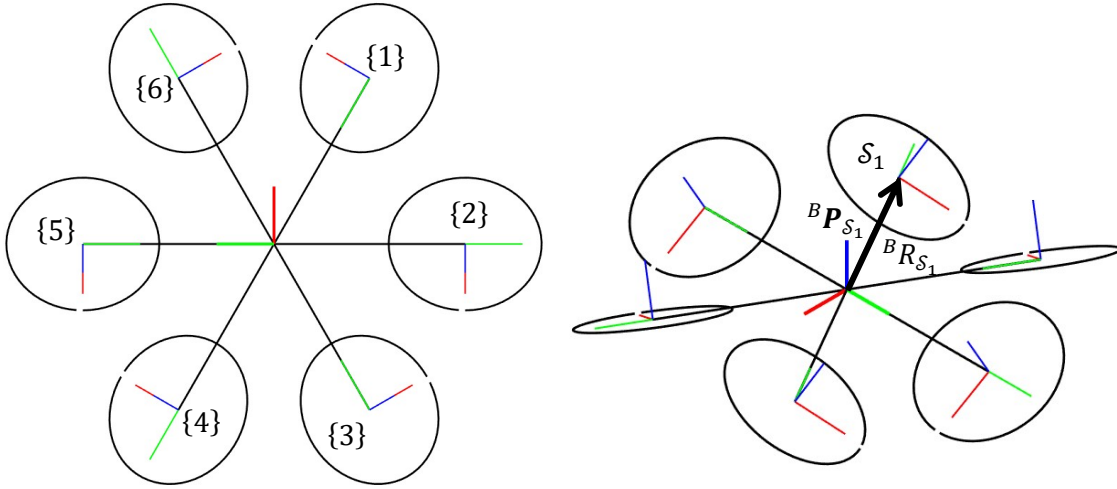


Figure 2.6. General formulation of a nonparallel hexrotor of class $\mathcal{F}_{\mathcal{S}_1}$. Its frame network is shown for rotation parameters γ, α, β .

The development of planar and vertical force concerning the body-fixed axis \mathcal{B} was considered extremely important in the development of the nonparallel multirotor model. Thus, two useful metrics which can be developed from the rotation modes is the unit projection of each motor thrust and drag axis ${}^B\mathbf{Z}_{\mathcal{M}}$ on ${}^B\mathbf{Z}$

$$z_{\mathcal{M}} = \|\mathcal{B}\mathbf{Z}_{\mathcal{M}} \cdot \mathcal{B}\mathbf{Z}\|_2 \equiv \begin{cases} z_{\mathcal{M}}(\beta_i) & \mathcal{M} := \mathcal{S}_s \\ z_{\mathcal{M}}(\alpha_i, \beta_i) & \mathcal{M} := \mathcal{Q}_q' \end{cases} \quad (2.14)$$

and the unit projection of each motor thrust and drag axis $\mathcal{B}\mathbf{Z}_{\mathcal{M}}$ on $\mathcal{B}\mathbf{X}\mathcal{B}\mathbf{Y}$

$$n_{\mathcal{M}} = \left\| \begin{cases} \mathcal{B}\mathbf{Z}_{\mathcal{M}} \cdot \mathcal{B}\mathbf{X} \\ \mathcal{B}\mathbf{Z}_{\mathcal{M}} \cdot \mathcal{B}\mathbf{Y} \end{cases} \right\|_2 \equiv \begin{cases} n_{\mathcal{M}}(\beta_i) & \mathcal{M} := \mathcal{S}_s \\ n_{\mathcal{M}}(\alpha_i, \beta_i) & \mathcal{M} := \mathcal{Q}_q' \end{cases} \quad (2.15)$$

provide explicit dependencies on α_i and β_i , while spanning the same set of solutions. This subtle difference will be taken full advantage of in the following derivations. In the next section the general kinematics and dynamics for a nonparallel multirotor was developed. Refer to Appendix A for a description of the derivation of general rigid body dynamics using the Newton-Euler formulism.

2.3 Kinematics

The instantaneous inertial position and orientation of a body fixed frame \mathcal{B} with respect to an inertial frame \mathcal{E} are given by

$$\begin{aligned} \mathcal{E}\mathbf{P}_{\mathcal{B}} &= [x \quad y \quad z]^T, \\ \mathcal{E}\mathbf{\Theta}_{\mathcal{B}} &= [\phi \quad \theta \quad \psi]^T. \end{aligned} \quad (2.16)$$

For an end-user, these states are more useful than a body-fixed frame definition, since knowing a UAV's exact position relative to the ground is desirable. The body-fixed frame linear and angular velocities are given then by

$$\begin{aligned} \mathcal{B}\mathbf{V} &= [u \quad v \quad w]^T, \\ \mathcal{B}\boldsymbol{\omega} &= [p \quad q \quad r]^T. \end{aligned} \quad (2.17)$$

The velocity states are more readily and accurately estimated using onboard IMU and gyroscope data. Thus, body-fixed frame definitions are more convenient to utilize in application. Appendix A contains useful kinematic definitions regarding frame transformations R_{Θ} and T_{Θ} . For more details please review the appropriate entries. The earth frame velocities can then be described by

$$\begin{aligned}\varepsilon \mathbf{V}_B &= R_{\Theta} {}^B \mathbf{V}, \\ \varepsilon \boldsymbol{\omega}_B &= T_{\Theta} {}^B \boldsymbol{\omega},\end{aligned}\tag{2.18}$$

The kinematic equations in this work are described using a hybrid frame \mathcal{H} state vector in \mathbb{R}^6 composed of an inertial frame linear states and body-fixed frame angular states. The state

$$\mathcal{H} \boldsymbol{\xi} = [\varepsilon \mathbf{V}_B^T \quad {}^B \boldsymbol{\omega}^T]^T,\tag{2.19}$$

represents this hybrid frame.

2.4 Dynamics

The dynamics of a UAV are discussed strictly using the Newton-Euler formulism as in Appendix A. A single rigid body is considered for the UAV model with mass m^* and mass moment of inertia

$${}^B J^* = \begin{bmatrix} J_{11}^* & J_{12}^* & J_{13}^* \\ J_{21}^* & J_{22}^* & J_{23}^* \\ J_{31}^* & J_{32}^* & J_{33}^* \end{bmatrix}.\tag{2.20}$$

Refer to Appendix A for more details on the Newton-Euler formulism. In this section the external effects and rotor force and torque production for nonparallel multirotor of type \mathcal{S}_1 is discussed. Finally, the dynamic equations of motion are derived.

2.4.1 External Effects

There are three external effects considered in this analysis. Gravitational effects can be modeled using

$$\mathbf{F}_g = [0 \quad 0 \quad -m^*g]^T, \quad (2.21)$$

which corresponds to the force of gravity applied to the body-fixed frame measured in the inertial frame \mathcal{E} .

The UAV center of gravity (COG), defined by the frame \mathcal{C} , ${}^{\mathcal{B}}\mathbf{P}_c = [{}^{\mathcal{B}}p_{x_c} \quad {}^{\mathcal{B}}p_{y_c} \quad {}^{\mathcal{B}}p_{z_c}]^T$ is the center of gravity of the UAV with respect to the frame \mathcal{B} . For ${}^{\mathcal{B}}\mathbf{P}_c \neq \mathbf{0}$, a body fixed torque is produced about \mathcal{B} due to gravity ${}^{\mathcal{B}}\mathbf{P}_c \times R_{\Theta}^T \mathbf{F}_g$. The vector $\mathbf{\Gamma}_g \in \mathbb{R}^6$ is defined to represent all gravitation effects for the nonlinear model

$$\mathbf{\Gamma}_g = [\mathbf{F}_g^T \quad ({}^{\mathcal{B}}\mathbf{P}_c \times R_{\Theta}^T \mathbf{F}_g)^T]^T. \quad (2.22)$$

The second external effect modeled is gyroscopic torque. In the previous sections, frame definitions for the various nonparallel multirotor were introduced. In this paper, the nonparallel multirotor class \mathcal{F}_{S_1} is developed. This is one of the two consecutive axis rotation models introduced, and provides a unique description of rotor force and torque production. Gyroscopic torque can be considered a byproduct of thrust and drag generation, and occurs due to procession of the propeller/rotor pairing for nonzero ${}^{\mathcal{B}}\boldsymbol{\omega}$. Introducing the rotor velocity vector ${}^{S_1}\boldsymbol{\Omega} = [0 \quad 0 \quad q_i\omega_i]^T$, the gyroscopic torque vector $\mathbf{\Gamma}_o$ can be defined by

$$\mathbf{\Gamma}_o = -J_r \sum_{S_1=\{1\}}^{\{n\}} \left\{ {}^{\mathcal{B}}\boldsymbol{\omega} \times {}^{\mathcal{B}}R_{S_1} {}^{S_1}\boldsymbol{\Omega} \right\}, \quad (2.23)$$

where J_r is a simplified scalar mass moment of inertia prescribed to a single rotor. While this torque is dependent on the user-input, it is not considered a direct control effort, rather a byproduct of control allocation.

The final external effect considered is general disturbance. All unmodelable effects such as wind, manipulator dynamics, etc. are categorized under this definition. Disturbance forces \mathbf{F}_w and torques $\boldsymbol{\tau}_w$ are used to construct the disturbance vector $\mathbf{\Gamma}_w$ defined in

$$\begin{aligned}
\mathbf{F}_w &= [W_1 \quad W_2 \quad W_3]^T, \\
\boldsymbol{\tau}_w &= [W_4 \quad W_5 \quad W_6]^T, \\
\boldsymbol{\Gamma}_w &= [\mathbf{F}_w^T \quad \boldsymbol{\tau}_w^T]^T.
\end{aligned} \tag{2.24}$$

2.4.2 Production of Rotor Force and Torque

The rotor propeller pairing produces some thrust and drag about the rotor axis. By combining multiple rotors, the net force and torque about the body-fixed frame \mathcal{B} can be constructed from the following definitions for force ${}^{\mathcal{B}}\mathbf{F}_{S_1}$ and torque ${}^{\mathcal{B}}\boldsymbol{\tau}_{S_1}$ in

$$\begin{aligned}
{}^{\mathcal{B}}\mathbf{F}_{S_1} &= {}^{\mathcal{B}}R_{S_1} {}^{S_1}\mathbf{F}, \\
{}^{\mathcal{B}}\boldsymbol{\tau}_{S_1} &= {}^{\mathcal{B}}R_{S_1} {}^{S_1}\boldsymbol{\tau} + ({}^{\mathcal{B}}\mathbf{P}_{S_1} \times ({}^{\mathcal{B}}R_{S_1} {}^{S_1}\mathbf{F})).
\end{aligned} \tag{2.25}$$

By factoring ω_i^2 , a basis composed of all design parameters can be formulated for both ${}^{\mathcal{B}}\mathbf{F}_{S_1}$ and ${}^{\mathcal{B}}\boldsymbol{\tau}_{S_1}$,

$$\begin{aligned}
{}^{\mathcal{B}}\mathbf{F}_{S_1} &= \begin{pmatrix} bs_{\beta_i} c_{\gamma_i + \alpha_i} \\ bs_{\beta_i} s_{\gamma_i + \alpha_i} \\ bc_{\beta_i} \end{pmatrix} \omega_i^2, \\
{}^{\mathcal{B}}\boldsymbol{\tau}_{S_1} &= \begin{pmatrix} q_i ds_{\beta_i} c_{\gamma_i + \alpha_i} + \frac{1}{2} Lbc_{\beta_i} s_{\gamma_i} \\ q_i ds_{\beta_i} s_{\gamma_i + \alpha_i} - \frac{1}{2} Lbc_{\beta_i} c_{\gamma_i} \\ q_i dc_{\beta_i} + \frac{1}{2} Lbs_{\beta_i} s_{\alpha_i} \end{pmatrix} \omega_i^2.
\end{aligned} \tag{2.26}$$

The body frame force ${}^{\mathcal{B}}\mathbf{F}_{S_1}$ is simply rotated by ${}^{\mathcal{B}}R_{S_1}$, while the body frame torque receives contributions from the pure drag vector and thrust vector at some lever arm ${}^{\mathcal{B}}\mathbf{P}_{S_1}$. Combining these expressions into an \mathbb{R}^6 vector definition for control allocation $\boldsymbol{\Gamma}_u$ results

$$\boldsymbol{\Gamma}_u = \sum_{i=1}^6 \boldsymbol{\Gamma}_u^i = \sum_{\mathcal{S}_1=\{1\}}^{\{n\}} \begin{bmatrix} {}^B \mathbf{F}_{\mathcal{S}_1}^T & {}^B \boldsymbol{\tau}_{\mathcal{S}_1}^T \end{bmatrix}^T. \quad (2.27)$$

2.4.3 Dynamic Formulation

With the external effects and control allocation defined, the general matrix form of the dynamics can be constructed using the mass matrix

$$M = \begin{bmatrix} m^* I_{3 \times 3} & \mathbf{0}_{3 \times 3} \\ \mathbf{0}_{3 \times 3} & {}^B J^* \end{bmatrix}, \quad (2.28)$$

and centripetal-Coriolis matrix

$$C({}^{\mathcal{H}} \dot{\boldsymbol{\xi}}) = \begin{bmatrix} \mathbf{0}_{3 \times 3} & \mathbf{0}_{3 \times 3} \\ \mathbf{0}_{3 \times 3} & -S({}^B J^* \boldsymbol{\omega}) \end{bmatrix}. \quad (2.29)$$

The dynamic formulation in \mathbb{R}^6 is then

$$M {}^{\mathcal{H}} \ddot{\boldsymbol{\xi}} + C({}^{\mathcal{H}} \dot{\boldsymbol{\xi}}) {}^{\mathcal{H}} \dot{\boldsymbol{\xi}} = \boldsymbol{\Gamma}_T, \quad (2.30)$$

$$\boldsymbol{\Gamma}_T := \boldsymbol{\Gamma}_g + \boldsymbol{\Gamma}_o + \boldsymbol{\Gamma}_u + \boldsymbol{\Gamma}_w.$$

The full dynamic formulation can be written in terms of the derivative of state ${}^{\mathcal{H}} \dot{\boldsymbol{\xi}}$ as

$${}^{\mathcal{H}} \dot{\boldsymbol{\xi}} = M^{-1} (-C({}^{\mathcal{H}} \dot{\boldsymbol{\xi}}) {}^{\mathcal{H}} \dot{\boldsymbol{\xi}} + \boldsymbol{\Gamma}_T). \quad (2.31)$$

To make analysis and control developments more convenient, the linear inertial frame states can be resolved separately from the angular body-fixed frame states

$$\varepsilon \dot{\mathbf{V}}_B = m^{*-1} \left(\mathbf{F}_g + R_{\Theta} \sum_{\mathcal{S}_1=\{1\}}^{\{n\}} ({}^B \mathbf{F}_{\mathcal{S}_1}) + \mathbf{F}_w \right), \quad (2.32)$$

$${}^B\dot{\boldsymbol{\omega}} = {}^B J^{*-1} \left(S({}^B J^* {}^B \boldsymbol{\omega}) {}^B \boldsymbol{\omega} + {}^B \mathbf{P}_c \times R_{\Theta}^T \mathbf{F}_g + \sum_{\mathcal{S}_1=\{1\}}^{\{n\}} \left({}^B \boldsymbol{\tau}_{\mathcal{S}_1} - J_r({}^B \boldsymbol{\omega} \times {}^B R_{\mathcal{S}_1} \boldsymbol{\Omega}) \right) + \boldsymbol{\tau}_w \right).$$

3 Physical System Design

This section provides a justification for the design of a special class of fully-actuated nonparallel hexrotor \mathcal{F}_{S_1} used in experimentation for this work. It was shown analytically that there are a finite number of possible orientation sets which satisfy all criteria defined for a nonparallel hexrotor of type \mathcal{F}_{S_1} , which utilize existing control architecture in all existing hexrotor flight stacks concerning throttle, roll, pitch, and yaw. The full design was then implemented on an experimental platform described in the following sections.

3.1 Defining the UAV Motor Map

The UAV motor map is developed analytically in this section. For convenience, the vectors

$$\begin{aligned}
 \boldsymbol{\omega} &= [\omega_1 \quad \omega_2 \quad \omega_3 \quad \omega_4 \quad \omega_5 \quad \omega_6]^T, \\
 \boldsymbol{\alpha} &= [\alpha_1 \quad \alpha_2 \quad \alpha_3 \quad \alpha_4 \quad \alpha_5 \quad \alpha_6]^T, \\
 \boldsymbol{\beta} &= [\beta_1 \quad \beta_2 \quad \beta_3 \quad \beta_4 \quad \beta_5 \quad \beta_6]^T, \\
 \boldsymbol{q} &= [q_1 \quad q_2 \quad q_3 \quad q_4 \quad q_5 \quad q_6]^T,
 \end{aligned} \tag{3.1}$$

are defined for use in the analysis. These vectors correspond to the rotor effort and three static design parameters, which determine wrench production for the platform. $\boldsymbol{\omega}$ specifically determines wrench production at application time of UAV flight, whereas $\boldsymbol{\alpha}$, $\boldsymbol{\beta}$, and \boldsymbol{q} remain static, and are determined at the design phase of implementation. It is the shaping of these static parameters that determine the UAV's flight characteristics. Factoring $\boldsymbol{\omega}$ from $\boldsymbol{\Gamma}_u$ developed in Eq. (2.27) results the mapping

$$\boldsymbol{\Gamma}_u = A(\boldsymbol{\alpha}, \boldsymbol{\beta}, \boldsymbol{q})\boldsymbol{\omega}. \tag{3.2}$$

User rotor control, defined uniquely by $\boldsymbol{\omega}$, then becomes the representation of the force torque control vector in the static basis $A(\boldsymbol{\alpha}, \boldsymbol{\beta}, \boldsymbol{q})$. While there are limitations on the form of $A(\boldsymbol{\alpha}, \boldsymbol{\beta}, \boldsymbol{q})$, the overarching objective of this work is the design of a fully-actuated and dimensionally decoupled controller. More abstractly, the axes of control must be orthogonal and decoupled by design. The restrictions on how the user manipulates $\boldsymbol{\omega}$ must above all comply with this design criteria, thus, $\boldsymbol{\omega}$ is decomposed according to a desired user effort u'_i and introduced allocation bases E_i^T . For $i = 1, 2, \dots, 6$, u'_i represents a desired forward, lateral, throttle, roll, pitch, and yaw force or torque, respectively. By allocating rotor speed in the direction of the unit vector bases E_i^T , decoupled force/torque production results. Six decoupled rotor effort vectors $\boldsymbol{\omega}_i$ are then introduced to represent this decoupled force/torque production in the rotor speed space $\boldsymbol{\omega}$, and their summation results $\boldsymbol{\omega}$. The rotor speed vector can then be expressed as

$$\boldsymbol{\omega} = \sum_{i=1}^6 \boldsymbol{\omega}_i = \sum_{i=1}^6 E_i^T u'_i = E^T \boldsymbol{u}', \quad (3.3)$$

where the basis E^T allocates effort into the 6 rotors according to orthogonal desired control inputs. The basis components may be defined by

$$\begin{aligned} E_1^T &= [x_1 \quad x_2 \quad x_3 \quad x_4 \quad x_5 \quad x_6]^T, \\ E_2^T &= [y_1 \quad y_2 \quad y_3 \quad y_4 \quad y_5 \quad y_6]^T, \\ E_3^T &= \frac{1}{\sqrt{6}} [1 \quad 1 \quad 1 \quad 1 \quad 1 \quad 1]^T, \\ E_4^T &= \frac{1}{\sqrt{3}} \left[-\frac{1}{2} \quad -1 \quad -\frac{1}{2} \quad \frac{1}{2} \quad 1 \quad \frac{1}{2} \right]^T, \\ E_5^T &= \left[-\frac{1}{2} \quad 0 \quad \frac{1}{2} \quad \frac{1}{2} \quad 0 \quad -\frac{1}{2} \right]^T, \\ E_6^T &= \frac{1}{\sqrt{6}} [1 \quad -1 \quad 1 \quad -1 \quad 1 \quad -1]^T, \end{aligned} \quad (3.4)$$

where $x_i = x_1, x_2, \dots, x_6$ and $y_i = y_1, y_2, \dots, y_6$ correspond to design bases allocating rotor effort into the forward and lateral force directions. The form of E_i^T for $i = 3, 4, 5, 6$ correspond to the production of throttle, roll, pitch, and yaw, respectively, and the form introduced can be determined by inspection of the rotor model of parallel hexrotors. APM and other compliant flight stacks control multirotor throttle, roll, pitch, and yaw identically due to rotor placements. While works such as [7] develop variable inverse mappings, there is a unique physical mapping corresponding to the location of the rotors. Quadrotors possess a unique inverse rotor speed mapping because there are four rotors and four degrees of control in the under-actuated control system. In the fully-actuated hexrotor design there is a unique, full-rank motor mapping for 6DOF control, thus there exists a unique inverse motor mapping as described. Throttle control increases a UAV's force production along its body fixed z-axis ${}^B\mathbf{Z}$, thus every rotor is forced to increase or decrease its output by equal amounts for any requested change to desired throttle u'_3 . The basis E_4^T allocates user desired roll effort u'_4 over the UAV rotors by creating a differential between the left-hand (rotors 4, 5, and 6) and right-hand (rotors 1, 2, and 3) side rotors. The differential causes a decoupled torque about the body-fixed x-axis ${}^B\mathbf{X}$. The basis E_5^T allocates user desired pitch effort u'_5 over the UAV rotors by creating a differential between the forward (rotors 1 and 6) and rear (rotors 3 and 4) rotors. This causes a net torque about the UAV body-fixed y-axis ${}^B\mathbf{Y}$. Lastly, the basis E_6^T allocates desired yaw effort u'_6 over the UAV rotors by creating a differential between the platforms CW and CCW spinning rotors. Since yaw torque in parallel multirotor configurations is determined exclusively by drag torque, the physical position has no effect on yaw production, however, to maintain orthogonality in all other dimensions, alternative assignment of CW and CCW spin is necessary. The four bases allocating effort for throttle, roll, pitch, and yaw across the UAV rotors was interpreted physically by Figure 3.1. Red and green vectors indicated correspond to a differential, whereas blue vectors indicate a produced net force, and orange vectors indicate a produced net torque.

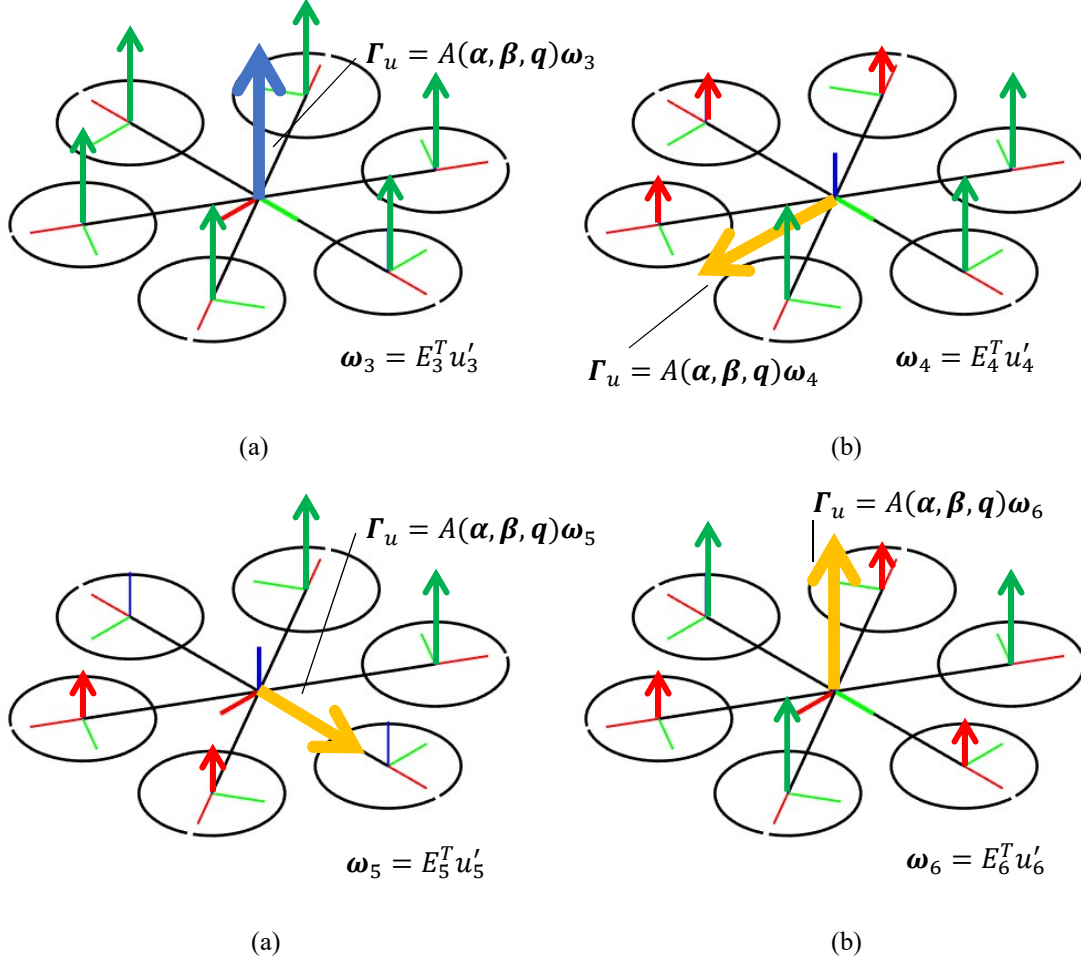


Figure 3.1. Physical correspondence for (a) UAV throttle control. (b) UAV roll control. (c) UAV pitch control. (d) UAV yaw control.

Substituting $\boldsymbol{\omega}$ as described by Eq. (3.3) into Eq. (3.2) provides an alternative representation of $\boldsymbol{\Gamma}_u$ in the basis $B(\boldsymbol{\alpha}, \boldsymbol{\beta}, \boldsymbol{q})$, which maps user desired control to the force torque space

$$\boldsymbol{\Gamma}_u = A(\boldsymbol{\alpha}, \boldsymbol{\beta}, \boldsymbol{q})E^T \mathbf{u}' = B(\boldsymbol{\alpha}, \boldsymbol{\beta}, \boldsymbol{q})\mathbf{u}'. \quad (3.5)$$

It is trivially true that if the designed platform is to be compliant with commercial flight stacks, and orthogonal with respect to the representation \mathbf{u}' and $\boldsymbol{\Gamma}_u$, the elements of \mathbf{u}' must produce decoupled forces and torques in $\boldsymbol{\Gamma}_u$. The form of the static basis $B(\boldsymbol{\alpha}, \boldsymbol{\beta}, \boldsymbol{q})$ is then necessarily diagonal, where

$$\mathbf{b}(\boldsymbol{\alpha}, \boldsymbol{\beta}, \mathbf{q}) = [b_1 \quad b_2 \quad b_3 \quad b_4 \quad b_5 \quad b_6]^T,$$

$$B(\boldsymbol{\alpha}, \boldsymbol{\beta}, \mathbf{q}) = \begin{bmatrix} b_1 & 0 & 0 & 0 & 0 & 0 \\ 0 & b_2 & 0 & 0 & 0 & 0 \\ 0 & 0 & b_3 & 0 & 0 & 0 \\ 0 & 0 & 0 & b_4 & 0 & 0 \\ 0 & 0 & 0 & 0 & b_5 & 0 \\ 0 & 0 & 0 & 0 & 0 & b_6 \end{bmatrix}. \quad (3.6)$$

The physical model basis $A(\boldsymbol{\alpha}, \boldsymbol{\beta}, \mathbf{q})$, while expressible in an infinite number of ways, must be decomposable into a diagonal matrix $B(\boldsymbol{\alpha}, \boldsymbol{\beta}, \mathbf{q})$ and an orthonormal matrix E as in

$$A(\boldsymbol{\alpha}, \boldsymbol{\beta}, \mathbf{q}) = B(\boldsymbol{\alpha}, \boldsymbol{\beta}, \mathbf{q})E, \quad (3.7)$$

if and only if, $A(\boldsymbol{\alpha}, \boldsymbol{\beta}, \mathbf{q})$ is full rank, and the UAV design is compliant to the decoupled axis assumptions. For convenience, the bases which have been predetermined by the (ArduPilot Mega) APM flight stack were expressed as a deficient rank matrix

$$E_a = [E_3^T \quad E_4^T \quad E_5^T \quad E_6^T]^T. \quad (3.8)$$

Since the forward and lateral force bases do not exist in commercial flight stacks, determination of their form relies on development of the given assumptions. Essentially, this portion of the analysis concerns finding the orthogonal compliment of the system E_a . Firstly, the forward and lateral bases E_1^T and E_2^T must remain orthogonal to all bases defined in E_a , thus

$$E_a = \begin{bmatrix} E_a & \mathbf{0}_{4 \times 6} \\ \mathbf{0}_{4 \times 6} & E_a \end{bmatrix} \begin{Bmatrix} E_1^T \\ E_2^T \end{Bmatrix} = \mathbf{0}_{8 \times 1}, \quad (3.9)$$

must hold for all design configurations of E_1^T and E_2^T . The forward and lateral bases must also remain orthogonal to each other. Their relationship can be described by

$$\forall i, j \in \{1,2\} | E_i \cdot E_j = \begin{cases} 1 & i = j \\ 0 & i \neq j \end{cases} \quad (3.10)$$

It should be noted that, the actual shape, design, and method of generating the control allocation bases E_i^T has not been discussed. Effectively, the presented discussion aims to develop the given assumptions for compatible forms of the basis $A(\boldsymbol{\alpha}, \boldsymbol{\beta}, \boldsymbol{q})$. Without further development, the 18 static design parameters $\boldsymbol{\alpha}$, $\boldsymbol{\beta}$, and \boldsymbol{q} must be developed using optimization methods such as those introduced in [36]. In this work, the form of the basis model is fully developed, starting with the reduction of the basis parameters E_1^T and E_2^T . Using Eq. (3.9) a new representation of E_1^T and E_2^T is introduced, where the free parameters ζ_r span the solution

$$\begin{aligned} \mathbf{n}_1 &:= \frac{1}{\sqrt{3}} \begin{bmatrix} \frac{1}{2} & -1 & \frac{1}{2} & \frac{1}{2} & -1 & \frac{1}{2} & \mathbf{0}_{1 \times 6} \end{bmatrix}^T, \\ \mathbf{n}_2 &:= \begin{bmatrix} \frac{1}{2} & 0 & -\frac{1}{2} & \frac{1}{2} & 0 & -\frac{1}{2} & \mathbf{0}_{1 \times 6} \end{bmatrix}^T, \\ \mathbf{n}_3 &:= \frac{1}{\sqrt{3}} \begin{bmatrix} \mathbf{0}_{1 \times 6} & \frac{1}{2} & -1 & \frac{1}{2} & \frac{1}{2} & -1 & \frac{1}{2} \end{bmatrix}^T, \\ \mathbf{n}_4 &:= \begin{bmatrix} \mathbf{0}_{1 \times 6} & \frac{1}{2} & 0 & -\frac{1}{2} & \frac{1}{2} & 0 & -\frac{1}{2} \end{bmatrix}^T, \\ \begin{Bmatrix} E_1^T(\mathbf{x}) \\ E_2^T(\mathbf{y}) \end{Bmatrix} &:= \begin{Bmatrix} E_1^T(\boldsymbol{\zeta}) \\ E_2^T(\boldsymbol{\zeta}) \end{Bmatrix} = \sum_{i=1}^4 \zeta_r \mathbf{n}_r, \end{aligned} \quad (3.11)$$

where all \mathbf{n}_r were determined to be null solutions to the system in Eq. (3.9) by inspection. This new representation reduces the number of free parameters in $x_i = x_1, x_2, \dots, x_6$ and $y_i = y_1, y_2, \dots, y_6$ from 12 to 4. The general solution of Eq. (3.9) is clearly that of the null solution, since $\text{rank} \left(\begin{bmatrix} E_a & \mathbf{0}_{4 \times 6} \\ \mathbf{0}_{4 \times 6} & E_a \end{bmatrix} \right) = 8$, the nullity of the system is 4, and the number of independent parameters required to represent this system is 4. Utilizing the developed general parameterization of E_1^T and E_2^T in Eq. (3.10) results

$$\zeta_1\zeta_3 + \zeta_2\zeta_4 = 0,$$

$$\zeta_1^2 + \zeta_2^2 = 1, \tag{3.12}$$

$$\zeta_3^2 + \zeta_4^2 = 1.$$

With the definitions of Eq. (3.6), Eq. (3.11), and Eq. (3.12) introduced, the form of $B(\boldsymbol{\alpha}, \boldsymbol{\beta}, \mathbf{q})$ and E have been expressed in satisfactory terms for decomposition of $A(\boldsymbol{\alpha}, \boldsymbol{\beta}, \mathbf{q})$. As the system's physical motor map between $\boldsymbol{\omega}$ and $\boldsymbol{\Gamma}_u$, $A(\boldsymbol{\alpha}, \boldsymbol{\beta}, \mathbf{q})$ can be expressed using column bases A_i defined in

$$\boldsymbol{\Gamma}_u = [A_1 \ A_2 \ A_3 \ A_4 \ A_5 \ A_6]\boldsymbol{\omega} = A(\boldsymbol{\alpha}, \boldsymbol{\beta}, \mathbf{q})\boldsymbol{\omega}, \tag{3.13}$$

where

$$\boldsymbol{\Gamma}_u = \sum_{i=1}^6 \left\{ \begin{array}{c} bs_{\beta_i}c_{\gamma_i+\alpha_i} \\ bs_{\beta_i}s_{\gamma_i+\alpha_i} \\ bc_{\beta_i} \\ q_i ds_{\beta_i}c_{\gamma_i+\alpha_i} + \frac{1}{2}Lbc_{\beta_i}s_{\gamma_i} \\ q_i ds_{\beta_i}s_{\gamma_i+\alpha_i} - \frac{1}{2}Lbc_{\beta_i}c_{\gamma_i} \\ q_i dc_{\beta_i} + \frac{1}{2}Lbs_{\beta_i}s_{\alpha_i} \end{array} \right\} \boldsymbol{\omega}_i^2 = \sum_{i=1}^6 A_i \boldsymbol{\omega}_i^2. \tag{3.14}$$

Each column basis A_i represents the i^{th} rotor's force and torque contribution to the body-fixed frame \mathcal{B} . One natural simplification for this system is then the substitution of γ_i in each basis A_i . γ_i is fully defined for all multirotor as equiangular by assumption, thus for a hexrotor,

$$\begin{aligned} \gamma_i &= (1 - 2i) \frac{\pi}{n} \Rightarrow \boldsymbol{\gamma} = [\gamma_1 \ \gamma_2 \ \gamma_3 \ \gamma_4 \ \gamma_5 \ \gamma_6]^T = \\ & \left[-\frac{\pi}{6} \quad -\frac{3\pi}{6} \quad -\frac{5\pi}{6} \quad -\frac{7\pi}{6} \quad -\frac{9\pi}{6} \quad -\frac{11\pi}{6} \right]^T. \end{aligned} \tag{3.15}$$

The basis A_i can be rewritten using trigonometric identities as

$$A_i = \left\{ \begin{array}{c} bs_{\beta_i}c_{\gamma_i+\alpha_i} \\ bs_{\beta_i}s_{\gamma_i+\alpha_i} \\ bc_{\beta_i} \\ q_id s_{\beta_i}c_{\gamma_i+\alpha_i} + \frac{1}{2}Lbc_{\beta_i}s_{\gamma_i} \\ q_id s_{\beta_i}s_{\gamma_i+\alpha_i} - \frac{1}{2}Lbc_{\beta_i}c_{\gamma_i} \\ q_idc_{\beta_i} + \frac{1}{2}Lbs_{\beta_i}s_{\alpha_i} \end{array} \right\} = \left\{ \begin{array}{c} bs_{\beta_i}(c_{\alpha_i}c_{\gamma_i} - s_{\alpha_i}s_{\gamma_i}) \\ bs_{\beta_i}(c_{\alpha_i}s_{\gamma_i} + s_{\alpha_i}c_{\gamma_i}) \\ bc_{\beta_i} \\ q_id s_{\beta_i}c_{\alpha_i}c_{\gamma_i} - \left(q_id s_{\beta_i}s_{\alpha_i} - \frac{1}{2}Lbc_{\beta_i}\right)s_{\gamma_i} \\ q_id s_{\beta_i}c_{\alpha_i}s_{\gamma_i} + \left(q_id s_{\beta_i}s_{\alpha_i} - \frac{1}{2}Lbc_{\beta_i}\right)c_{\gamma_i} \\ q_idc_{\beta_i} + \frac{1}{2}Lbs_{\beta_i}s_{\alpha_i} \end{array} \right\}. \quad (3.16)$$

To factor E from $A(\boldsymbol{\alpha}, \boldsymbol{\beta}, \boldsymbol{q})$, it is helpful to define the vector masks from tensor index notation

$$\begin{aligned} \hat{\boldsymbol{e}}_1 &= [1 \quad 0 \quad \dots \quad 0]^T, \\ \hat{\boldsymbol{e}}_2 &= [0 \quad 1 \quad \dots \quad 0]^T, \\ &\dots, \\ \hat{\boldsymbol{e}}_n &= [0 \quad 0 \quad \dots \quad 1]^T, \end{aligned} \quad (3.17)$$

for use in the definition of the scalar components c_{γ_i} , s_{γ_i} , and 1 in terms of the bases defined in the compliance matrix E_a

$$\begin{aligned} c_{\gamma_i} &:= \left[\frac{\sqrt{3}}{2} \quad 0 \quad -\frac{\sqrt{3}}{2} \quad -\frac{\sqrt{3}}{2} \quad 0 \quad \frac{\sqrt{3}}{2} \right]^T \hat{\boldsymbol{e}}_i = -\sqrt{3}E_5 \hat{\boldsymbol{e}}_i, \\ s_{\gamma_i} &:= \left[-\frac{1}{2} \quad -1 \quad -\frac{1}{2} \quad \frac{1}{2} \quad 1 \quad \frac{1}{2} \right]^T \hat{\boldsymbol{e}}_i = \sqrt{3}E_4 \hat{\boldsymbol{e}}_i, \\ 1 &:= \sqrt{6}E_3 \hat{\boldsymbol{e}}_i = \sqrt{6}(-1)^{i+1}E_6 \hat{\boldsymbol{e}}_i. \end{aligned} \quad (3.18)$$

These definitions allow for the expression of factorable row bases E_3 , E_4 , E_5 , and E_6 . Due to the diagonal form of $B(\boldsymbol{\alpha}, \boldsymbol{\beta}, \boldsymbol{q})$, each row basis must be factorable from A_i for all i , else Eq. (3.7) is invalidated, and the design is not compliant or full-rank. A_i can then be written in the form

$$A_i = \sqrt{3} \left\{ \begin{array}{l} bs_{\beta_i}(-c_{\alpha_i}E_5 - s_{\alpha_i}E_4) \\ bs_{\beta_i}(c_{\alpha_i}E_4 - s_{\alpha_i}E_5) \\ \sqrt{2}bc_{\beta_i}E_3 \\ -q_id s_{\beta_i}c_{\alpha_i}E_5 - \left(q_id s_{\beta_i}s_{\alpha_i} - \frac{1}{2}Lbc_{\beta_i}\right)E_4 \\ q_id s_{\beta_i}c_{\alpha_i}E_4 - \left(q_id s_{\beta_i}s_{\alpha_i} - \frac{1}{2}Lbc_{\beta_i}\right)E_5 \\ \sqrt{2}(-1)^{i+1}\left(q_id c_{\beta_i} + \frac{1}{2}Lbs_{\beta_i}s_{\alpha_i}\right)E_6 \end{array} \right\} \hat{\mathbf{e}}_i. \quad (3.19)$$

Necessarily, E_3 must be factorable from the third row of $A(\boldsymbol{\alpha}, \boldsymbol{\beta}, \mathbf{q})$, since $B(\boldsymbol{\alpha}, \boldsymbol{\beta}, \mathbf{q})$ is diagonal.

Specifically,

$$\sqrt{6}b[c_{\beta_1} \ c_{\beta_2} \ c_{\beta_3} \ c_{\beta_4} \ c_{\beta_5} \ c_{\beta_6}] = b_3E_3. \quad (3.20)$$

When considering the tilt model described by Eq. (2.11), the range of $\beta_i \in [0, \pi]$, and the row basis definition of Eq. (3.20), the solution set of β_i is restricted by the condition

$$\forall i(\beta_i = \beta). \quad (3.21)$$

A similar approach for reduction of the system may be taken for rows one and two of A_i . Substituting the reduced general parameterization developed for E_1^T and E_2^T in Eq. (3.11) in rows one and two of the column physical model basis A_i results

$$\begin{cases} b_1E_1(\zeta)\hat{\mathbf{e}}_i = -\sqrt{3}bs_{\beta}(c_{\alpha_i}E_5 + s_{\alpha_i}E_4)\hat{\mathbf{e}}_i = b_1(-1)^i(\zeta_1E_4 + \zeta_2E_5)\hat{\mathbf{e}}_i \\ b_2E_2^T(\zeta)\hat{\mathbf{e}}_i = \sqrt{3}bs_{\beta}(c_{\alpha_i}E_4 - s_{\alpha_i}E_5)\hat{\mathbf{e}}_i = b_2(-1)^i(\zeta_3E_4 + \zeta_4E_5)\hat{\mathbf{e}}_i \end{cases} \Rightarrow \begin{cases} \left(\left(c_{\alpha_i} - (-1)^{i+1} \frac{b_1\zeta_2}{\sqrt{3}bs_{\beta}} \right) E_5 + \left(s_{\alpha_i} - (-1)^{i+1} \frac{b_1\zeta_1}{\sqrt{3}bs_{\beta}} \right) E_4 \right) \hat{\mathbf{e}}_i = 0 \\ \left(\left(c_{\alpha_i} - (-1)^i \frac{b_2\zeta_3}{\sqrt{3}bs_{\beta}} \right) E_4 + \left(-s_{\alpha_i} + (-1)^{i+1} \frac{b_2\zeta_4}{\sqrt{3}bs_{\beta}} \right) E_5 \right) \hat{\mathbf{e}}_i = 0 \end{cases} \quad (3.22)$$

These two results imply linear independence relationships between the cofactors of the vector bases E_4 and E_5 . By design E_4 is orthogonal to E_5 , thus any formulation of the form $c_0E_4 + c_1E_5 = 0$ for scalar coefficients c_0 and c_1 , imply $c_0 = 0$ and $c_1 = 0$. Thus,

$$c_{\alpha_i} = (-1)^{i+1} \frac{b_1 \zeta_2}{\sqrt{3} b s_\beta} = (-1)^i \frac{b_2 \zeta_3}{\sqrt{3} b s_\beta}, \quad (3.23)$$

$$s_{\alpha_i} = (-1)^{i+1} \frac{b_1 \zeta_1}{\sqrt{3} b s_\beta} = (-1)^{i+1} \frac{b_2 \zeta_4}{\sqrt{3} b s_\beta},$$

For $\alpha_i \in [-\pi, \pi)$, the set of solutions for α is parameterized by $\alpha = \alpha_1 = \alpha_3 = \alpha_5$ and $\alpha_2 = \alpha_4 = \alpha_6 =$

$\begin{cases} \alpha + \pi & \alpha \leq 0 \\ \alpha - \pi & \alpha > 0 \end{cases}$. With the parameterization of β_i and α_i , a solution set for q_i becomes accessible.

Inspection of the sixth row of A_i with inclusion of the parameterizations results

$$\sqrt{2} \left((-1)^{i+1} q_i d c_\beta + \frac{1}{2\sqrt{3}} L b_1 \zeta_1 \right) E_6 \hat{e}_i = b_6 E_6 \hat{e}_i. \quad (3.24)$$

Necessarily, the form of q_i is then,

$$\forall i (q_i = (-1)^{i+1} q_1). \quad (3.25)$$

An important conclusion from this result is the inclusion of two distinct possible solution sets depending on the spin of rotor 1. Finally, inspection of rows four and five of A_i with all parameterizations results

$$-\frac{q_1 d b_1}{\sqrt{3} b} \zeta_2 E_5 + \left(-\left(\frac{q_1 d b_1}{\sqrt{3} b} \zeta_1 - \frac{1}{2} L b c_\beta \right) - b_4 \right) E_4 = 0, \quad (3.26)$$

$$\frac{q_1 d b_1}{\sqrt{3} b} \zeta_2 E_4 + \left(-\left(\frac{q_1 d b_1}{\sqrt{3} b} \zeta_1 - \frac{1}{2} L b c_\beta \right) - b_5 \right) E_5 = 0.$$

Like all parameterizations that preceded Eq. (3.26), a linear independence condition arises when formulated in this way. Because E_4 must be factorable from the fourth row of A_i and E_5 must be factorable from the fifth row of A_i , $\zeta_2 = 0$, and

$$\forall i \left(\alpha_i = \pm (-1)^{i+1} \frac{\pi}{2} \right). \quad (3.27)$$

For convenience the row bases

$$E_x = \frac{1}{\sqrt{3}} \begin{bmatrix} \frac{1}{2} & -1 & \frac{1}{2} & \frac{1}{2} & -1 & \frac{1}{2} \end{bmatrix}, \quad (3.28)$$

$$E_y = \begin{bmatrix} \frac{1}{2} & 0 & -\frac{1}{2} & \frac{1}{2} & 0 & -\frac{1}{2} \end{bmatrix},$$

are introduced to simplify final solution definitions. Applying Eq. (3.21), Eq. (3.25), and Eq. (3.27) allows expression of the motor mapping column basis as

$$A_i = \sqrt{3} \left\{ \begin{array}{l} \pm bs_\beta E_x \\ \pm bs_\beta E_y \\ \sqrt{2} bc_\beta E_3 \\ \left(\mp q_1 ds_\beta + \frac{1}{2} Lbc_\beta \right) E_4 \\ \left(\mp q_1 ds_\beta + \frac{1}{2} Lbc_\beta \right) E_5 \\ \sqrt{2} \left(q_1 dc_\beta \pm \frac{1}{2} Lbs_\beta \right) E_6 \end{array} \right\} \hat{e}_i. \quad (3.29)$$

The final decomposition of $A(\boldsymbol{\alpha}, \boldsymbol{\beta}, \boldsymbol{q})$ defined in Eq. (3.7) is then

$$\mathbf{b}(\boldsymbol{\alpha}, \boldsymbol{\beta}, \boldsymbol{q}) := \mathbf{b}(\text{sgn}(\alpha), \beta, q_1) = \left\{ \begin{array}{l} \pm\sqrt{3}bs_\beta \\ \pm\sqrt{3}bs_\beta \\ \sqrt{6}bc_\beta \\ \sqrt{3} \left(\mp q_1 ds_\beta + \frac{1}{2} Lbc_\beta \right) \\ \sqrt{3} \left(\mp q_1 ds_\beta + \frac{1}{2} Lbc_\beta \right) \\ \sqrt{6} \left(q_1 dc_\beta \pm \frac{1}{2} Lbs_\beta \right) \end{array} \right\}, \quad (3.30)$$

$$E = \left\{ \begin{array}{l} E_x \\ E_y \\ E_3 \\ E_4 \\ E_5 \\ E_6 \end{array} \right\} = \begin{bmatrix} \frac{1}{2\sqrt{3}} & -\frac{1}{\sqrt{3}} & \frac{1}{2\sqrt{3}} & \frac{1}{2\sqrt{3}} & -\frac{1}{\sqrt{3}} & \frac{1}{2\sqrt{3}} \\ \frac{1}{2} & 0 & -\frac{1}{2} & \frac{1}{2} & 0 & -\frac{1}{2} \\ \frac{1}{\sqrt{6}} & \frac{1}{\sqrt{6}} & \frac{1}{\sqrt{6}} & \frac{1}{\sqrt{6}} & \frac{1}{\sqrt{6}} & \frac{1}{\sqrt{6}} \\ -\frac{1}{2\sqrt{3}} & -\frac{1}{\sqrt{3}} & -\frac{1}{2\sqrt{3}} & \frac{1}{2\sqrt{3}} & \frac{1}{\sqrt{3}} & \frac{1}{2\sqrt{3}} \\ -\frac{1}{2} & 0 & \frac{1}{2} & \frac{1}{2} & 0 & -\frac{1}{2} \\ \frac{1}{\sqrt{6}} & -\frac{1}{\sqrt{6}} & \frac{1}{\sqrt{6}} & -\frac{1}{\sqrt{6}} & \frac{1}{\sqrt{6}} & -\frac{1}{\sqrt{6}} \end{bmatrix}, \quad (3.31)$$

where $\mathbf{b}(\boldsymbol{\alpha}, \boldsymbol{\beta}, \mathbf{q})$ was defined as a vector in \mathbb{R}^6 containing the diagonal elements of $B(\boldsymbol{\alpha}, \boldsymbol{\beta}, \mathbf{q})$ in Eq. (3.6). Depending on the sign of α and q_1 , there are 4 sets of solutions parameterized by β . Figure 3.2 shows these four parameterized solutions for all combinations of α and q_1 .

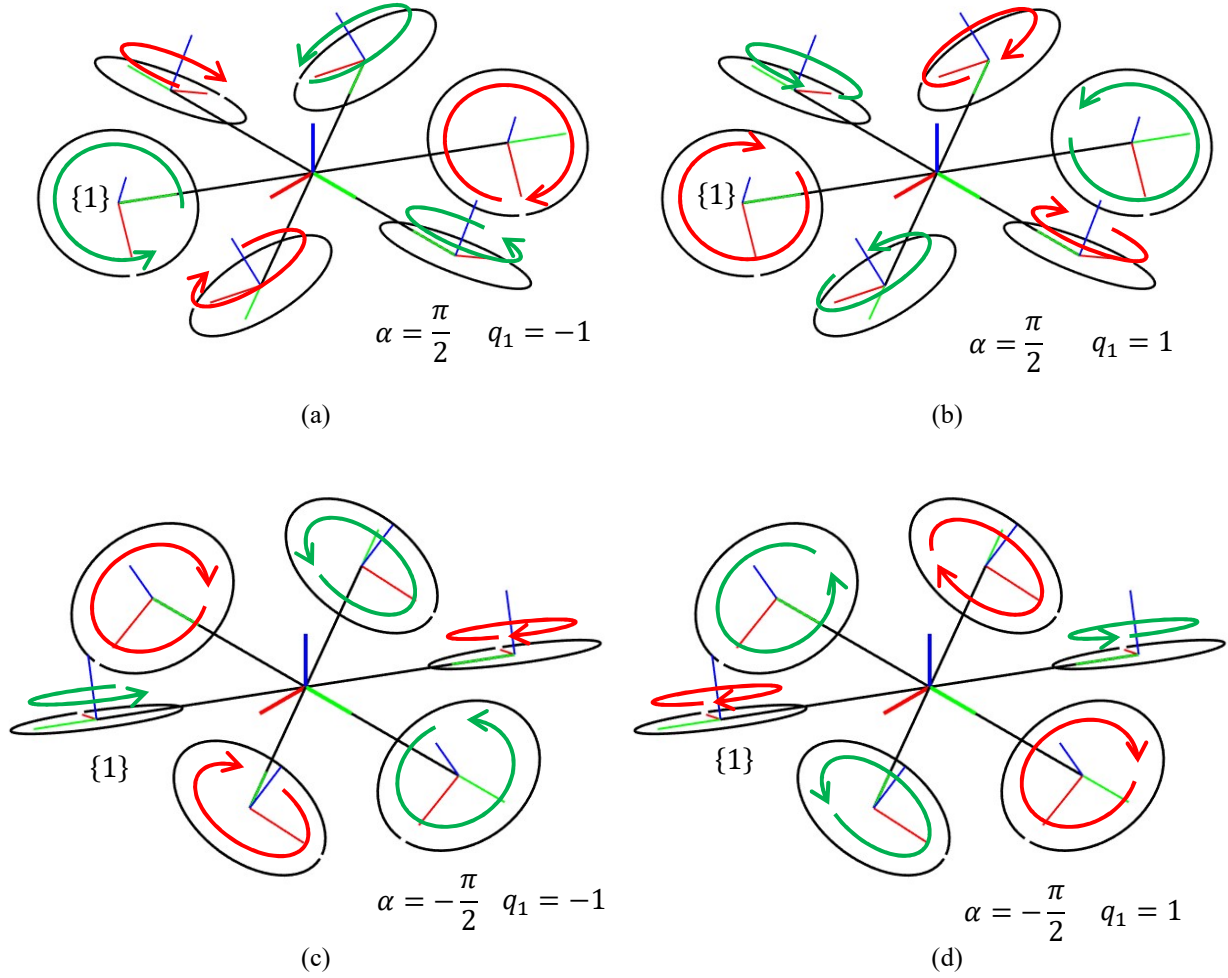


Figure 3.2. Four solution sets parameterized by the tilt angle β . (a) CCW propeller spin, with $\alpha = \frac{\pi}{2}$. (b) CW propeller spin, with $\alpha = \frac{\pi}{2}$. (c) CCW propeller spin, with $\alpha = -\frac{\pi}{2}$. (d) CW propeller spin, with $\alpha = -\frac{\pi}{2}$.

4 Optimization and Rotor Saturation

In Eq. (3.30) and Eq. (3.31), all possible fully-actuated flight stack solutions which are APM compliant were parameterized in terms of the design tilt β . There are four distinct setups which vary based on propeller spin and α rotation as shown in Figure 3.2. The reasoning follows from Eq. (2.15) and Eq. (2.14), wherein the thrust and drag action axis for each rotor projects onto the body fixed frame z-axis ${}^B\mathbf{Z}$ as a function of only β for model class \mathcal{F}_{S_1} . In this section, efficiency metrics are determined based on the comparison of nonparallel multirotor of class \mathcal{F}_{S_1} and parallel multirotor of class \mathcal{F}_J . Second the efficiency metrics are discussed in terms of the rotor speed space constraints. By decomposing the problem using norm metrics, a key component of the design topology is lost, thus a discussion of the 6th dimensional speed constraints was necessary. Lastly, a discussion of cross-span compensation is introduced to provide options for adjusting power metrics.

4.1 Power and Force Efficiency Metrics

In this analysis the quality of force/torque production was determined as a function of the design parameters. One metric for determining this quality is the expression of necessary total power P_t required to produce a specified control effort \mathbf{T}_u . For any DC system, power is proportional to the square current I^2 , such that $P_t = Z_e I^2$, where Z_e is some constant electrical impedance. A brushless DC motor possesses an approximate relationship between rotor speed and current of the form $I = K_e \omega_i^2$, where K_e is some constant mechanical impedance. Thus, power necessary to actuate a multirotor can be written as a function of rotor speed $P_t = Z_e K_e \omega_i^4 \propto \|\boldsymbol{\omega}\|_2^2$. The square L_2 -norm of the rotor speed vector $\boldsymbol{\omega}$ is

$$\begin{aligned} \|\boldsymbol{\omega}\|_2^2 &= \|E^T \mathbf{u}\|_2^2 = \|E^T B^{-1}(\boldsymbol{\alpha}, \boldsymbol{\beta}, \mathbf{q}) \boldsymbol{\Gamma}_u\|_2^2 = \left\| E_1^T \begin{pmatrix} F_x \\ b_1 \end{pmatrix} + E_2^T \begin{pmatrix} F_y \\ b_2 \end{pmatrix} + E_3^T \begin{pmatrix} F_z \\ b_3 \end{pmatrix} + \right. \\ &\left. E_4^T \begin{pmatrix} \tau_x \\ b_4 \end{pmatrix} + E_5^T \begin{pmatrix} \tau_y \\ b_5 \end{pmatrix} + E_6^T \begin{pmatrix} \tau_z \\ b_6 \end{pmatrix} \right\|_2^2, \end{aligned} \quad (4.1)$$

where the scalar force expressions F_x , F_y , and F_z , and scalar torque expressions τ_x , τ_y , and τ_z correspond to a user-desired force and torque. In this expression, the necessary power is quantified as a function of a constant force/torque among two designs. An added benefit of the decoupled orthogonal decomposition, necessitates that the bases E_i^T impose a strong equality on the general 6th dimensional norm triangle inequality

$$\|\boldsymbol{\omega}\|_2 = \|\sum_i \boldsymbol{\omega}_i\|_2 = \|\boldsymbol{\omega}_1\|_2 + \|\boldsymbol{\omega}_2\|_2 + \|\boldsymbol{\omega}_3\|_2 + \|\boldsymbol{\omega}_4\|_2 + \|\boldsymbol{\omega}_5\|_2 + \|\boldsymbol{\omega}_6\|_2. \quad (4.2)$$

The vector quantities $\boldsymbol{\omega}_1$, $\boldsymbol{\omega}_2$, $\boldsymbol{\omega}_3$, $\boldsymbol{\omega}_4$, $\boldsymbol{\omega}_5$, and $\boldsymbol{\omega}_6$, which were introduced in Eq. (3.3) correspond to individual rotor speed combinations which produced decoupled forces along the UAV body-fixed x-, y-, and z-axes F_x , F_y , and F_z , and decoupled torques about the UAV body-fixed x-, y-, and z-axes τ_x , τ_y , and τ_z . The power metric $\|\boldsymbol{\omega}_i\|_2^2$ for each of the six axes of force/torque production is then

$$\begin{aligned}
\|\boldsymbol{\omega}_1\|_2^2 &= \left(\frac{F_x}{b_1}\right)^2, \\
\|\boldsymbol{\omega}_2\|_2^2 &= \left(\frac{F_y}{b_2}\right)^2, \\
\|\boldsymbol{\omega}_3\|_2^2 &= \left(\frac{F_z}{b_3}\right)^2, \\
\|\boldsymbol{\omega}_4\|_2^2 &= \left(\frac{\tau_x}{b_4}\right)^2, \\
\|\boldsymbol{\omega}_5\|_2^2 &= \left(\frac{\tau_y}{b_5}\right)^2, \\
\|\boldsymbol{\omega}_6\|_2^2 &= \left(\frac{\tau_z}{b_6}\right)^2.
\end{aligned} \tag{4.3}$$

Considering all 6 axes of force/torque production, using this formulation allows for the comparison of the quality of production between various designs of multirotor of classes \mathcal{F}_{S_1} and \mathcal{F}_J . Given a constant desired force/torque signal \boldsymbol{F}_u , the necessary effort $\|\boldsymbol{\omega}_{i(\mathcal{M})}\|_2^2$ for $i = 1, 2, \dots, 6$ of a general hexrotor model of class $\mathcal{F}_{\mathcal{M}}$ can be derived. Models types \mathcal{F}_{S_1} and \mathcal{F}_J correspond to the designed nonparallel hexrotor and a parallel underactuated hexrotor developed in this paper, and can be described by Eq. (3.30) and Eq. (3.31) for $\beta > 0$ and $\beta = 0$, respectively. The square L_2 -norm for the forces F_x , F_y , and F_z , and torques τ_x , τ_y , and τ_z are derived in terms of the power metrics $\|\boldsymbol{\omega}_{i(S_1)}\|_2^2$ and $\|\boldsymbol{\omega}_{i(J)}\|_2^2$ in

$$\begin{aligned}
\|F_x\|_2^2 &= b_1^2 \|\boldsymbol{\omega}_1\|_2^2 = 3b^2 s_\beta^2 \|\boldsymbol{\omega}_{1(S_1)}\|_2^2, \\
\|F_y\|_2^2 &= b_2^2 \|\boldsymbol{\omega}_2\|_2^2 = 3b^2 s_\beta^2 \|\boldsymbol{\omega}_{2(S_1)}\|_2^2, \\
\|F_z\|_2^2 &= b_3^2 \|\boldsymbol{\omega}_3\|_2^2 \Rightarrow 6b^2 c_\beta^2 \|\boldsymbol{\omega}_{3(S_1)}\|_2^2 = 6b^2 \|\boldsymbol{\omega}_{3(J)}\|_2^2,
\end{aligned} \tag{4.4}$$

$$\|\tau_x\|_2^2 = b_4^2 \|\omega_4\|_2^2 \Rightarrow 3 \left(\mp q_1 d s_\beta + \frac{1}{2} L b c_\beta \right)^2 \|\omega_{4(s_1)}\|_2^2 = \frac{3}{4} L^2 b^2 \|\omega_{4(j)}\|_2^2,$$

$$\|\tau_y\|_2^2 = b_5^2 \|\omega_5\|_2^2 \Rightarrow 3 \left(\mp q_1 d s_\beta + \frac{1}{2} L b c_\beta \right)^2 \|\omega_{5(s_1)}\|_2^2 = \frac{3}{4} L^2 b^2 \|\omega_{5(j)}\|_2^2,$$

$$\|\tau_z\|_2^2 = b_6^2 \|\omega_6\|_2^2 \Rightarrow 6 \left(q_1 d c_\beta \pm \frac{1}{2} L b s_\beta \right)^2 \|\omega_{6(s_1)}\|_2^2 = 6 d^2 \|\omega_{6(j)}\|_2^2.$$

Since parallel hexrotors of type j cannot produce forward or lateral forces F_x and F_y , no efficiency metric can be created for these axes, however, the ratio of the power metrics for the defined throttle, roll, pitch, and yaw axes for types i and j result 4 efficiency metrics ϵ_z , ϵ_{τ_x} , ϵ_{τ_y} , and ϵ_{τ_z} formulated as

$$\epsilon_z = \left(\frac{\|\omega_{3(j)}\|_2}{\|\omega_{3(s_1)}\|_2} \right)^2 = c_\beta^2,$$

$$\epsilon_{\tau_x} = \left(\frac{\|\omega_{4(j)}\|_2}{\|\omega_{4(s_1)}\|_2} \right)^2 = \left(\mp 2 q_1 \frac{d}{L b} s_\beta + c_\beta \right)^2,$$

(4.5)

$$\epsilon_{\tau_y} = \left(\frac{\|\omega_{5(j)}\|_2}{\|\omega_{5(s_1)}\|_2} \right)^2 = \left(\mp 2 q_1 \frac{d}{L b} s_\beta + c_\beta \right)^2,$$

$$\epsilon_{\tau_z} = \left(\frac{\|\omega_{6(j)}\|_2}{\|\omega_{6(s_1)}\|_2} \right)^2 = \left(\frac{q_1 \frac{d}{L b} c_\beta \pm \frac{1}{2} s_\beta}{\frac{d}{L b}} \right)^2,$$

The efficiency metrics represent a scalable quality for determining the amount of power necessary to produce decoupled throttle $P_{F_z(\mathcal{M})}$ roll $P_{\tau_x(\mathcal{M})}$, pitch $P_{\tau_y(\mathcal{M})}$, and yaw $P_{\tau_z(\mathcal{M})}$ for a nonparallel multirotor of type \mathcal{F}_{S_1} compared to a standard parallel multirotor of type \mathcal{F}_j such that

$$\begin{aligned}
P_{F_z(\mathcal{J})} &= \epsilon_{F_z} P_{F_z(\mathcal{S}_1)}, \\
P_{\tau_x(\mathcal{J})} &= \epsilon_{\tau_x} P_{\tau_x(\mathcal{S}_1)}, \\
P_{\tau_y(\mathcal{J})} &= \epsilon_{\tau_y} P_{\tau_y(\mathcal{S}_1)}, \\
P_{\tau_z(\mathcal{J})} &= \epsilon_{\tau_z} P_{\tau_z(\mathcal{S}_1)}.
\end{aligned} \tag{4.6}$$

It should be noted, however, that as a normed metric, these efficiencies simply correlate to the amount of power each model type requires to generate the same force/torque expression. This does not guarantee that both models will be capable of producing all possible force/torque expressions. In other words, the constraints on the rotor speed vector $\boldsymbol{\omega}$ must be developed in order to accurately depict a platform's capabilities. Clearly, higher power consumption implies larger rotor speed differentials, which imply less tolerance concerning rotor saturation.

Lastly, an efficiency metric is introduced for forward and lateral force production in

$$\begin{aligned}
\epsilon_n &= \frac{\|F_x + F_y\|_2^2}{\|F_z\|_2^2} = \frac{1}{2} t_\beta^2 \left(\frac{u_1'^2 + u_2'^2}{u_3'^2} \right) = \frac{1}{2} t_\beta^2 c_p, \\
c_p &:= \left(\frac{u_1'^2 + u_2'^2}{u_3'^2} \right).
\end{aligned} \tag{4.7}$$

Because all forms of force and torque production are dependent on the inclusion of throttle, this metric compares the total forward/lateral plane force production to throttle force production. For finite control authority, higher ϵ_n values imply lower energy requirements for planar force expression, and a higher threshold for saturation. This metric is a normed metric which does not describe the geometry of the constraints, which map the rotor speed space.

4.2 Rotor Speed Constraints and Saturation

The rotor speed constraints concern the possible differentials that a multirotor can create to produce forces and torques. While the previous section introduced metrics derived from the norm of rotor speed $\|\boldsymbol{\omega}\|_2^2$, these metrics do not consider multirotor geometry. There is an inherent restriction on rotor speed which necessitates the development of constraint equations. Thus, the form of specific rotor speed combinations are discussed in this section. While, in practice, all six axes of forward, lateral, throttle, roll, pitch, and yaw are actively involved in wrench production, torque generation is by nature a regulated system. It is not unreasonable to define then a metric for analyzing decoupled forces of fully-actuated hexrotor models. Finally, the overall flight performance was discussed. Rather the constraints which define multirotor capabilities in the production of combined throttle and torque for basic flight attitude and altitude tracking were developed.

4.2.1 Arbitrary Force Constraints

The rotor speed combination to produce pure force in an arbitrary direction was denoted $\boldsymbol{\omega}_n$ and defined as the sum of rotor speed vectors allocating forward, lateral, and throttle forces $\boldsymbol{\omega}_1$, $\boldsymbol{\omega}_2$, and $\boldsymbol{\omega}_3$

$$\boldsymbol{\omega}_n = \boldsymbol{\omega}_1 + \boldsymbol{\omega}_2 + \boldsymbol{\omega}_3 = E_x^T u'_1 + E_y^T u'_2 + E_3^T u'_3 = \begin{Bmatrix} \frac{1}{\sqrt{6}} u'_3 + \frac{1}{2\sqrt{3}} u'_1 + \frac{1}{2} u'_2 \\ \frac{1}{\sqrt{6}} u'_3 - \frac{1}{\sqrt{3}} u'_1 \\ \frac{1}{\sqrt{6}} u'_3 + \frac{1}{2\sqrt{3}} u'_1 - \frac{1}{2} u'_2 \\ \frac{1}{\sqrt{6}} u'_3 + \frac{1}{2\sqrt{3}} u'_1 + \frac{1}{2} u'_2 \\ \frac{1}{\sqrt{6}} u'_3 - \frac{1}{\sqrt{3}} u'_1 \\ \frac{1}{\sqrt{6}} u'_3 + \frac{1}{2\sqrt{3}} u'_1 - \frac{1}{2} u'_2 \end{Bmatrix}. \quad (4.8)$$

The convenience of the decomposition developed in Eq. (3.30) and Eq. (3.31), allow for isolation of all design metrics in the diagonal mapping $B(\boldsymbol{\alpha}, \boldsymbol{\beta}, \boldsymbol{q})$. E by design, is composed of orthonormal bases which are static and common among all hexrotor models. This is due to the desired output axis design of $\boldsymbol{\omega} =$

$E^T \mathbf{u}'$. This conveniently makes parameterization of $\boldsymbol{\omega}_i$ applicable to a wide variety of airframes, and allows for the comparison of decoupled desired forces and torques u'_i . Since u'_i is scalar and measured in $\frac{rad^2}{s^2}$, it corresponds directly to the desired effort and power consumption in the 6th dimensional wrench system. An element-wise positive definite constraint must hold for $\boldsymbol{\omega}_n$ as multirotor rotors are designed to spin unidirectionally. While bidirectional motors exist, they are generally not used for UAV applications at large due to efficiency losses. The rotor speed constraints which define arbitrary force production then present as

$$\boldsymbol{\omega}_n \geq 0 \Rightarrow \begin{cases} -\frac{1}{2\sqrt{3}} \left(\frac{u'_1}{u'_3}\right) \pm \frac{1}{2} \left(\frac{u'_2}{u'_3}\right) \leq \frac{1}{\sqrt{6}} \\ \frac{1}{\sqrt{3}} \left(\frac{u'_1}{u'_3}\right) \leq \frac{1}{\sqrt{6}} \end{cases}. \quad (4.9)$$

The forward and lateral control authority elements u'_1 and u'_2 scaled by the throttle command u'_3 in Figure 4.1 result static non-dimensional quality measures for determining the limits of planar force expression in the forward and lateral dimensions. The UAV body-fixed frame \mathcal{B} is indicated on the figure using the axes ${}^B\mathbf{X}$ and ${}^B\mathbf{Y}$.

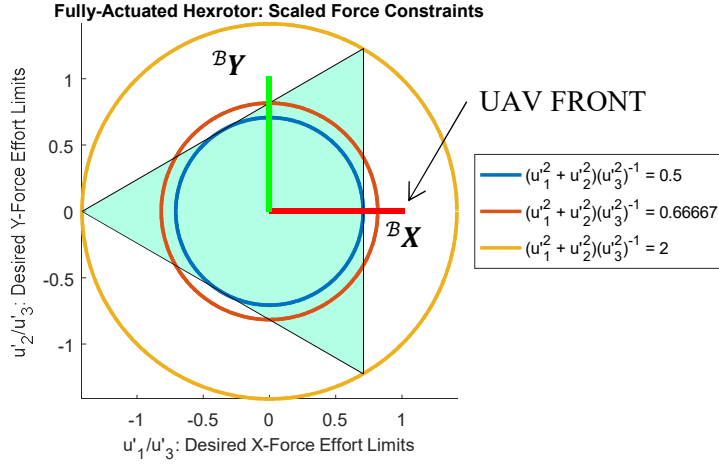


Figure 4.1. Projection of force constraints for a fully-actuated hexrotor.

The circular power factors, what was denoted in this analysis as $c_p = \frac{u_1'^2 + u_2'^2}{u_3'^2}$ indicated on Figure 4.1 correspond to the capability of nonparallel hexrotor in applying planar force as a ratio of vertical force in the normed sense. The indicated power factors calculated at $c_p = \frac{1}{2}$, $c_p = \frac{2}{3}$, and $c_p = 2$ correspond to maximum point efficiencies in the allocation of pure positive forward force, pure positive or negative lateral force, and negative forward force, respectively. By matching the rotor speed constraints with the normed power constraints, it becomes apparent that efficiency for planar force expression is directional. Referring to the planar force efficiency metric ϵ_n defined in Eq. (4.7), the aforementioned point efficiencies were calculated to be

$$\begin{aligned}
\epsilon_{n,x_+} &= \frac{1}{4} t_\beta^2, \\
\epsilon_{n,y_\pm} &= \frac{1}{3} t_\beta^2, \\
\epsilon_{n,x_-} &= t_\beta^2,
\end{aligned} \tag{4.10}$$

for ϵ_{n,x_+} corresponding to maximum possible positive forward force efficiency, maximum lateral force efficiency ϵ_{n,x_+} possible, and maximum negative forward force efficiency ϵ_{n,x_-} . Where their general definition $\epsilon_n \propto C_p$.

While the force projection is useful for finding maximum planar force allocation limitations, this particular analysis considered zero-torque loading. To maintain stable flight however, adequate throttle, roll, pitch, and yaw efforts must be allocated in the rotor speed space. This presents in the flight stack phase known as mixing. In the next section the constraints on altitude and attitude control effort was considered.

4.2.2 Throttle, Roll, Pitch, and Yaw Constraints

To analyze roll, pitch, and yaw control allocation, a combined rotor speed vector $\boldsymbol{\omega}_a$ was constructed from the summation of the decoupled speed vectors corresponding to the bases $\boldsymbol{\omega}_3$, $\boldsymbol{\omega}_4$, $\boldsymbol{\omega}_5$, and $\boldsymbol{\omega}_6$ in

$$\boldsymbol{\omega}_a = \boldsymbol{\omega}_3 + \boldsymbol{\omega}_4 + \boldsymbol{\omega}_5 + \boldsymbol{\omega}_6 = \begin{Bmatrix} \frac{1}{\sqrt{6}} u'_3 - \frac{1}{2\sqrt{3}} u'_4 - \frac{1}{2} u'_5 + \frac{1}{\sqrt{6}} u'_6 \\ \frac{1}{\sqrt{6}} u'_3 - \frac{1}{\sqrt{3}} u'_4 - \frac{1}{\sqrt{6}} u'_6 \\ \frac{1}{\sqrt{6}} u'_3 - \frac{1}{2\sqrt{3}} u'_4 + \frac{1}{2} u'_5 + \frac{1}{\sqrt{6}} u'_6 \\ \frac{1}{\sqrt{6}} u'_3 + \frac{1}{2\sqrt{3}} u'_4 + \frac{1}{2} u'_5 - \frac{1}{\sqrt{6}} u'_6 \\ \frac{1}{\sqrt{6}} u'_3 + \frac{1}{\sqrt{3}} u'_4 + \frac{1}{\sqrt{6}} u'_6 \\ \frac{1}{\sqrt{6}} u'_3 + \frac{1}{2\sqrt{3}} u'_4 - \frac{1}{2} u'_5 - \frac{1}{\sqrt{6}} u'_6 \end{Bmatrix}. \tag{4.11}$$

This notation mirrors that of the deficient rank control allocation matrix E_a defined in Eq. (3.9). As was developed in Eq. (4.9) for hexrotor force speed vector constraints, an element-wise positive definite constraint was placed on $\boldsymbol{\omega}_a$ resulting in

$$\boldsymbol{\omega}_a \geq 0 \Rightarrow \begin{cases} \frac{1}{2\sqrt{3}} \left(\frac{u'_4}{u'_3} \right) + \frac{1}{2} \left(\frac{u'_5}{u'_3} \right) - \frac{1}{\sqrt{6}} \left(\frac{u'_6}{u'_3} \right) \leq \frac{1}{\sqrt{6}} \\ \frac{1}{\sqrt{3}} \left(\frac{u'_4}{u'_3} \right) + \frac{1}{\sqrt{6}} \left(\frac{u'_6}{u'_3} \right) \leq \frac{1}{\sqrt{6}} \\ \frac{1}{2\sqrt{3}} \left(\frac{u'_4}{u'_3} \right) - \frac{1}{2} \left(\frac{u'_5}{u'_3} \right) - \frac{1}{\sqrt{6}} \left(\frac{u'_6}{u'_3} \right) \leq \frac{1}{\sqrt{6}} \\ -\frac{1}{2\sqrt{3}} \left(\frac{u'_4}{u'_3} \right) - \frac{1}{2} \left(\frac{u'_5}{u'_3} \right) + \frac{1}{\sqrt{6}} \left(\frac{u'_6}{u'_3} \right) \leq \frac{1}{\sqrt{6}} \\ -\frac{1}{\sqrt{3}} \left(\frac{u'_4}{u'_3} \right) - \frac{1}{\sqrt{6}} \left(\frac{u'_6}{u'_3} \right) \leq \frac{1}{\sqrt{6}} \\ -\frac{1}{2\sqrt{3}} \left(\frac{u'_4}{u'_3} \right) + \frac{1}{2} \left(\frac{u'_5}{u'_3} \right) + \frac{1}{\sqrt{6}} \left(\frac{u'_6}{u'_3} \right) \leq \frac{1}{\sqrt{6}} \end{cases}. \quad (4.12)$$

These constraints correspond to all possible attitude torque control effort scaled by throttle. Essentially, there can be no force or torque expression if a no-throttle state is commanded by the flight controller, since rotors are not considered bidirectional. As throttle increases, all other dimensional controls scale, hence the development of all constraints in this manner. The visualization of these attitude constraints results in the cube geometry of Figure 4.2. The cyan cube restricts the possible scaled effort of roll, pitch, and yaw effort for a given throttle output. Since the definition represents speed constraints in the basis E , this mapping is true for all commercial hexrotor regardless of design, as long as it is controllable using the compliant decoupled control scheme E_a .

Fully-Actuated Hexrotor: Scaled Torque Constraints

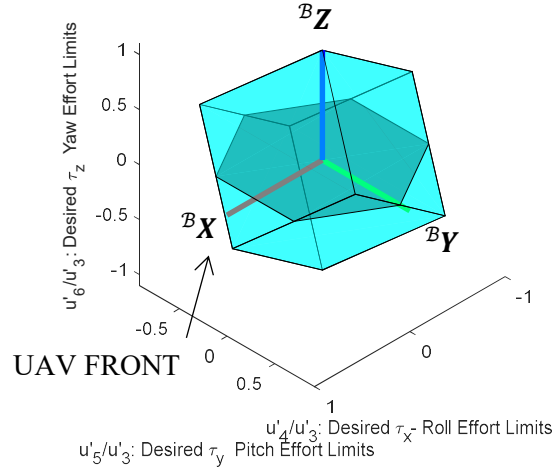


Figure 4.2. Isometric view of the hexrotor attitude speed constraint space.

The axes represented in the top view of the hexrotor attitude speed constraint space was given in Figure 4.3. In this view the roll/pitch planar constraints can be inspected for any given static yaw command. In the presented case, the hexagon in black indicates the roll/pitch speed constraint plane for a zero-yaw command offset, or $\frac{u'_6}{u'_3} = 0$ identically for all time t . This space indicates what percentage and in what combination roll and pitch commands may be requested for a zero-yaw torque condition, where the axis corresponding to BX implies the magnitude of scaled roll effort, and BY the axis corresponding to scaled pitch effort. The shape is informative of hexrotor geometry as there are six propellers placed equiangularly. Normed power factors such as c_p indicated in Figure 4.1, and the efficiencies developed in Eq. (4.5) and Eq. (4.7), fail to capture this geometry. This verifies the necessity of the comparison of these constraint spaces in the development of general power efficiencies.

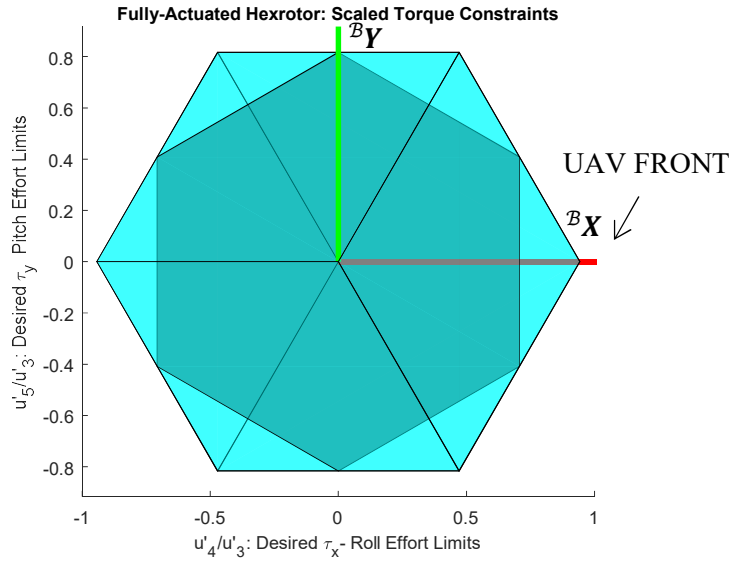


Figure 4.3. Top view of the hexrotor attitude speed constraint space.

The front and side views of the hexrotor attitude constraint space are given in Figure 4.4 as hexagonal and square, respectively.

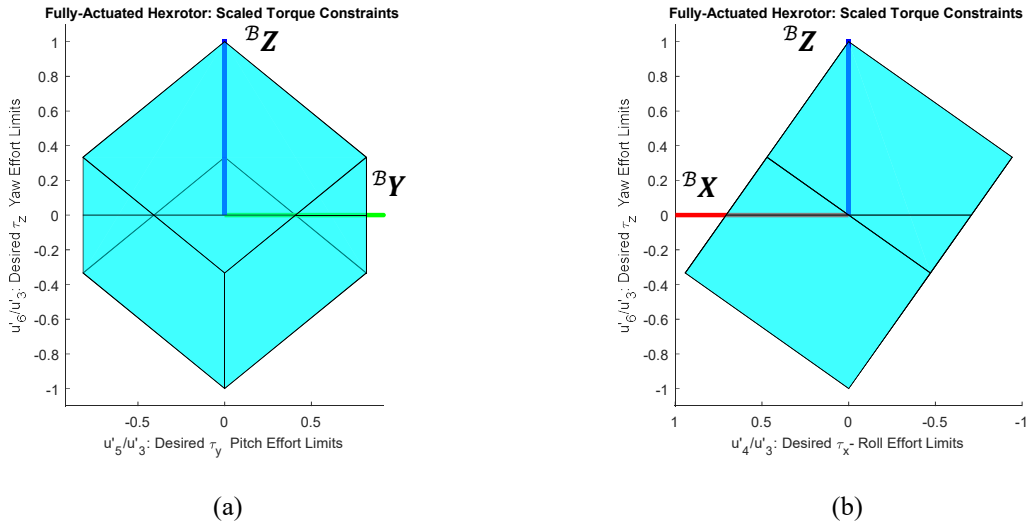


Figure 4.4. (a) Front view of the hexrotor attitude speed constraint space. (b) Side view of the hexrotor attitude speed constraint space.

The zero-yaw condition implies a symmetric distribution of both roll and pitch efforts within the constraint space. As a regulated system, yaw is generally maintained in this condition, thus the roll and pitch allocation plane can be represented by this constraint space adequately. If a hexrotor is given a non-zero yaw command, however, the shape of the roll/pitch allocation plane varies drastically. When considering the use-cases of a fully-actuated hexrotor, aerial manipulation is a major consideration in the regulation of attitude. Aerial manipulation implies the development of arbitrary wrenches in-situ, and involves careful attitude torque tracking. These demands must agree with flight requirements always, thus it is informative to develop the roll/pitch constraints for some non-zero yaw conditions. In Figure 4.5 an isometric view of the attitude rotor speed constraints for a 15% yaw to torque condition is shown. What this condition represents is a non-dimensional scaling of applied yaw to throttle $\frac{u'_6}{u'_3} = 0.15$. The space was shifted by 0.15 to display the intersecting roll/pitch plane.

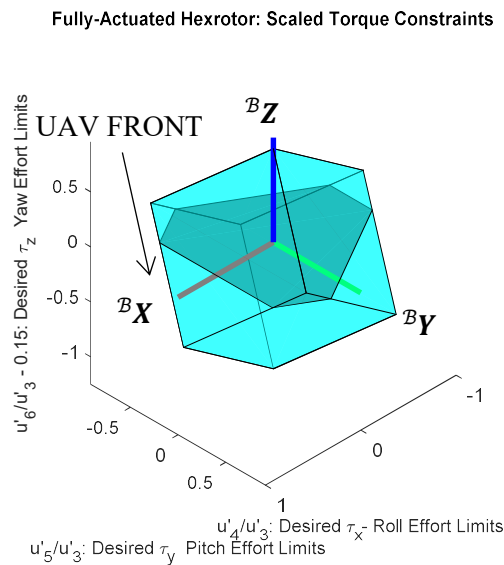


Figure 4.5. Isometric view of the hexrotor attitude speed constraints. Roll/pitch constraint plane for a 15% yaw to throttle offset command.

As can be shown in the top view of the constraint space in Figure 4.6, the hexagonal roll/pitch plane shape is deformed from the symmetric hexagon shape of Figure 4.3. While pitch effort remains symmetric, a clear deviation occurs between possible positive and negative roll control authority. If a UAV is in some positive yaw condition, its overall capability for negative roll increases, while its ability to perform positive roll, and both positive and negative pitch decreases.

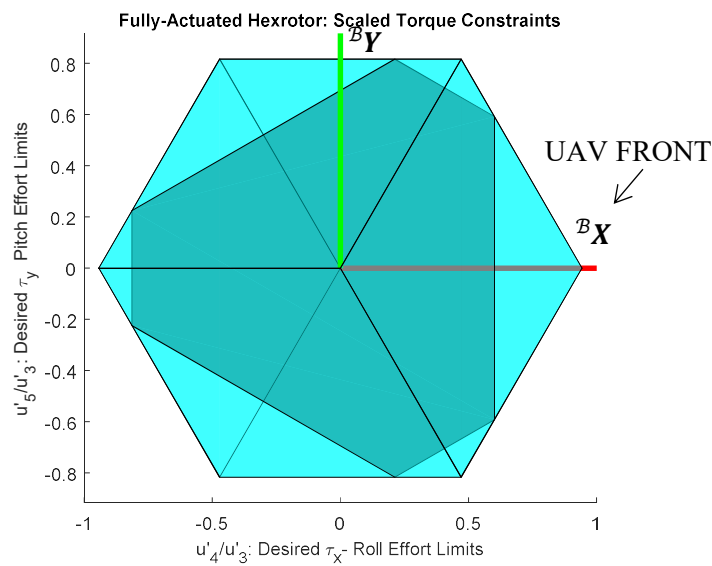


Figure 4.6. Top view of the hexrotor attitude speed constraints. Roll/pitch constraint plane for a 15% yaw to throttle offset command.

The front and side view of the constraint space in Figure 4.5 and Figure 4.6 were provided in Figure 4.7. The vertical shift in the space due to the positive 15% yaw to throttle offset is shown in the forward lateral views.

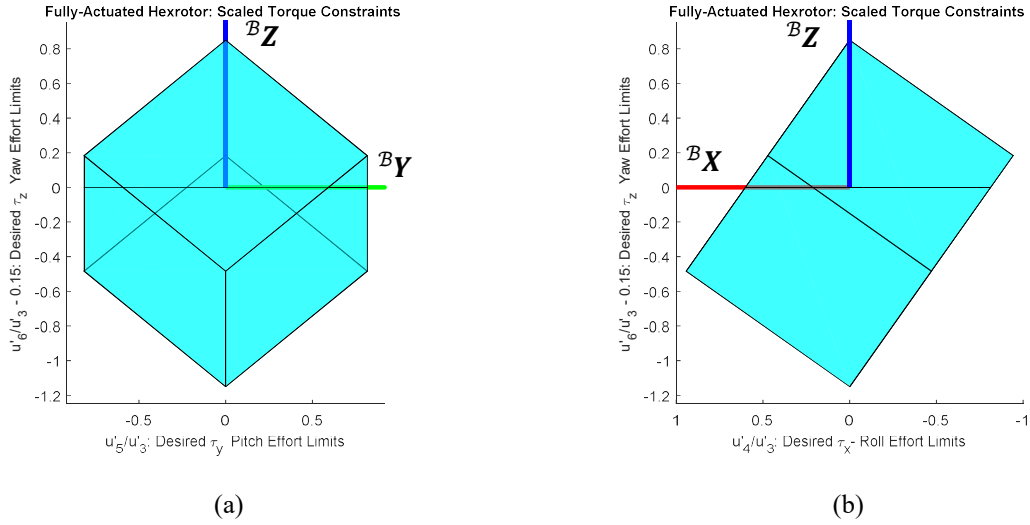


Figure 4.7. Roll/pitch constraint plane for a 15% yaw to throttle offset command. (a) Front view of the hexrotor attitude speed constraints. (b) Side view of the hexrotor attitude speed constraints.

By shifting the constraint space in the negative direction for the case shown in Figure 4.8, the deformation of the roll/pitch saturation plane presents a symmetric ${}^B Y$ axis inversion of the deformation in Figure 4.6.

The offset yaw command in this case was -15% scaled yaws to throttle command or $\frac{u'_6}{u'_3} = -0.15$.

Fully-Actuated Hexrotor: Scaled Torque Constraints

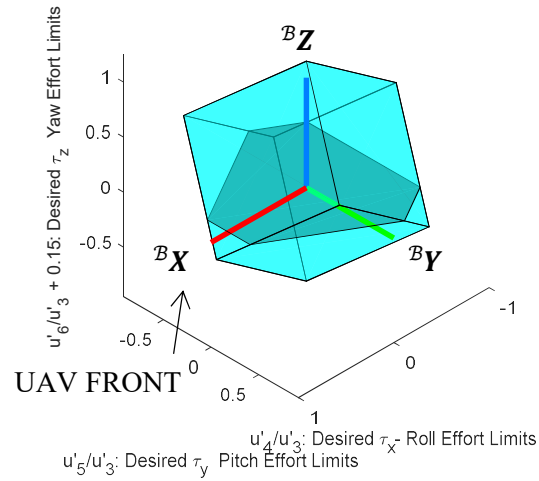


Figure 4.8. Isometric view of the hexrotor attitude speed constraints. Roll/pitch constraint plane for a -15% yaw to throttle offset command.

The top view of the constraint space introduced in Figure 4.8 is shown in Figure 4.9. The deformation of the roll/pitch constrain plane has shifted for a yaw to throttle command of -15% to allow for increased forward roll capability but decreased negative roll and both positive and negative pitch.

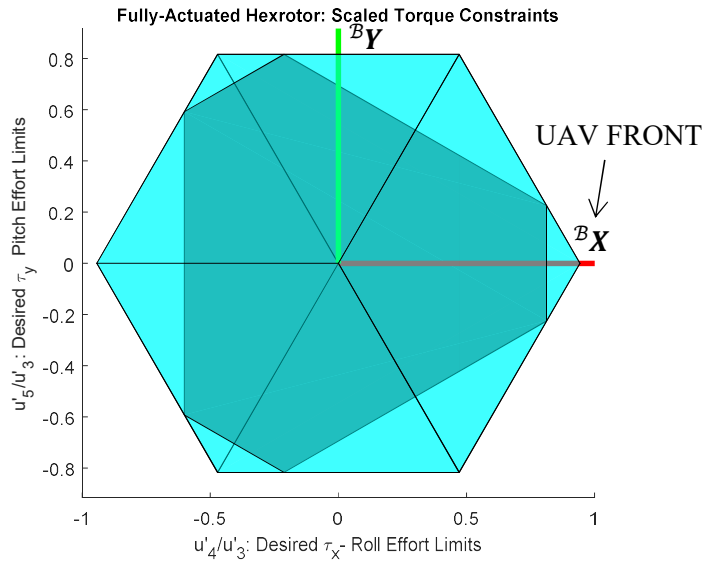


Figure 4.9. Top view of the hexrotor attitude speed constraints. Roll/pitch constraint plane for a -15% yaw to throttle offset command.

The front and side views for the negative yaw case is shown in Figure 4.10.

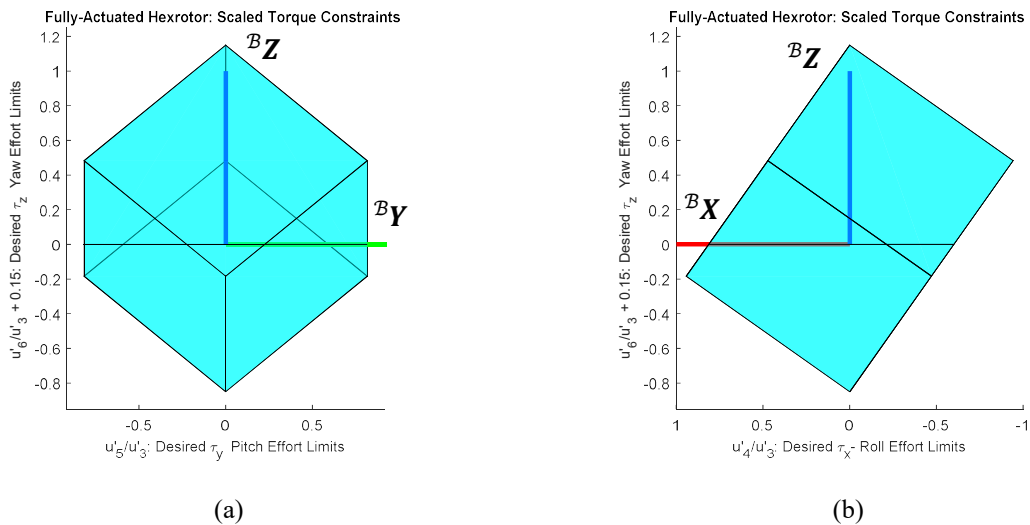


Figure 4.10. Roll/pitch constraint plane for a -15% yaw to throttle offset command. (a) Front view of the hexrotor attitude speed constraints. (b) Side view of the hexrotor attitude speed constraints.

Further inspection of the cube geometry of the hexrotor attitude constraint space reveals three distinct regions of consideration for roll/pitch torque production. The speed condition shown in Figure 4.11 was generated assuming a 33% yaw offset. When a 33% speed differential is created between yaw and throttle magnitudes u'_6 and u'_3 , respectively, the direction of max roll/pitch allocation ceases angular variation. Below $\left| \frac{u'_6}{u'_3} \right| = \frac{1}{3}$, peak allocation is possible in 6 distinct directions, as indicated by the 6 vertices of the shaded hexagon on Figure 4.3, Figure 4.6, and Figure 4.9. Depending on the magnitude and sign of the desired yaw command, the direction of these 6 points changed with mixed command ω_4 and ω_5 . At $\frac{u'_6}{u'_3} = \pm \frac{1}{3}$, the six directional points merge into three, and the direction of maximum roll/pitch allocation becomes fixed for yaw ratio magnitudes above $\frac{1}{3}$. The overall scaling, however, is reduced at ratios $\left| \frac{u'_6}{u'_3} \right| \geq \frac{1}{3}$ following the contour of the cube.

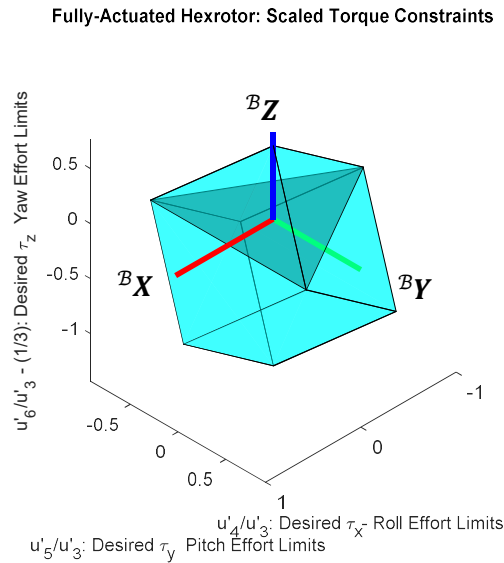


Figure 4.11. Isometric view of the hexrotor attitude speed constraints. Roll/pitch constraint plane for a 33% yaw to throttle offset command.

The top view of the attitude constraint space is shown in Figure 4.12. Having examined Figure 4.3, Figure 4.6, Figure 4.9, and Figure 4.12, maximum roll/pitch authority is achieved for a combined roll/pitch effort directed at some angle θ_{xy} measured about ${}^B\mathbf{Z}$, where $\tan \theta_{xy} = \left(\frac{u'_5}{u'_4}\right)$. The direction of maximum roll/pitch effort for the case where $\frac{u'_6}{u'_3} = \frac{1}{3}$ is $\theta_{xy} = \frac{\pi}{3}, \pi, \frac{5\pi}{3}$. This case also presents the global maximum for roll/pitch allocation for the entire attitude constraint space.

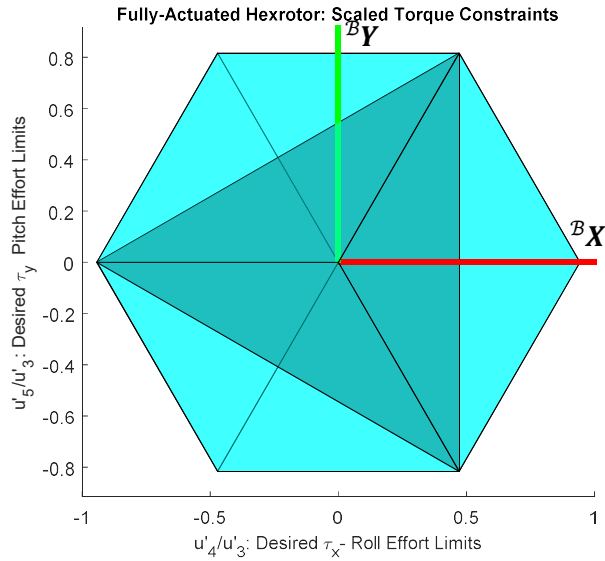


Figure 4.12. Top view of the hexrotor attitude speed constraints. Roll/pitch constraint plane for a 33% yaw to throttle offset command.

The front and side views of the constraint space for $\frac{u'_6}{u'_3} = \frac{1}{3}$ is shown in Figure 4.13.

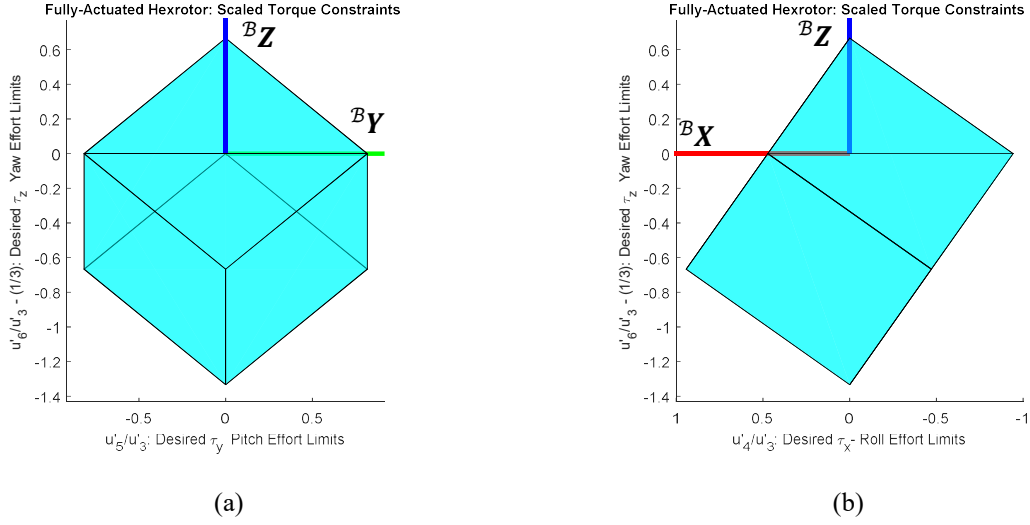


Figure 4.13. Roll/pitch constraint plane for a 33% yaw to throttle offset command. (a) Front view of the hexrotor attitude speed constraints. (b) Side view of the hexrotor attitude speed constraints.

As was derived in the previous sections, there are a finite number of configurations for fully-actuated hexrotor. While octocopter and higher order multirotor configurations possess more rotor units than a hexrotor, the dimensionality of wrench expressions exists in \mathbb{R}^6 . The hexrotor platform was chosen for special consideration as it possesses exactly six rotors. The reason quadcopters are so ubiquitous in multirotor design and analysis is they possess a square rotor mapping for the development of underactuated control of throttle, roll, pitch, and yaw, excluding forward and lateral considerations. The hexrotor and higher order multirotor are over-actuated for that \mathbb{R}^4 system, thus there is no unique inverse of the rotor mapping. Rather techniques such as the Moore-Penrose pseudo-inverse must be employed to generate a sufficient command signal [8]. Thus, for fully-actuated multirotor analysis in \mathbb{R}^6 , hexrotor exist as the fundamental airframe for design, as the inverse motor mapping is unique. The decomposition of the motor mapping of the form of $A(\alpha, \beta, q) = B(\alpha, \beta, q)E$ introduced in Eq. (3.7), does not apply for multirotor of order higher than six. For comparison however, the constraint spaces for higher and lower order multirotor can still be built using the directionality of γ . Recalling the basis equations of Eq. (3.18), n^{th} order general multirotor constraint equations can be constructed via

$$\boldsymbol{\omega}_n = \boldsymbol{\omega}_1 + \boldsymbol{\omega}_2 + \boldsymbol{\omega}_3 = E_x^T u'_1 + E_y^T u'_2 + E_3^T u'_3, \quad (4.13)$$

$$\boldsymbol{\omega}_a = \boldsymbol{\omega}_3 + \boldsymbol{\omega}_4 + \boldsymbol{\omega}_5 + \boldsymbol{\omega}_6 = E_3^T u'_3 + E_4^T u'_4 + E_5^T u'_5 + E_6^T u'_6, \quad (4.14)$$

respectively, where the n^{th} order basis vectors were chosen to be

$$\begin{aligned} E_x^T &:= - \left(\sqrt{\sum_{j=1}^n c_{\gamma_j}^2} \right)^{-1} \sum_{i=1}^n (-1)^i c_{\gamma_i} \hat{\mathbf{e}}_i, \\ E_y^T &:= \left(\sqrt{\sum_{j=1}^n s_{\gamma_j}^2} \right)^{-1} \sum_{i=1}^n (-1)^i s_{\gamma_i} \hat{\mathbf{e}}_i, \\ E_3^T &:= (\sqrt{n})^{-1} \sum_{i=1}^n \hat{\mathbf{e}}_i, \\ E_4^T &:= - \left(\sqrt{\sum_{j=1}^n c_{\gamma_j}^2} \right)^{-1} \sum_{i=1}^n c_{\gamma_i} \hat{\mathbf{e}}_i, \\ E_5^T &:= \left(\sqrt{\sum_{j=1}^n s_{\gamma_j}^2} \right)^{-1} \sum_{i=1}^n s_{\gamma_i} \hat{\mathbf{e}}_i, \\ E_6^T &:= -(\sqrt{n})^{-1} \sum_{i=1}^n (-1)^i \hat{\mathbf{e}}_i. \end{aligned} \quad (4.15)$$

It should be noted that this mapping was chosen for non-hexrotor airframes, however, there are no fixed mappings for higher order multirotor for the discussed reasons.

While quadcopter UAV cannot express arbitrary forward and lateral force projections, the attitude constraint space may still be visualized in the manner introduced in this section for the fully -actuated hexrotor. Figure 4.14 represents the attitude constraints for a quadcopter.

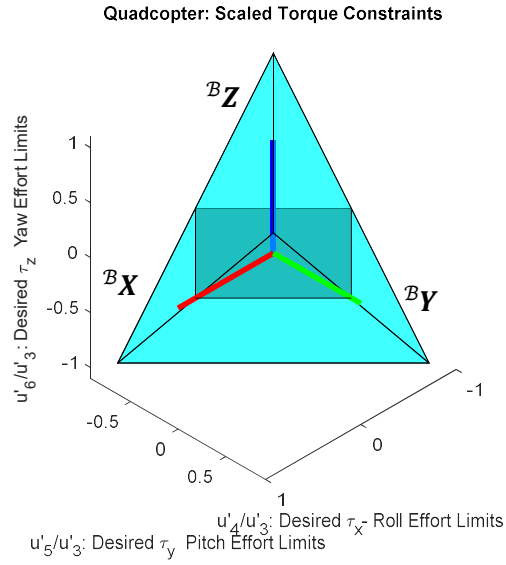


Figure 4.14. Isometric view of the quadcopter attitude speed constraints.

The top view of the space in Figure 4.15 reveals a square geometry for the roll/pitch constraint plane given a zero-yaw condition.

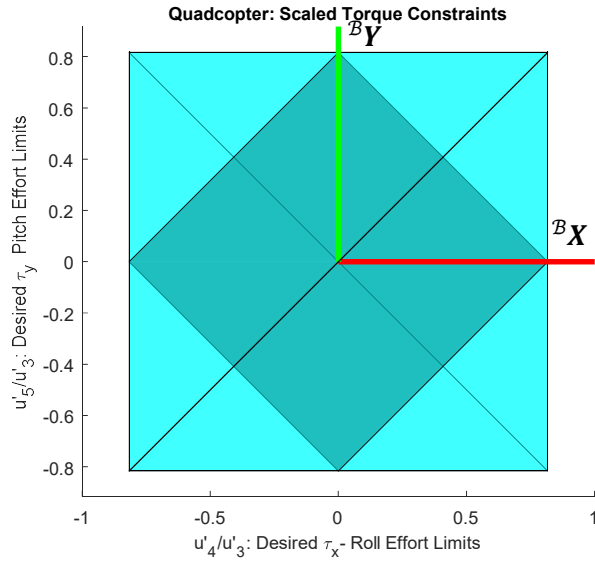


Figure 4.15. Top view of the quadcopter attitude speed constraints.

The front and side views of the quadcopter attitude speed constraints are shown in Figure 4.16.

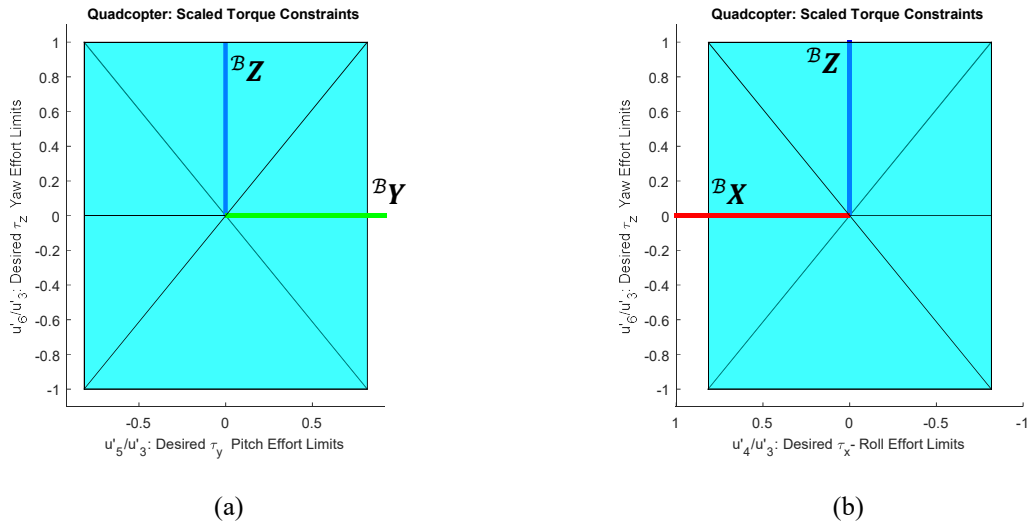


Figure 4.16. (a) Front view of the quadcopter attitude speed constraints. (b) Side view of the quadcopter attitude speed constraints.

The quadcopter constraint space agrees with in-situ application. Maximum roll/pitch presents as a square always, while the yaw limits the saturation plane to a line at peak yaw output.

Moving on to the analyses of higher order multirotor, the octocopter force projection plane is shown in Figure 4.18. A symmetric force plane is expressed about both ${}^B\mathbf{X}$ and ${}^B\mathbf{Y}$ axes. Because no rotors lie on fundamental axes, as was the case in the hexrotor constraint equations, octocopters possess a symmetric and objectively larger forward/lateral force plane expression than hexrotor platforms. While octocopters are heavier and expend more energy in general, this analysis suggests higher performance for octocopter platforms in aerial manipulation tasks due to the shape of the force constraint space.

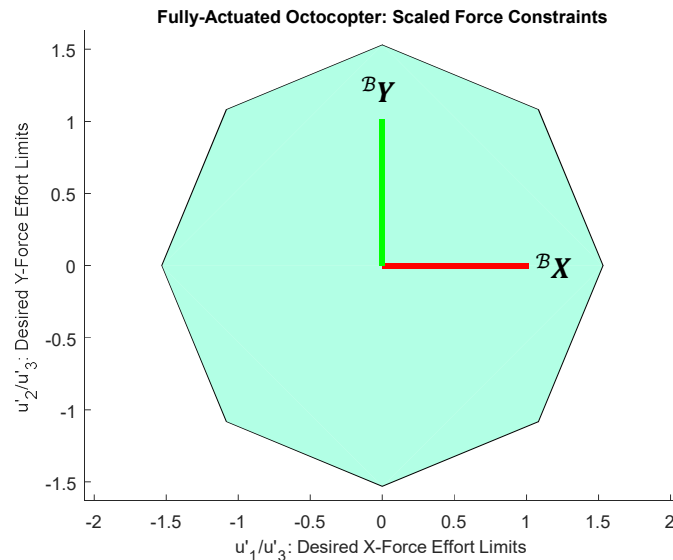


Figure 4.17. Projection of force constraints for a fully-actuated octocopter.

Octocopter attitude speed constraints are presented in Figure 4.18 as an octagonal 3-dimensional polygon. Much like the hexrotor attitude constraints presented in Figure 4.2, the roll/pitch condition for zero-yaw has been shown in black.

Fully-Actuated Octocopter: Scaled Torque Constraints

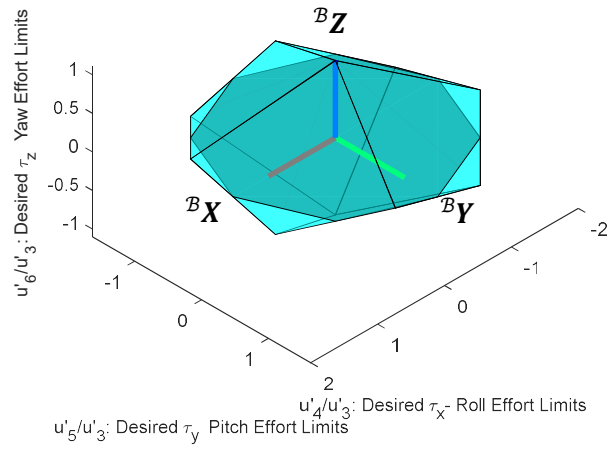


Figure 4.18. Isometric view of the octocopter attitude speed constraints.

The geometry of the attitude speed constraints can be seen from the top view in Figure 4.19. As expected, the roll/pitch plane at the zero-yaw condition is an equal octagon. The overall magnitude ratio of $\frac{u'_4}{u'_6}$ and $\frac{u'_5}{u'_6}$ presents as a much larger constraint space than that of the hexrotor model in Figure 4.3.

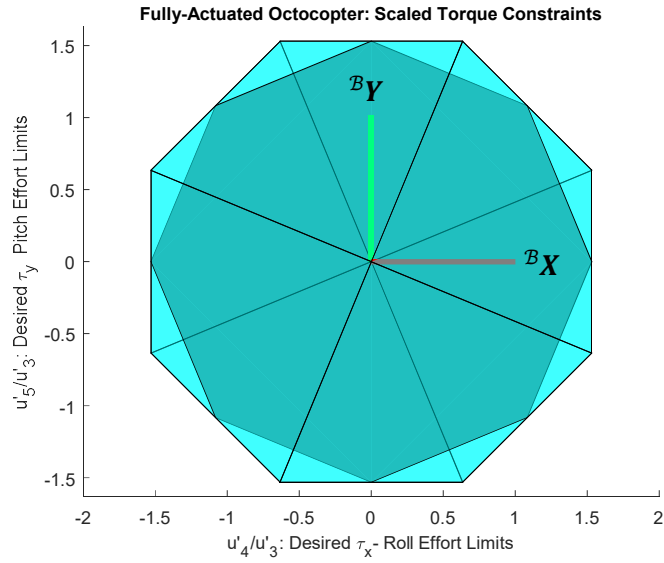


Figure 4.19. Top view of the octocopter attitude speed constraints.

The side and front views of the octocopter constraint space is shown in Figure 4.20.

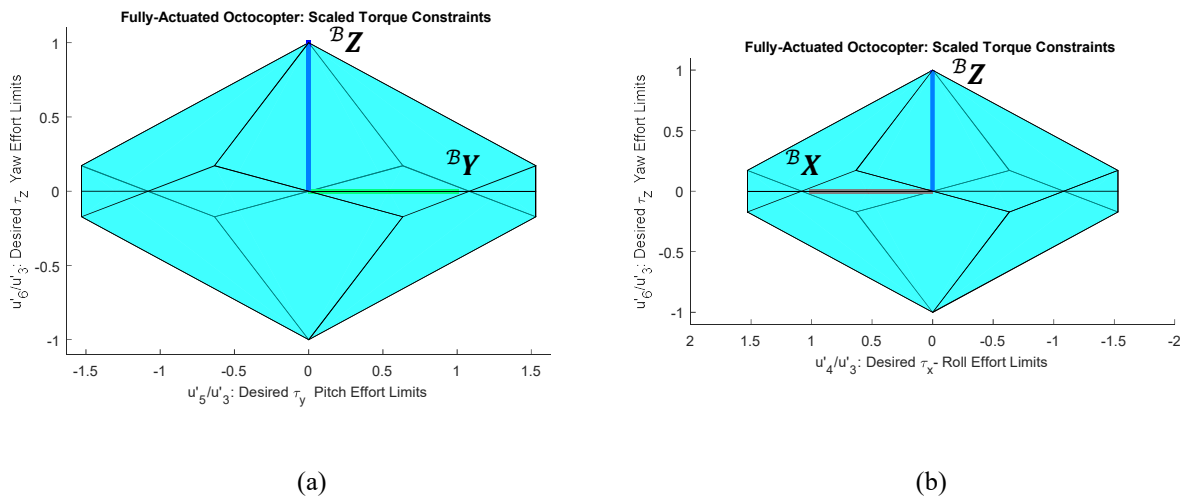


Figure 4.20. (a) Front view of the octocopter attitude speed constraints. (b) Side view of the octocopter attitude speed constraints.

The saturation limits on octocopter platforms are higher in a scaled sense due to both the symmetry of the constraint spaces and increased number of actuators. While this was an expected result, the pattern of geometries concerning force expressions was puzzling. Concerning octocopter attitude constraints, the zero-yaw condition yielded an octagonal roll/pitch constraint plane. Much like the hexrotor constraint geometry, an n -sided polygon is presented for a multirotor with n rotors. Further parallels can be observed from the front and side views of the constraint polygons. There are three distinct constraint geometries presented for varying yaw conditions. Above a certain commanded yaw ratio, the roll/pitch constraint polygon is of reduced order, presenting as a polygon of side count $\frac{n}{2}$, after which the fixed-shape orientation remains with scaled output. That is, the overall orientation of shape becomes fixed with yaw condition in that region. As both multirotor model attitude constraint spaces possessed such similarity, the reasoning for such widely different shape representation on the force constraint space prompted a shift in the focus of the analysis. Mathematically, the reasoning for the triangular constraint space of Figure 4.1 was caused by repeated constraints in Eq. (4.8) for the development of Eq. (4.9). While higher order multirotor are not in use commercially, inspection of their constraint spaces was used to infer the possible reasoning for the disparity in representation for force constraints between hexrotors and octocopters. To that end, the force and attitude constraints for a 10-rotor multirotor, called a decacopter were developed using the bases in Eq. (4.13), Eq. (4.14), and Eq. (4.15). The force plane constraints for the decacopter were developed from Eq. (4.13) in Figure 4.21.

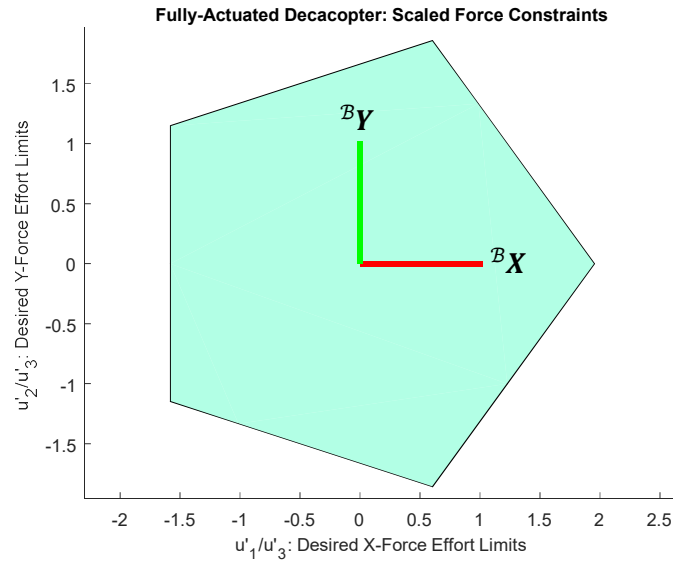


Figure 4.21. Projection of force constraints for a fully-actuated decacopter.

The force plane for the decacopter presents as a 5-sided pentagon. Much like the hexrotor platform, the force polygon possesses $\frac{n}{2}$ sides. Regardless of how the body-fixed frame is oriented, this force plane will always be of this reduced order. While initially counterintuitive, the result can be explained by the symmetry of design. An octocopter may be bisected symmetrically along both ${}^B\mathbf{X}$ and ${}^B\mathbf{Y}$. Both hexrotor and decacopter can be bisected symmetrically by at most one axis. Further inspection of the attitude constraints yielded Figure 4.22 for the decacopter design.

Fully-Actuated Decacopter: Scaled Torque Constraints

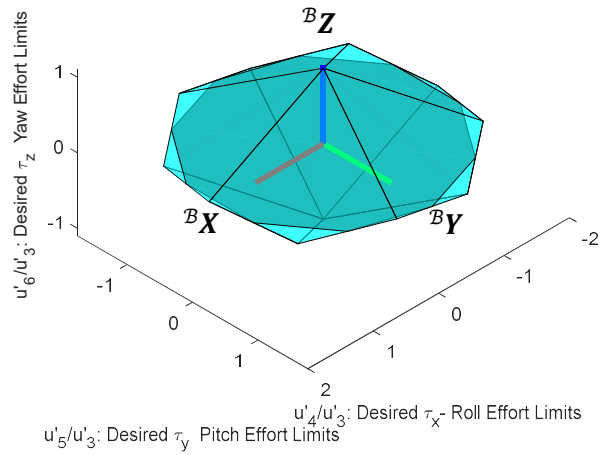


Figure 4.22. Isometric view of the decacopter attitude speed constraints.

The top view of the decacopter constraint space is shown in Figure 4.23.

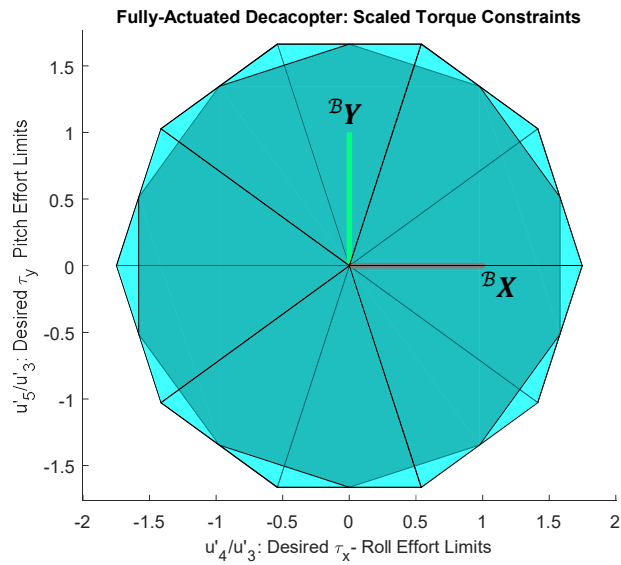


Figure 4.23. Top view of the decacopter attitude speed constraints.

The front and side views of the decacopter attitude constraint space are shown in Figure 4.24. Immediately, the shape disparities parallel those of the hexrotor. The front views of both platforms are of hexagonal shape, while the side views are square. This shape difference highlights the lack of rotor support in the generation of pitch. Two rotors lie on the ${}^B\mathbf{Y}$ axis such that four rotors contribute to pitch in the hexrotor design and 8 rotors contribute to pitch in the decacopter design. The in axis rotors induce similar reduction in restraint space for force generation.

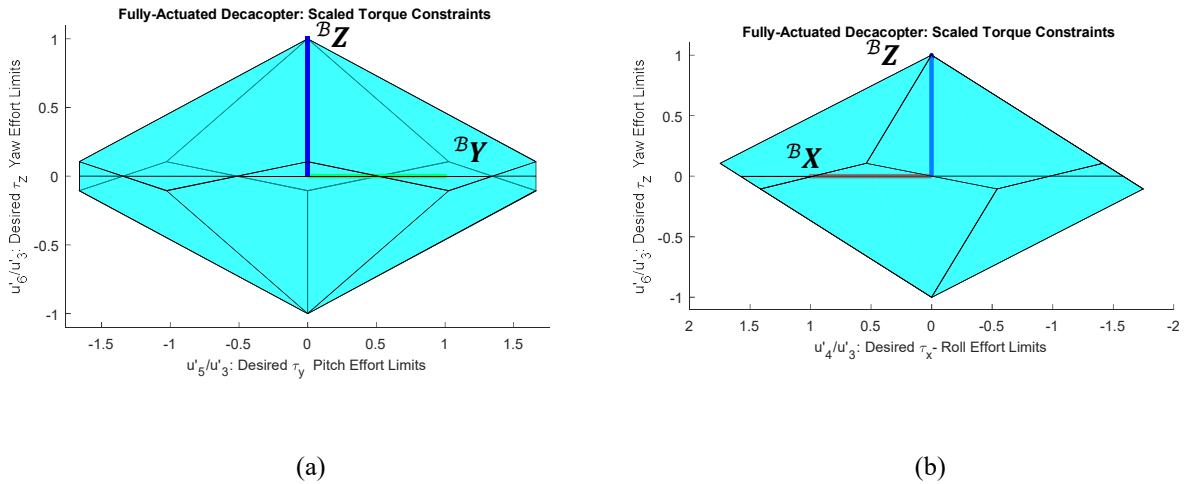


Figure 4.24. (a) Front view of the decacopter attitude speed constraints. (b) Side view of the decacopter attitude speed constraints.

It is posited that an n -rotor multirotor possesses an attitude constraint space developed as an n -faced 3-dimensional polygon, possessing rectangular faces. The n -rotor multirotor possesses an n -sided polygon constraint space for force development if $\text{mod}_4(n) = 0$, and an $\frac{n}{2}$ -sided polygon if $\text{mod}_4(n) \neq 0$. That is, the multirotor configuration can be bisected symmetrically about two orthogonal axes.

The constraints for a 12-sided multirotor were developed for rigor. This 12-rotor multirotor was called a duodecacopter, and since its configuration can be bisected by two orthogonal axes, its constraint spaces

were expected to mirror those of the octocopter. As shown in Figure 4.25 the expected 12-sided polygon resulted from the developed constraint definitions in Eq. (4.13) and Eq. (4.15).

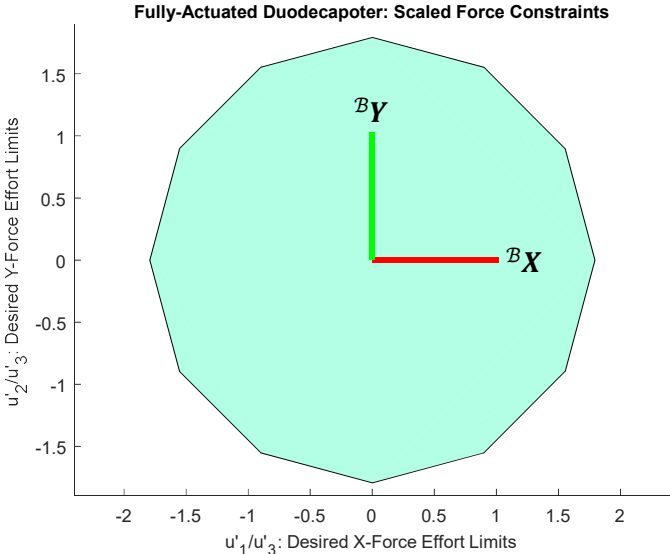


Figure 4.25. Projection of force constraints for a fully-actuated duodecapoter.

Using Eq. (4.14) The attitude constraint space was developed in Figure 4.26.

Fully-Actuated Duodecaopter: Scaled Torque Constraints

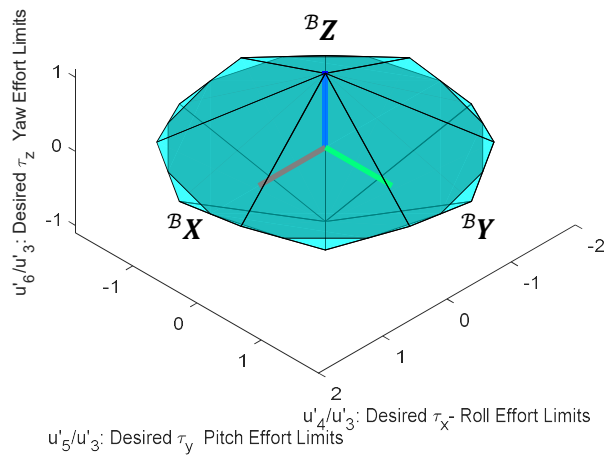


Figure 4.26. Isometric view of the duodecaopter attitude speed constraints.

The top view was presented in Figure 4.27.

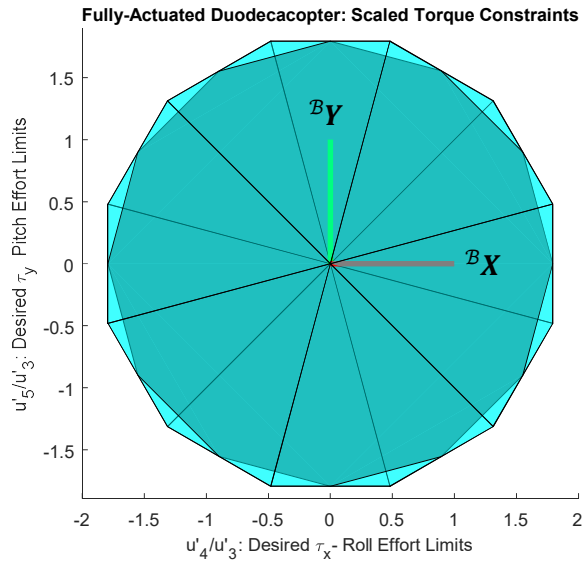


Figure 4.27. Top view of the duodecaopter attitude speed constraints.

Lastly, the front and side views were presented in Figure 4.28

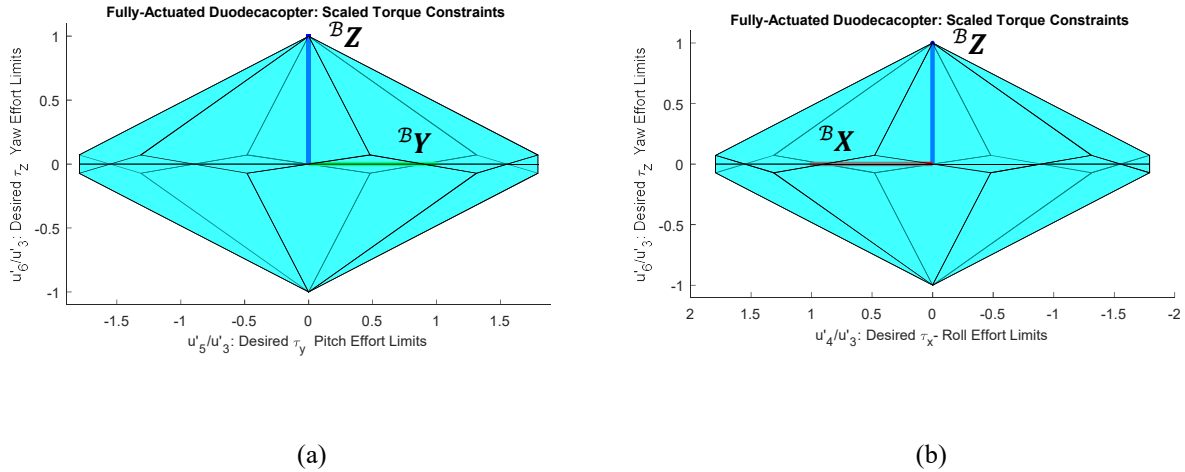


Figure 4.28. (a) Front view of the duodecacopter attitude speed constraints. (b) Side view of the duodecacopter attitude speed constraints.

As expected the force constraint plane was developed as a 12-sided polygon, and the attitude constraint space presented as a 12-sided 3-dimensional polygon with rectangular faces. As $n \rightarrow \infty$ the expected yaw symmetric shapes converge to a conical polygon with force and roll/pitch constraint planes of the circular shape inherent of L_2 -norm metrics. While this is impractical, this analysis demonstrates the necessity of the inspection of the constraint spaces of finite rotor multirotor design, and suggests multirotor with rotor number n satisfying $\text{mod}_4(n) = 0$ such as the octocopter are superior in aerial manipulation applications due to their higher order polygon shaped force constraint space.

4.3 Cross-span Compensation Design

While the major purpose of the introduced efficiency metrics in Eq. (4.5) and Eq. (4.7) was to develop design based considerations for nonparallel hexrotor performance relative to parallel hexrotor of similar

form factor, the development of compensation elements can also be developed. This responds to the converse question of what form factor compensation is necessary to correct any efficiency losses inherent to fully-actuated tilt design.

While there is no direct method for affecting throttle or yaw performance via compensation design of L , roll and pitch compensation is possible as they depend explicitly on cross-span in both designs configurations. To differentiate nonparallel and parallel cross span, L_i and L_j were introduced in the analysis, where L_i and L_j correspond to cross-span lengths for a nonparallel multirotor and parallel multirotor, respectively. The efficiency metrics corresponding to roll and pitch in Eq. (4.5) were rewritten in terms of the new cross-span definitions as

$$\begin{aligned}\epsilon_{\tau_x} &= \left(\mp 2q_1 \frac{d}{L_j b} s_\beta + \frac{L_i}{L_j} c_\beta \right)^2, \\ \epsilon_{\tau_y} &= \left(\mp 2q_1 \frac{d}{L_j b} s_\beta + \frac{L_i}{L_j} c_\beta \right)^2,\end{aligned}\tag{4.16}$$

The inclusion of distinct cross-span terms L_i and L_j provides a designer with a method for compensating efficiency losses in roll and pitch torque generation. Because throttle force and yaw torque are applied directly to the z-axis of the parallel model \mathcal{F}_j there is no method for compensation of efficiency in this formulation. While increasing the cross-span of a multirotor increases form factor and changes the overall usability of a multirotor, it should be noted that by increasing the cross-span of a nonparallel multirotor according to the relationship

$$L_i = \left| \frac{L_j}{c_\beta} \pm 2q_1 \frac{d}{b} t_\beta \right| \Rightarrow \epsilon_{\tau_x} = \epsilon_{\tau_y} = 1,\tag{4.17}$$

results a platform which possess identical control authority over the platform's roll and pitch axes as a parallel platform. Often it is impractical to identify the thrust and drag parameters b and d without force/torque testing, therefore an approximate model can be used of the form

$$L_i = \left| \frac{L_j}{c\beta} \right| \Rightarrow \left(1 - 2 \frac{d}{L_j b} \right)^2 \leq \epsilon_{\tau_x} = \epsilon_{\tau_x} = \left(1 \mp 2q_1 \frac{d}{L_j b} s\beta \right)^2 \leq \left(1 + 2 \frac{d}{L_j b} \right)^2. \quad (4.18)$$

While this design does not return unity power efficiency in roll and pitch production, it relies solely on the design tilt angle for calculation without prior knowledge of the rotors being used. This can provide an effective method for general nonparallel multirotor design. How well the approximate model matches the exact model depends on the ratio of drag to thrust production which is generally $\frac{d}{b} = O(10^{-2})m$ as thrust is often much larger than drag for a UAV rotor and the parallel comparator class cross-span L_j . A comparison chart for cross-span compensation for several common multirotor classes are given in Figure 4.29 as a function of design tilt β .

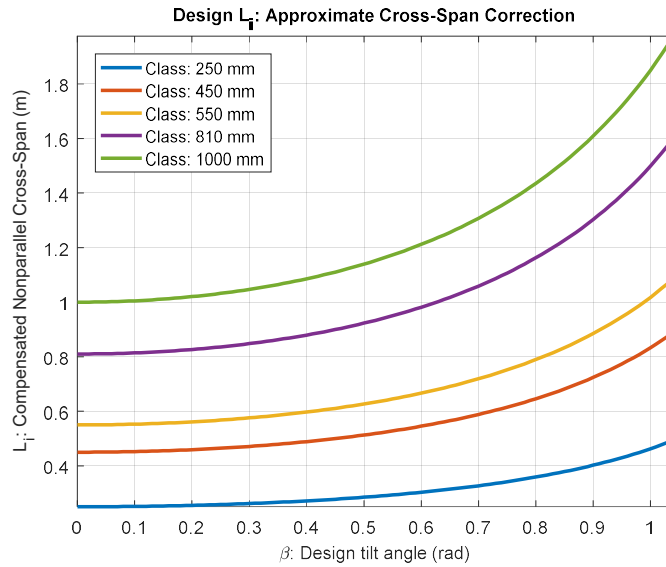


Figure 4.29. Approximate cross-span model compensation isoclines as a function of design tilt.

For small β compensation is feasible, however, larger rotor tilt requires larger compensation making it impractical.

5 Fully-Actuated UAV Control

Regardless of airframe type, control of multirotor UAV has been studied heavily in the literature, when it comes to underactuated platforms. Fully-actuated platforms, however, are a relatively new topic in the study of multirotor UAV, thus, special treatment of the control strategy employed in this study was considered. In this section fully-actuated control is developed using a backstepping scheme, overall stability is discussed concerning aerial manipulation, and the dynamics of an attached manipulator as well as some consequences on environment interaction are introduced. For a more rigorous treatment of the backstepping technique please refer to Appendix C.

5.1 Deterministic Control

Backstepping is a common method of nonlinear control which affects platform dynamics via a mixed control signal composed of both feedforward and feedback terms denoted in this analysis as $\Gamma_{u,f}$ and $\Gamma_{u,b}$, respectively. The control signal Γ_u was redefined here as

$$\begin{aligned}\Gamma_u &= \Gamma_{u,f} + \Gamma_{u,b}, \\ \Gamma_{u,f} &:= C(\mathcal{H}\xi)^{\mathcal{H}}\xi - \Gamma_g - \Gamma_o - \Gamma_w, \\ \Gamma_{u,b} &:= M\Lambda_d,\end{aligned}\tag{5.1}$$

where Λ_d are some desired stable error dynamics. In the deterministic approach, it is assumed that all parameters and nonlinear effects are known precisely This is a key assumption. The composition of this controller is such that a feedforward component $\Gamma_{u,f}$ effectively cancels the nonlinear centripetal-Coriolis term, and the effects of gravity, gyroscopic torque, and known disturbance, however, more robust methods may be employed to account for sensitivity to estimation error. The feedback term $\Gamma_{u,b}$ handles the error

dynamics of the system. The combination of these two terms provides a robust method for handling general nonlinearities.

It should be noted that multirotor UAV are classified as a nonlinear system of the form input-affine with drift for nonlinear mappings $f: \mathbb{R}^6 \rightarrow \mathbb{R}^6$ and $g: \mathbb{R}^6 \rightarrow \mathbb{R}^6$,

$$\mathcal{H}\dot{\xi} = f(\mathcal{H}\xi) + g(\mathcal{H}\xi)\mathbf{u}'. \quad (5.2)$$

The implications of drift in this formulation are such that, stability of $\mathcal{H}\xi$ may be impractical to prove globally. Physically, this is intuitive given a simple case study:

Let a multirotor be subject to a total attitude inversion, say ${}^B\theta = \pi$. Since thrust can be applied in the positive ${}^B\mathbf{Z}$ direction only, the UAV must right its orientation before producing vertical thrust capable of rejecting gravitational effects. Even if the controller is developed using backstepping and Lyapunov principles, practical application and saturation limits exclude global guarantees.

Regardless, backstepping was used throughout simulation and physical system testing, thus the theory was developed. In the following sections a 2nd order backstepping scheme was used to formulate stable error dynamics.

As the nonparallel multirotor class $\mathcal{F}_{\mathcal{S}_1}$ has been the subject of this study, the class is used to define body fixed control force and torque signals

$${}^B\mathbf{F} = \sum_{\mathcal{S}_1=\{1\}}^{\{n\}} {}^B\mathbf{F}_{\mathcal{S}_1}, \quad (5.3)$$

$${}^B\boldsymbol{\tau} = \sum_{\mathcal{S}_1=\{1\}}^{\{n\}} {}^B\boldsymbol{\tau}_{\mathcal{S}_1}.$$

The mappings $f_1: \mathbb{R}^6 \rightarrow \mathbb{R}^6$, $f_2: \mathbb{R}^6 \rightarrow \mathbb{R}^6$, $g_1: \mathbb{R}^6 \rightarrow \mathbb{R}^6$, and $g_2: \mathbb{R}^6 \rightarrow \mathbb{R}^6$ are defined and used to format the dynamic equations from Eq. (2.32) in

$$\begin{aligned}\varepsilon \dot{\mathbf{V}}_B &= f_1 + g_1(\varepsilon \boldsymbol{\Theta}_B)^B \mathbf{F}, \\ f_1 &:= m^{*-1}(\mathbf{F}_g + \mathbf{F}_w),\end{aligned}\tag{5.4}$$

$$g_1(\varepsilon \boldsymbol{\Theta}_B) := m^{*-1} R_\Theta,$$

and

$$\begin{aligned}{}^B \dot{\boldsymbol{\omega}} &= f_2(\varepsilon \boldsymbol{\Theta}_B, {}^B \boldsymbol{\omega}) + g_2 {}^B \boldsymbol{\tau}. \\ f_2(\varepsilon \boldsymbol{\Theta}_B, {}^B \boldsymbol{\omega}) &:= {}^B J^{*-1} \left(S({}^B J^* {}^B \boldsymbol{\omega})^B \boldsymbol{\omega} + {}^B \mathbf{P}_c \times R_\Theta^T \mathbf{F}_g - \sum_{\tilde{s}_1=\{1\}}^{\{n\}} J_r({}^B \boldsymbol{\omega} \times {}^B R_{\tilde{s}_1} {}^{\tilde{s}_1} \boldsymbol{\Omega}) + \right. \\ &\quad \left. \boldsymbol{\tau}_w \right), \\ g_2 &:= {}^B J^{*-1}.\end{aligned}\tag{5.5}$$

The deterministic control laws can then be formulated for both force and torque systems as

$$\begin{aligned}{}^B \mathbf{F}^* &= g_1^{-1}(\varepsilon \boldsymbol{\Theta}_B)(-f_1 + \boldsymbol{\Lambda}_{u,1}), \\ {}^B \boldsymbol{\tau}^* &= g_2^{-1}(-f_2(\varepsilon \boldsymbol{\Theta}_B, {}^B \boldsymbol{\omega}) + \boldsymbol{\Lambda}_{u,2}),\end{aligned}\tag{5.6}$$

where $\boldsymbol{\Lambda}_{u,1}$ and $\boldsymbol{\Lambda}_{u,2}$ represent some stable error dynamics formulated after the second order backstepping scheme derived in Appendix C,

$$\begin{aligned}\boldsymbol{\Lambda}_{u,1} &:= \varepsilon \dot{\mathbf{V}}_{B_d} + (D_{11} + D_{12}) \varepsilon \tilde{\mathbf{V}}_B + (I + D_{12} D_{11}) \varepsilon \tilde{\mathbf{P}}_B, \\ \boldsymbol{\Lambda}_{u,2} &:= {}^B \dot{\boldsymbol{\omega}}_d + (D_{21} + D_{22}) {}^B \tilde{\boldsymbol{\omega}} + (I + D_{22} D_{21}) \int_0^t {}^B \tilde{\boldsymbol{\omega}} dt.\end{aligned}\tag{5.7}$$

Substituting these definitions into the deterministic control law results

$$\begin{aligned}
{}^B\mathbf{F}^* &= g_1^{-1}(\varepsilon\boldsymbol{\Theta}_B)(-f_1 + \varepsilon\dot{\mathbf{V}}_{B_d} + (D_{11} + D_{12})\varepsilon\tilde{\mathbf{V}}_B + (I + D_{12}D_{11})\varepsilon\tilde{\mathbf{P}}_B), \\
{}^B\boldsymbol{\tau}^* &= g_2^{-1}\left(-f_2(\varepsilon\boldsymbol{\Theta}_B, {}^B\boldsymbol{\omega}) + {}^B\dot{\boldsymbol{\omega}}_d + (D_{21} + D_{22}){}^B\tilde{\boldsymbol{\omega}} + (I + D_{22}D_{21})\int_0^t {}^B\tilde{\boldsymbol{\omega}} dt\right).
\end{aligned} \tag{5.8}$$

The feasibility of this controller depends on several factors. Of note, the accuracy of measurement of the state variables, the disturbance vector quantities \mathbf{F}_w and $\boldsymbol{\tau}_w$, and the state dependent scaling produced by the inverse mapping of $g_1(\varepsilon\boldsymbol{\Theta}_B)$. Concerning the nonlinear mappings $f_1, f_2(\varepsilon\boldsymbol{\Theta}_B, {}^B\boldsymbol{\omega})$, $g_1(\varepsilon\boldsymbol{\Theta}_B)$, and g_2 , the global attitude $\varepsilon\boldsymbol{\Theta}_B$ and angular velocity ${}^B\boldsymbol{\omega}$ can be estimated with relative accuracy using the accelerometer, gyroscope, and magnetometer sensors native to flight controllers such as the Pixhawk, NAZA, APM, etc. The velocity $\varepsilon\mathbf{V}_B$ may be estimated with IMU, GPS, and barometer sensors, however, careful consideration must be taken to develop an accurate estimate of global position $\varepsilon\mathbf{P}_B$. Unlike the internal IMU, GPS and barometer measurements are not accurate. Further complications arise from GPS denied environments. In the indoor experiments performed in this work, motion capture feedback is readily available, thus, it is assumed that $\varepsilon\mathbf{P}_B$ can be developed with satisfactory accuracy. The inverse of $g_1(\varepsilon\boldsymbol{\Theta}_B)$ and g_2 are always calculable, however, the transpose rotation matrix R_Θ^T that appears in the formulation of $g_1(\varepsilon\boldsymbol{\Theta}_B)$ requires careful consideration as throttle requirements will vary greatly depending on UAV orientation.

As passive systems, UAV are generally simple to control given reasonable references, however, saturation must be carefully considered due to contributions from the disturbance vector. Wind effects aside, aerial manipulators are heavily affected by manipulator dynamics, thus, estimation of these effects is necessary. One advantage of the fully-actuated design is that general decoupling of both UAV and manipulator systems is possible. In the next section manipulator dynamics are developed.

5.2 The Disturbance Vector and Manipulator Dynamics

The disturbance vector introduced in Eq. (2.24) was expressed in terms of the variables \mathbf{F}_w and $\boldsymbol{\tau}_w$, respectively. In this study the dominating contributor to disturbance is the wrench produced by an attached manipulator. The effects were modeled using the iterative Newton-Euler algorithm such that force and torque at the base of the manipulator may be estimated in terms of some external wrench, applied to the UAV body fixed frame \mathcal{B} , and factored into the backstepping flight controller.

Following the iterative Newton-Euler formulism outlined in Appendix B, a Denavit-Hartenberg parameter table was constructed in Table 5.1, where d_1 was used to denote a z-offset for the manipulator in m , a_3 , a_4 , and a_5 are the effective link lengths of the manipulator, and $\theta_1(t)$, $\theta_2(t)$, $\theta_3(t)$, $\theta_4(t)$, and $\theta_5(t)$ correspond to joint angles of the manipulator servo actuators.

Table 5.1. Denavit-Hartenberg parameters for the custom aerial manipulator

i	α_{i-1}	a_{i-1}	θ_i	d_i
1	π	0	0	d_1
2	0	0	$\theta_2(t)$	0
3	$\frac{\pi}{2}$	0	$\theta_3(t)$	0
4	0	a_3	$\theta_4(t)$	0
5	0	a_4	$\theta_5(t)$	0
6	0	a_5	0	0

By completing the outward and inward iterations defined in Eq. (B.3.4) to Eq. (B.3.8) of the algorithm, the base force ${}^0\mathbf{f}$ and torque ${}^0\boldsymbol{\tau}$ can be directly applied to the UAV body fixed frame in calculation. Similarly, any external environment interaction are quickly factored into this calculation by the inclusion of ${}^7\mathbf{f}$ and

⁷ τ . Since these effects are measured with respect to the tool frame, external forces and torques due to interactions can be applied to the base via this tool frame definition.

An additional consideration taken in design was that of workspace restrictions. In general, dynamics cannot be used to inform workspace restrictions, however, static considerations can be made. In Figure 5.1 a generic manipulator is shown with several workspace regions outlined. As a static system, the blue region for this manipulator corresponds to the possible positions of the tool frame where an unknown mass may be held. The green contours correspond to a composite COG which can be calculated statically for all configurations. This region will deform based on the total weight of the manipulator system and can be used in defining roll/pitch torque projection limits.

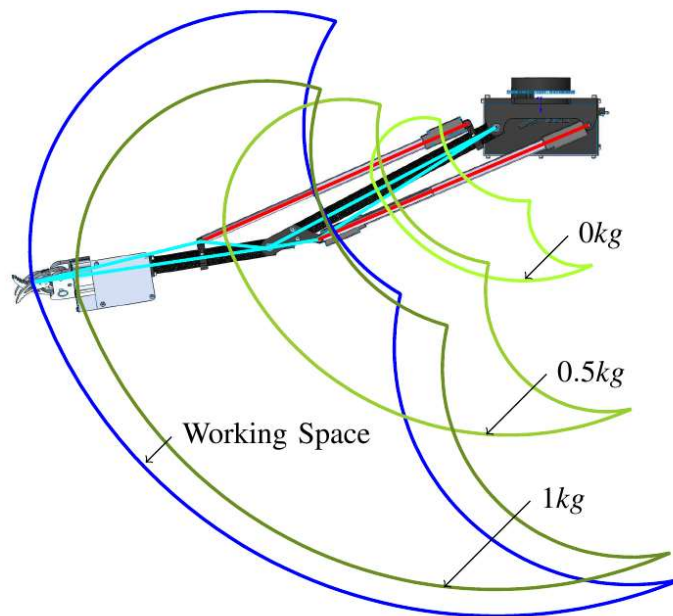


Figure 5.1. Example manipulator workspace and expected position of CG with varying payloads.

Once a manipulator is attached to an airframe, static hover must provide reasonable saturation limits corresponding to the geometry defined in the previous sections concerning torque generated by static location of the composite CG denoted $\sum m_i$ and defined in Figure 5.2.

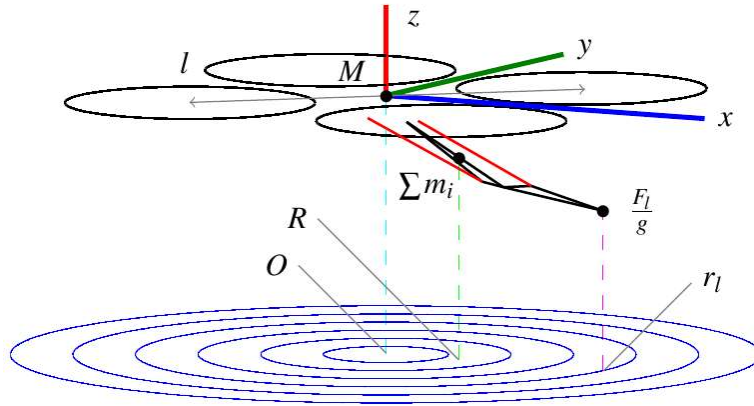


Figure 5.2. Static hover considerations for manipulator configurations.

While the manipulator controller is not the focus of this work, the control diagram shown in Figure 5.3 demonstrates one possible configuration for a fully-actuated aerial manipulation setup. In this setup, body-fixed accelerations and velocities are passed to the manipulator model for the development of joint torques, while the base force and torques are used in the multirotor model to develop rotor speed commands towards stable flight. A pseudo-real-time control architecture such as the Robot Operating System (ROS) can be used to develop reference control signals for closed-loop control. Details on this type of setup are provided in the following sections.

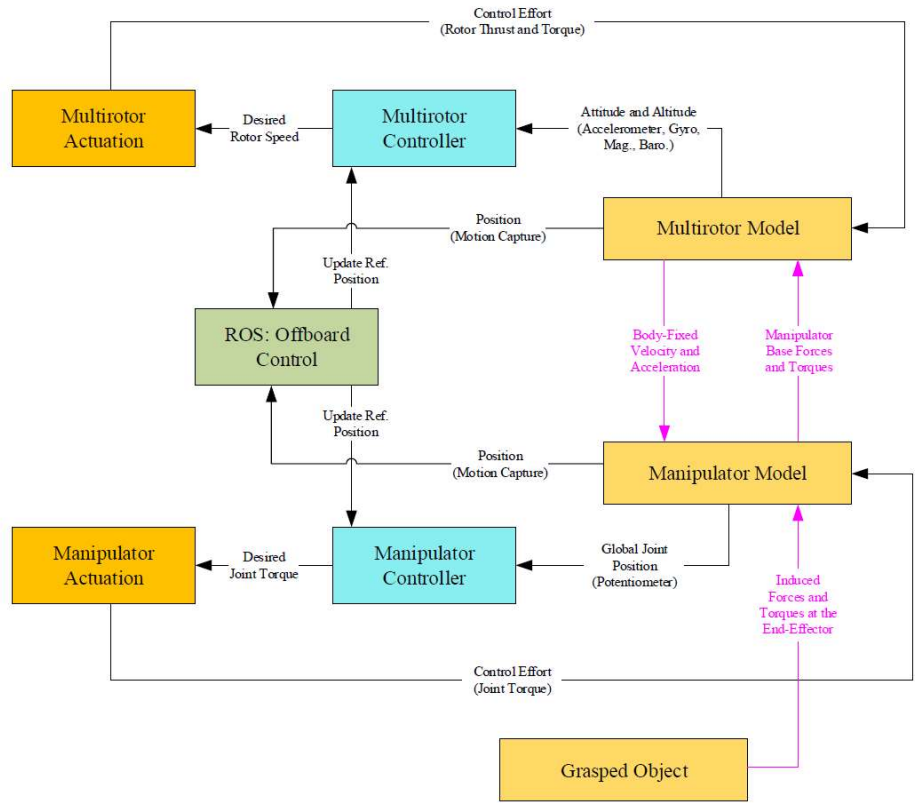


Figure 5.3. Decoupled control diagram for an aerial manipulator.

6 Prototype Development and Experimentation

In this section, prototype development and experimental verification performed for this work are described. For all flight experiments, the caged flight volumes shown in Figure 6.1 and Figure 6.2 were used. In the indoor flight volume setup of Figure 6.1, an Optitrack motion capture system was used to provide precise position and orientation measurements for use in closed-loop control. Pose data of a rigid body can be reported at 120 Hz via the ROS framework. For those applications requiring GPS feedback, the outdoor flight volume was used. Both flight volumes were maintained in the University of Nevada, Las Vegas Intelligent Structures and Control Laboratory located in Las Vegas, Nevada.

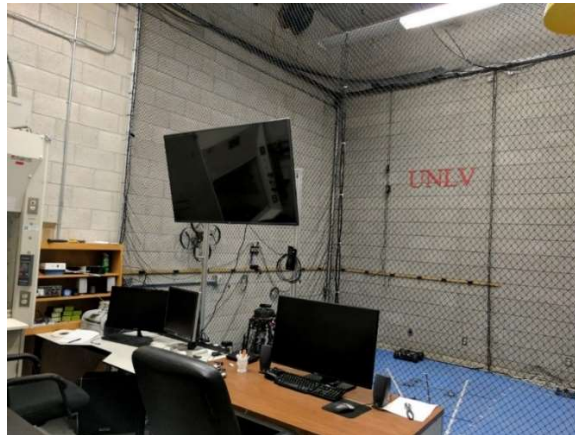


Figure 6.1. UNLV indoor flight volume equipped with an Optitrack motion capture system.



Figure 6.2. UNLV outdoor flight volume used for flight experiments requiring GPS localization.

6.1 Physical System Design

The aerial manipulation hardware for the developed prototype was introduced in this section. The completed airframe is shown in Figure 6.3. The airframe was based on the Flamewheel 550 kit, where custom motor mounts were printed from PLA on a TAZ 5 3D printer. The custom motor mounts increased total cross span of the airframe from 0.550 m to $L = 0.7024\text{ m}$. The entire airframe, excluding attached battery possessed a mass of 2.057 kg . The interchangeable battery was typically chosen to be a Turnigy 8000 mAh 6S (nominal: 22.2V) LiPo battery weighing 1.131 kg . For general operation and analysis considerations, the effective mass of this platform was taken to be $m^* = 3.188\text{ kg}$.



Figure 6.3. Completed fully-actuated hexrotor prototype

The rotor and propeller pairing chosen for the prototype build was the T-Motors MN4006 Antigravity brushless motor along with Timber T-Style Propeller 13x4.4 propellers. Each propeller rotor pairing was mounted to a custom motor mount designed with a fixed tilt of $\beta = \frac{\pi}{6}$ as shown in Figure 6.4. Of the four possible fully-actuated designs developed in Figure 3.2, configuration (a), where $\alpha = \alpha_1 = \frac{\pi}{2}$ and $q_1 = -1$ was chosen for this build.

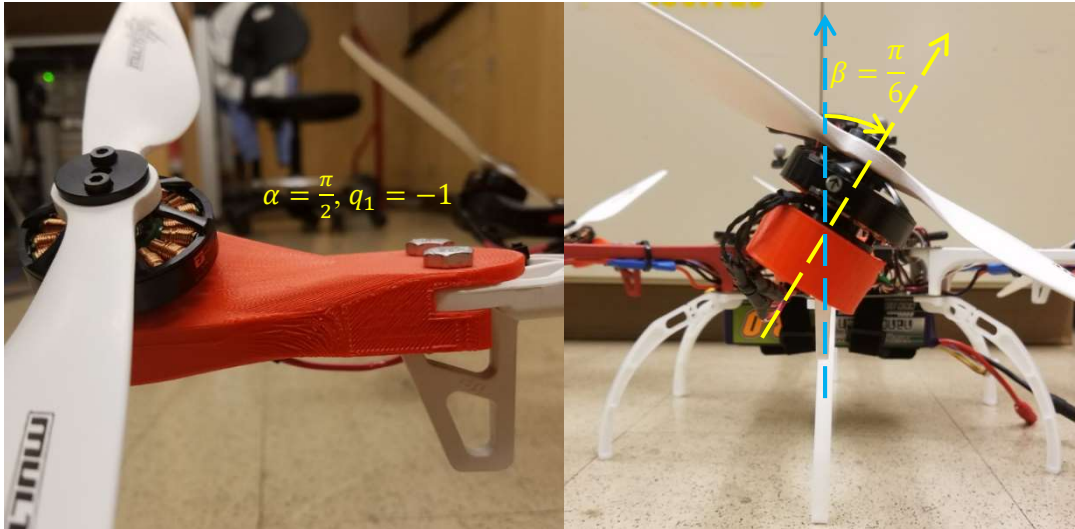


Figure 6.4. Custom motor mounts built with a design tilt of $\beta = \frac{\pi}{6}$.

The manipulator system was composed of 5 AX-12+ Dynamixel servo motors. These motors are conveniently ROS enabled and readily provide, position, velocity, and current draw data. As shown in Figure 6.5, the manipulator was attached to the power distribution board on the bottom of the hexrotor airframe. The manipulator system weighs in at 0.621 kg .

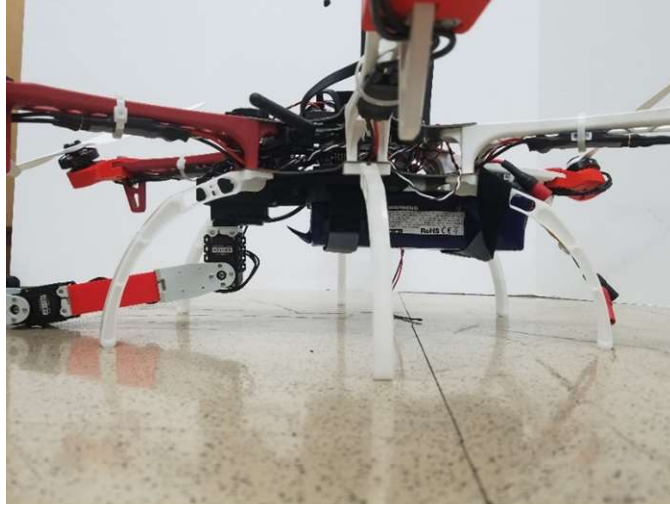


Figure 6.5. Manipulator mounting configuration.

The battery and manipulator mounting configuration are shown isolated from the main system in Figure 6.6 and Figure 6.7. As shown, the battery mounting point was shifted backwards to accommodate the manipulator. This design choice served two purposes. First, the manipulator is placed closer to its expected tool frame target, and second, it allows for a more compact and balanced mass distribution in expected manipulator use-cases.

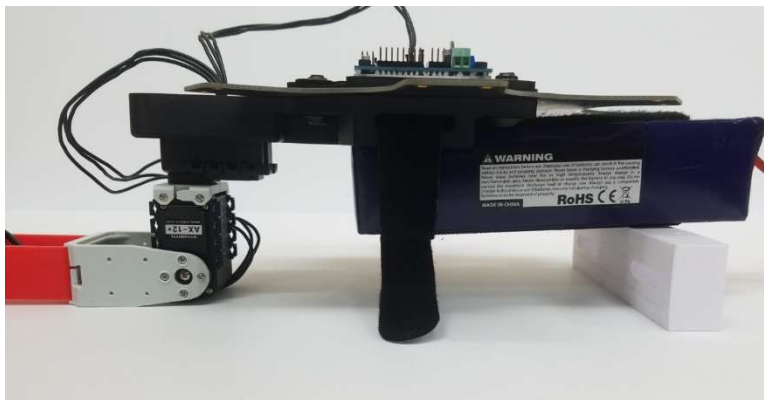


Figure 6.6. Side view of manipulator and lower mounting hardware.

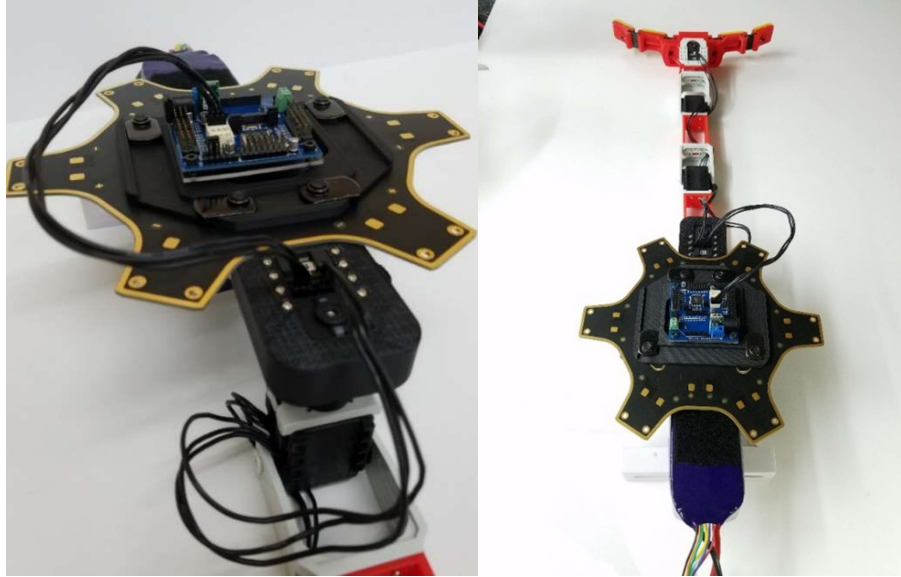


Figure 6.7. Real-time servo controller Arbotix-M, and the mounting and power distribution board.

In the next section, specific hardware used in the power train, and control and communications hardware are introduced.

6.2 Flight Hardware

To generate thrust and drag via the propeller rotor pairing, X-Rotor 40A electronic speed controllers (ESC) were used to convert servo signals sent by a flight controller directly to the motor in affect brushless motor torque. Since the multirotor battery is connected directly to the ESCs any voltage drops in the battery directly affect rotor torque output. The flight controller used with the developed prototype was the Pixhawk 2.1 flight controller flashed with a custom APM flight stack. The Pixhawk 2.1 possesses a breakout board and redundant internal IMU. Thus, the flight controller is capable of measuring acceleration, and angular velocity changes due to airframe motion and develop control signals as a real-time system. The HERE GPS and compass unit was mounted to the IR marker stand as shown in Figure 6.8. To affect reference control, an Odroid XU4 was mounted to the platform, and communications between the onboard linux computer and the flight controller were performed via the MAVLINK protocol [44].



Figure 6.8. Top view of the fully-actuated hexrotor. Peripheral and controller hardware shown.

6.3 Simulation Testing

In this section, several different simulations of UAV flight and aerial manipulation were performed using the Matlab toolboxes Simulink and Simscape Multibody [45] and V-Rep developed by Coppelia Robotics [46]. The purpose of these simulations was to validate dynamic performance of the airframe, and evaluate expected behavior under custom control strategies.

6.3.1 Simulated Hexrotor Flight and Arbitrary Wrench Production

The first simulation was built using Simscape Multibody and modeled fully-actuated flight of the hexrotor and mounted manipulator. The workspace shown in Figure 6.9 provides a general description of the simulation build. The UAV is attached to the inertial frame block via a 6 DOF joint, and the manipulator is attached to the body-fixed frame of the airframe.

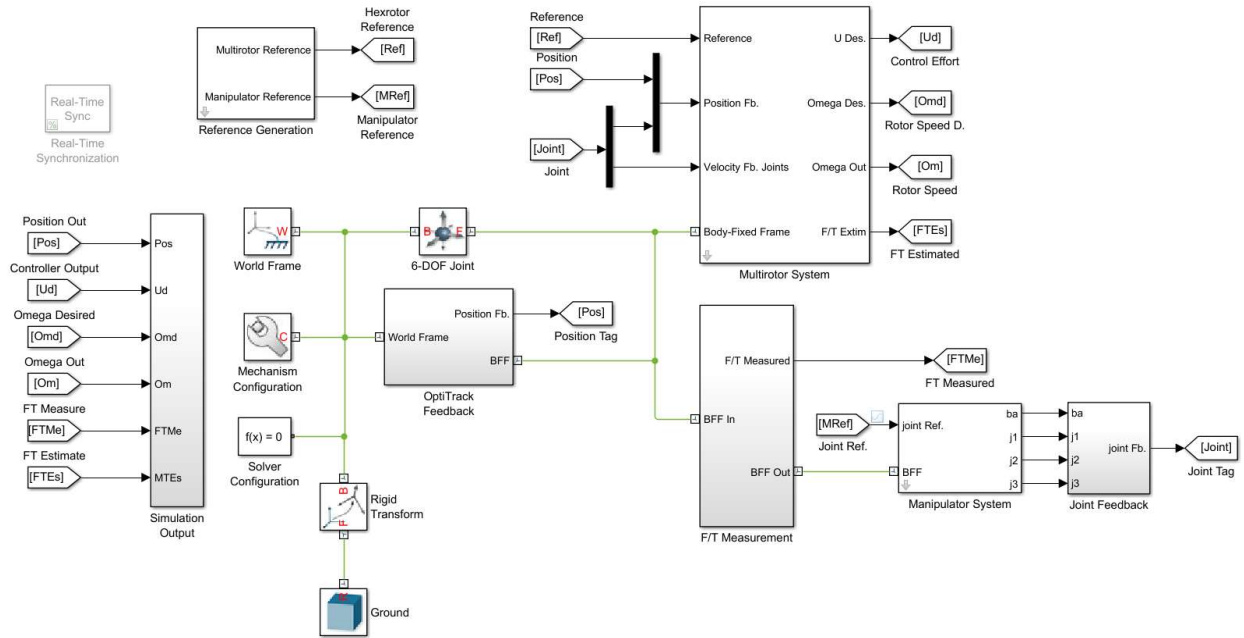


Figure 6.9. Completed aerial manipulator simulation in the Simulink environment.

Because of the build structure, the manipulator and UAV systems may be analyzed together or independently via targeted subsystem analysis. The UAV subsystem build is shown in Figure 6.10. As depicted, the UAV internal controller receives external references and position feedback, say from a motion capture system. There is also in input option for manipulator joint velocity information for iterative Newton-Euler estimation of manipulator forces and torques. Internal IMU may report some velocity feedback as well, hence the muxing of these signals with manipulator joint feedback. The estimated manipulator force and torque is reported for reference considerations, and a desired control signal $\mathbf{F}_{u,d}$ is sent to the rotors speed interpreter. The interpreter allocates rotor differentials based on the mapping

$$\boldsymbol{\omega} = \mathbf{h}_m(t) * \boldsymbol{\omega}_d, \quad (6.1)$$

$$\boldsymbol{\omega}_d = \mathbf{A}^{-1}(\boldsymbol{\alpha}, \boldsymbol{\beta}, \mathbf{q}) \mathbf{F}_{u,d}.$$

In this mapping, a desired rotor speed control vector ω_d is generated and sent through a first order linear motor model. This motor model transformation was used to represent the response of a brushless motor and denoted in the mapping as the convolution of the motor impulse response $h_m(t)$ and ω_d . Because the prototype is fully actuated, $A(\alpha, \beta, q)$ is invertible, and a unique mapping exists. A secondary subsystem is used to allocate gyroscopic torque as a function of rotor speed and body-fixed angular velocity ${}^B\omega$.

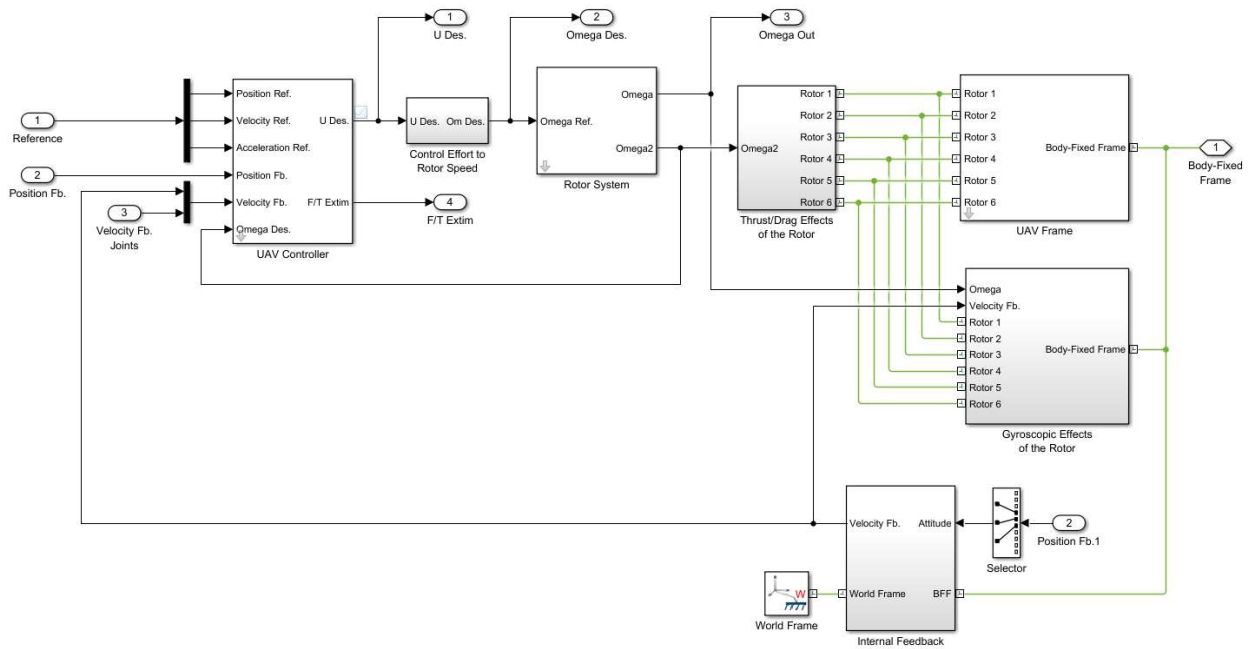


Figure 6.10. UAV dynamic and controller simulation subsystem.

A visualization of this simulation is provided in Figure 6.11.

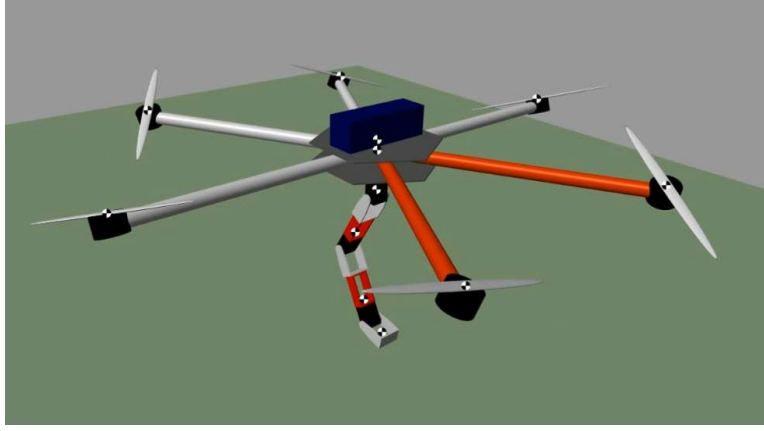


Figure 6.11. Primitive visualization of the fully-actuated hexrotor aerial manipulation platform in the Simscape Multibody environment.

In the presented case study, the feasibility of the arbitrary wrench production was evaluated. To test the hexrotor's performance, an arbitrary desired pose reference was commanded of the UAV model. The UAV state was given the following 4th order time dependent piecewise command:

$$\xi_d(t) = \begin{cases} a_4 t^4 + a_3 t^3 + a_2 t^2 + a_1 t + a_0 & 0 \leq t < \eta T \\ b_1 t + b_0 & \eta T \leq t < (1 - \eta) T \\ c_4 t^4 + c_3 t^3 + c_2 t^2 + c_1 t + c_0 & (1 - \eta) T \leq t < T \\ x_f & T \leq t \leq t_f \end{cases} \quad (6.2)$$

for the quartic-linear-quartic path described by the coefficients a_i , b_i , and c_i described in Table 6.1. These coefficients ensure that the reference signal issued to the model was piecewise continuous concerning position, velocity, and acceleration references. This was achieved by satisfying $\forall t, \lim_{\delta \rightarrow 0} \frac{d^n \xi_d(t \pm \delta)}{dt^n} = \frac{d^n \xi_d(t)}{dt^n}$ for $n = \{0,1,2\}$ and the boundary conditions $\xi_d(0) = \xi_{d,0}$, $\xi_d(t_f) = \xi_{d,f}$, and $\frac{d^m \xi_d(0)}{dt^m} = \frac{d^m \xi_d(t_f)}{dt^m} = 0$ for $m = \{1,2\}$.

Table 6.1. Coefficient table for continuous time fully-actuated hexrotor reference generation.

i	a_i	b_i	c_i
0	$\xi_{d,0}$	$\frac{(\eta - 2)\xi_{d,0} + \eta\xi_{d,f}}{2(\eta - 1)}$	$-\frac{(1 - 2\eta)\xi_{d,0} + ((2\eta - 1) + 2(\eta - 1)\eta^3)\xi_{d,f}}{2\eta^3(-\eta + 1)}$
1	0	$-\frac{\xi_{d,f} - \xi_{d,0}}{T(\eta - 1)}$	$\frac{(3\eta - 2)(\xi_{d,f} - \xi_{d,0})}{T\eta^3(-\eta + 1)}$
2	0		$\frac{3(\xi_{d,f} - \xi_{d,0})}{T^2\eta^3}$
3	$-\frac{\xi_{d,f} - \xi_{d,0}}{T^3\eta^2(\eta - 1)}$		$-\frac{(\eta - 2)(\xi_{d,f} - \xi_{d,0})}{T^3\eta^3(\eta - 1)}$
4	$\frac{\xi_d(t_f) - \xi_{d,0}}{2T^4\eta^3(\eta - 1)}$		$-\frac{\xi_{d,f} - \xi_{d,0}}{2T^4\eta^3(\eta - 1)}$

When given the reference data

$$\xi_d(0) = [0 \ 0 \ 0 \ 0 \ 0 \ 0]^T,$$

$$\xi_d(t_f) = [0.25 \ 0.5 \ 1 \ 0.1 \ 0.05 \ 0.7]^T,$$

(6.3)

$$\eta = 0.5,$$

$$T = 3,$$

the simulation pose data followed the trajectories of Figure 6.12, where the hexrotor was simulated at the prototype weight of $m^* = 3.188 \text{ kg}$, and a cross span of $L = 0.7024 \text{ m}$. A design tilt of $\beta = \frac{\pi}{6}$ was used as this was the chosen prototype design tilt.

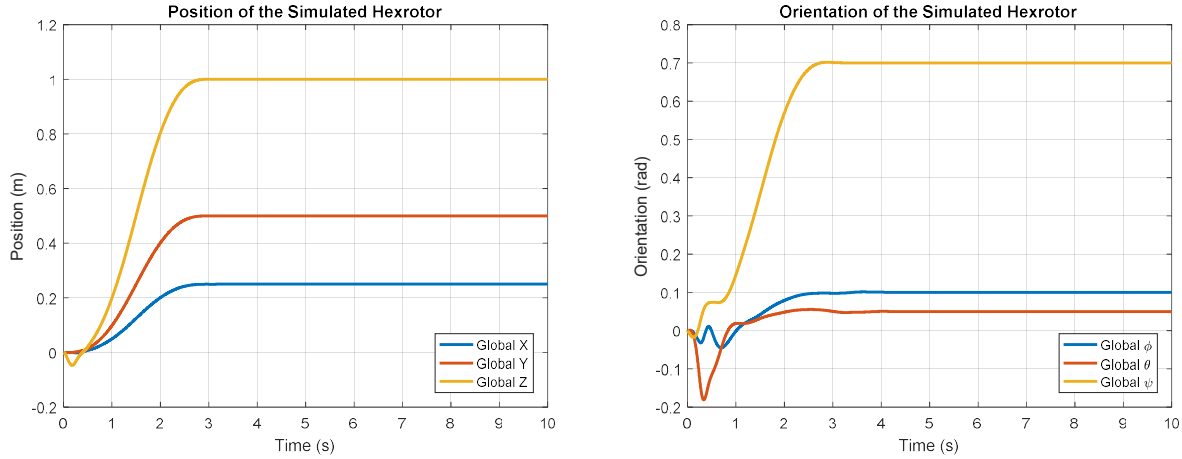


Figure 6.12. Simulated position and attitude of the fully-actuated hexrotor with no manipulator.

As demonstrated, the platform followed a non-zero roll/pitch trajectory in position hold. The simulation infers the capability for the real prototype to affect arbitrary pose tracking within some reasonable saturation limits. The rotor speed outputs for the simulation were provided in Figure 6.13. As discussed, the rotor speeds were determined via 1st order model of the form $H_{motor}(s) = \frac{1}{\tau s + 1} \omega_d(s)$, and saturated between $0 < \omega_i < \omega_{max}$, where ω_{max} was determined to be $750 \frac{rad}{s}$. All rotor performance data were determined experimentally. The details are explained in the experimental verification section of this paper including determination of the thrust and drag coefficients b and d .

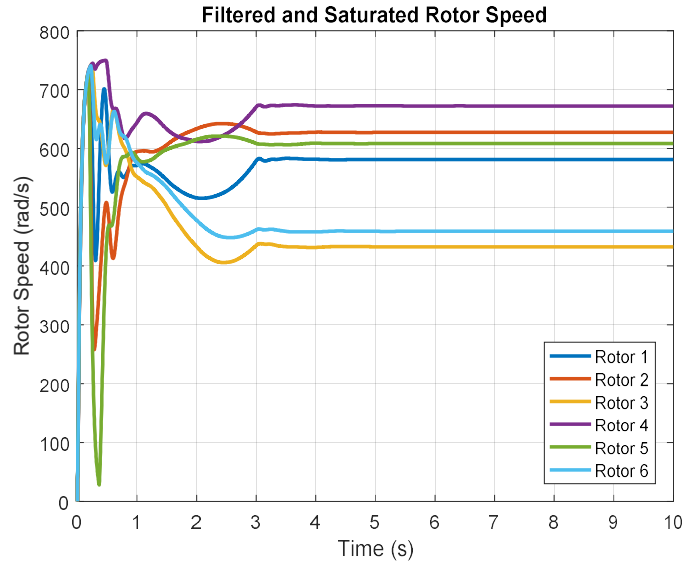


Figure 6.13. Simulation filtered and saturated rotor effort.

After steady state is attained, the rotor differentials are shown to be nonuniform across rotor definitions. This is due to the non-zero roll/pitch reference. It is clear from this assessment that the magnitude of desired roll/pitch orientation greatly affects saturation limits of the rotors. The resulting wrench data was provided in Figure 6.14 for this test. The steady-state wrench data shows the capability for this system to produce fixed and arbitrary forward and lateral forces along with the traditional throttle, roll, pitch, and yaw efforts associated with parallel multirotor.

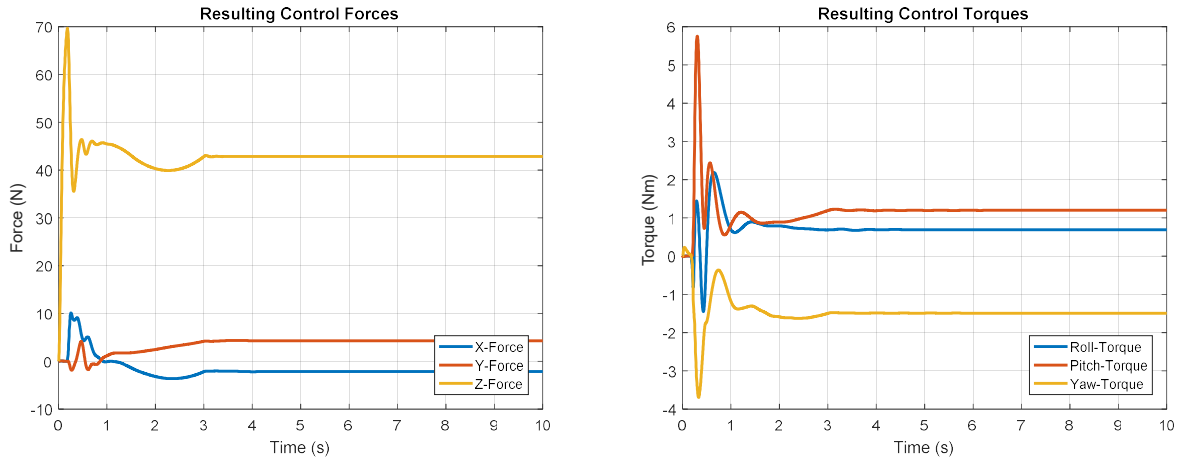


Figure 6.14. Control effort of the simulated hexrotor.

6.3.2 Manipulation and Wrench Estimates Using the Iterative Newton-Euler Algorithm

The second simulation build highlighted disturbance estimator of manipulator base reactions. The form of the simulated manipulator was matched explicitly to the prototype model as a 3R manipulator and attached to the base of the airframe as shown in Figure 6.15.

The goal of this case study as to assess the effectiveness of the iterative Newton-Euler algorithm towards calculation of reaction forces and torques applied to the base of the UAV. To that end a coupled simulation in which the manipulator was mounted to the hexrotor was performed, and the Simscape Multibody reaction forces and torques at the base of the manipulator were recorded in Figure 6.16. These results were calculated based on the physics solver native to Simscape Multibody.

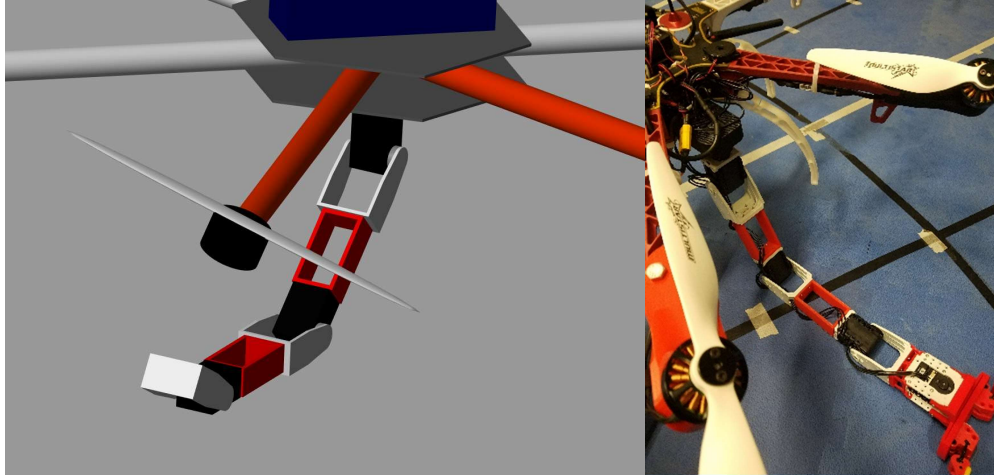


Figure 6.15. Primitive visualization of the manipulator system using Simscape Multibody, and the final prototype manipulator system.

For the case study presented in this study, the PID controlled servos were given a joint state reference $\theta_j = [\theta_2 \ \theta_3 \ \theta_4 \ \theta_5]^T = \left[-\frac{\pi}{4} \ \frac{\pi}{4} \ \frac{\pi}{4} \ \frac{\pi}{6}\right]^T$. The kinematics and control of the manipulator are irrelevant to the focus of this work, thus, full description of the manipulator actuation process was omitted. Rather, the manipulator is considered to be some system imparting reaction forces and torques, were these reactions can be measured with relative accuracy utilizing the Simscape Multibody physics solver.

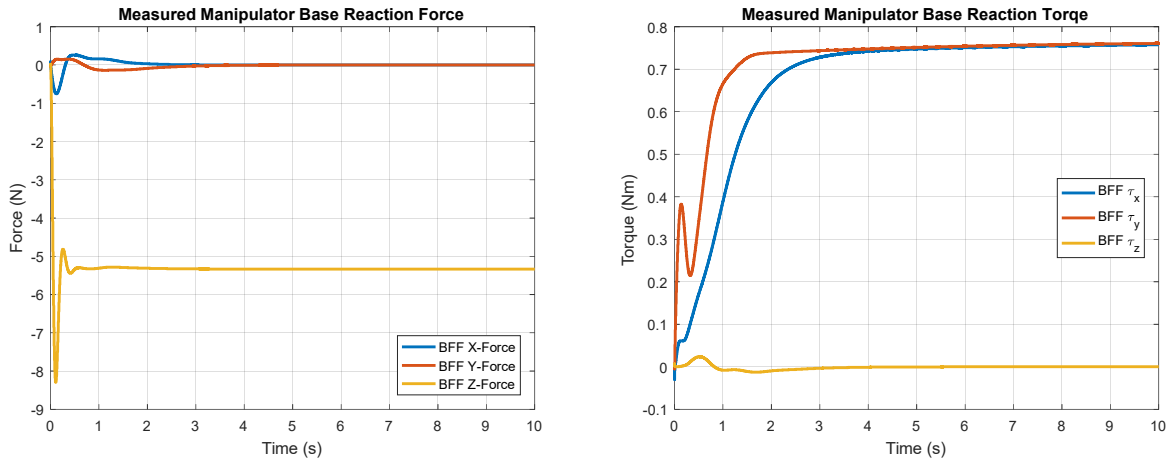


Figure 6.16. Simscape Multibody base reaction forces and torques developed from the physical simulation of the aerial manipulator.

The developed iterative Newton-Euler algorithm assumes point mass bodies for the calculation of reaction forces and torques. Figure 6.17 shows the developed estimate.

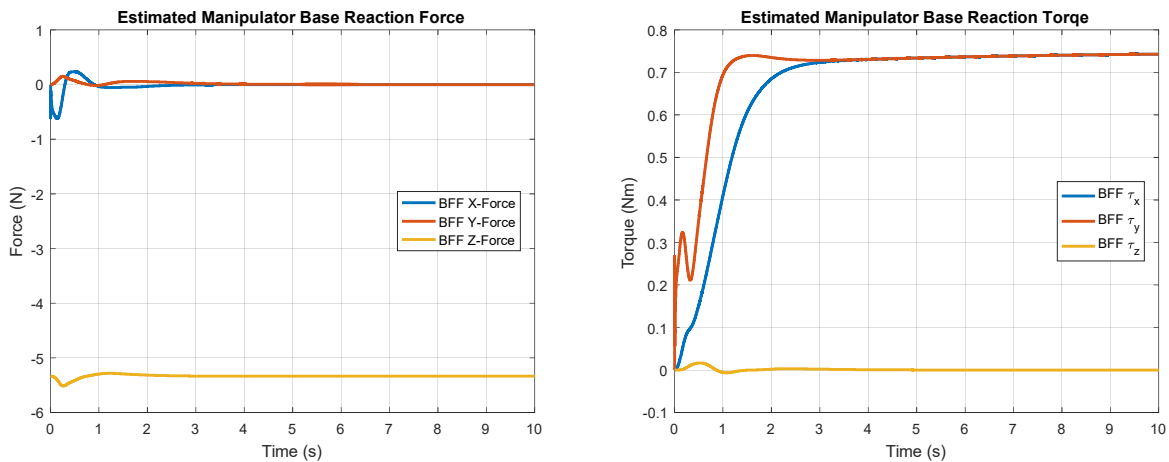


Figure 6.17. Iterative Newton-Euler algorithm estimation of base reactions.

As shown in the error estimates developed in Figure 6.18, the algorithm provides good steady state estimates with practical transient estimates. The large spike in z-force estimation error can be attributed to

the sensor used in force measurement. Since the simulation started at a discontinuity in applied force due to gravity. The estimator could not account for the numerical artifact.

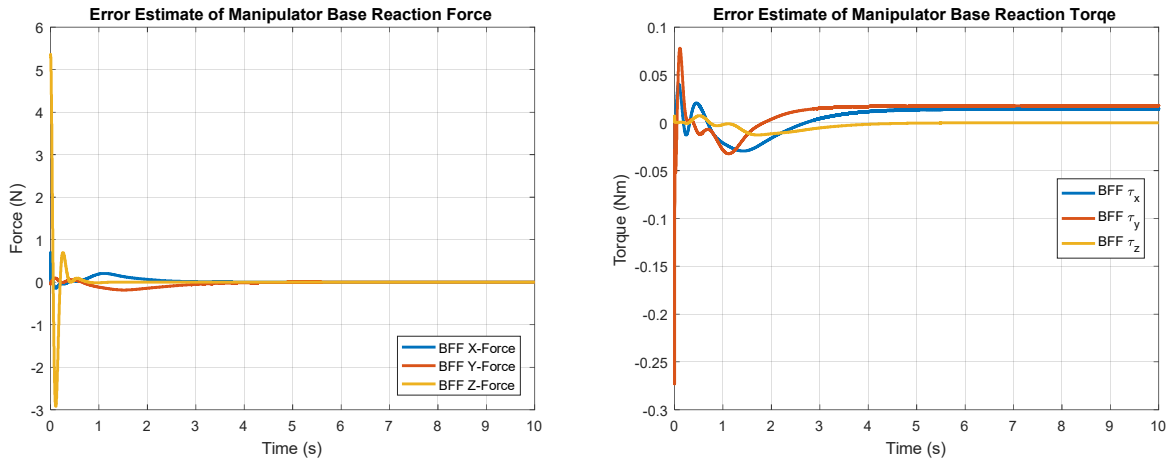


Figure 6.18. Error of the iterative Newton-Euler algorithm estimate.

6.3.3 Discrete Controller Tests using V-Rep and Application based Studies

The physics solvers native to the Mathworks toolboxes Simulink and Simscape Multibody are generally optimized for continuous-time development of physical systems. For real-time development, specialized physical system software such as V-Rep and Gazebo are often used in the literature. V-Rep was utilized in this work for all real-time tests. What is shown in Figure 6.19 is one of many physical system simulations developed in V-Rep for the analysis of fully-actuated hexrotor control, where the fully-actuated hexrotor is being commanded to track a QR code rigidly fixed to a ground platform. The ground platform maps the environment with a planar Lidar, thus the hexrotor may localize itself in the workspace. This simulation was built from an existing simulation within the V-Rep library, where the hexrotor was built from primitives in a custom stack. V-Rep is useful due its ROS compatibility and real-time control functionality. For the development of the hexrotor in V-Rep, the controller tuned in the Simscape environment was discretized

and implemented. Further details on specific implementations of the hexrotor in V-Rep are provided in the Applications section of this paper.

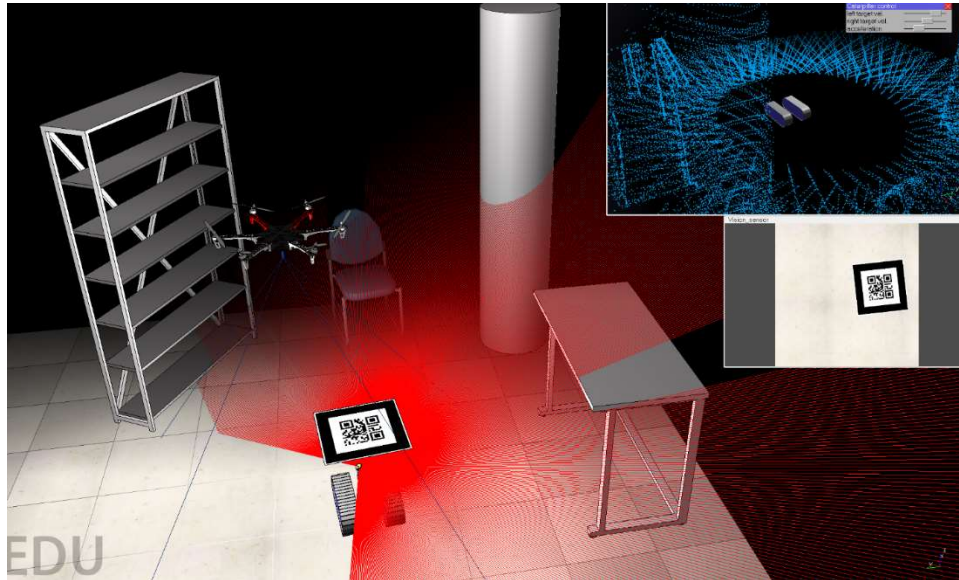


Figure 6.19. Discrete controller testing in the V-Rep environment.

6.4 Experimental Verification

In this section several analytic concepts and parameters developed in the theory of this work were developed experimentally. First the rotor model for thrust and drag, posited to be of linear form proportional to square rotor speed was evaluated via experimentation using a Force/Torque sensor made by ATI. The development of saturation limits using the developed custom flight stack flashed to a Pixhawk flight controller were evaluated, and a case study in cross span compensation was introduced here.

6.4.1 Rotor Testing and Model Verification

To refresh the reader on the form of the motor model, the projected motor frame force and torque developed by rotor spin was developed in Eq. (2.1). It was posited to be of the form repeated here in

$$\begin{aligned}\mathcal{M}\mathbf{F} &= [0 \quad 0 \quad b\omega_i^2]^T, \\ \mathcal{M}\boldsymbol{\tau} &= [0 \quad 0 \quad q_id\omega_i^2]^T,\end{aligned}\tag{6.4}$$

for convenience, where b and d are linear constant coefficients, $q_i = -\text{sgn}(\omega_i)$, and ω_i is the rotor angular velocity. The accuracy of the motor model depends on many factors including environment cross wind at the time of experiment and propeller flex [6]. Considerations beyond the simplified model, however, are often impractical to quantify and implement in application. To maintain simplicity and focus on the effects of rotor orientation, this work focuses on identifying an accurate base model, and does not consider external factors. The controlled experimental setup shown in Figure 6.20 was used to determine the scalar coefficients for thrust and drag b and d , where the rotor tested was the T-Motor MN4006 AntiGravity Brushless motor, and the propeller used was the Multistar Timber T-Style Propeller 13x4.4.



Figure 6.20. T-Motor MN4006 AntiGravity Brushless motor and Multistar Timber T-Style Propeller 13x4.4 mounted to an ATI mini-45 6-axis F/T sensor.

Motor and propeller manufacturers do not provide aerodynamic data for their products in general, and numerical models are often less accurate than experimental data. Thus, it was necessary to test the propeller and motor pairing before performing any flight experiments. While there is not a set design methodology for choice of rotor and propeller pairing, there are manufacturer codes to consider, which may inform individual product performance. Brushless motors sold for UAV implementation are designated a so-called KV rating, which is meant to linearly correlate unloaded rotor RPM to applied armature voltage. For example, the MN4006 possesses a KV rating of 380KV, implying an unloaded RPM of 8436 RPM ($\sim 880 \left(\frac{rad}{s}\right)$) at 22.2V, the average voltage of a 6S Lipo battery. The impedance introduced by the propeller varies by specification, thus loaded RPM is often very different from unloaded RPM. Propellers are classified by two numbers in a propeller identifier, which is separated by the character “x”. The Multistar Timber T-Style Propeller used in this work possesses the identifier 13x4.4. The first number classifies the propeller diameter in inches, while the second number classifies the propeller pitch in inches. The pitch assumes no slip, thus assuming no propeller slip, the UAV travels the pitch distance for every revolution of the propeller. This is clearly not the case for a multirotor in hover, however, higher pitch numbers correlate to higher propeller attack angle, which affects lift and drag production.

By using a handheld tachometer and the 6-axis ATI force-torque sensor shown in Figure 6.20, motor data was collected and used to generate Figure 6.21. The instantaneous rotor angular velocity was measured and used to correlate rotor frame thrust and drag. It should be noted that the square rotor speed was used for this correlation.

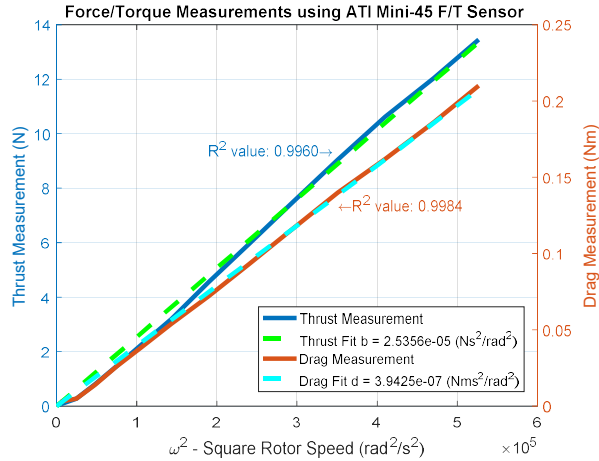


Figure 6.21. Measure F/T data for the MN4006 and Multistar Timber T-Style Propeller 13x4.4 pairing

The force and torque data was interpreted using linear regression with correlation fittings calculated at $R_{thrus}^2 = 0.9960$ and $R_{drag}^2 = 0.9984$, respectively. This high correlation supports the use of equation (2.1) as a rotor model in the developed UAV controller and experiments.

While the experiment described in Figure 6.20 was useful in evaluating the rotor and propeller pairing, the correlation between user-desired control and rotor speed cannot be quantified empirically. There are several factors impeding its description. Firstly, the timing of a brushless DC motor's phase progression is typically never directly determined by the flight controller. In multirotor implementations, a device called an electronic speed controller (ESC) receives a signal from a flight controller, generally pulse width modulation (PWM), and outputs its own timing in a pseudo 3-phase configuration to directly affect the brushless motor. Depending on the ESC firmware and model, the timing can vary significantly. Several advanced ESCs are programmable with both intermediate timing high efficiency, or high timing low efficiency modes. These modes support lower or higher rotor torque output depending on the desired application, and affect the rotor speed for any desired user-control signal. A further complication for this mapping is the applied voltage. Since most ESCs do not possess a voltage regulator, varying battery levels produce varying torque outputs for similar motor timings. While there is often firmware support in generic

flight control stacks such as ArduPilot Mega (APM) and PX4 for battery level depletion over time, this compensation is inherently approximate. Where the correlation in Figure 6.21 is valid for indoor applications with no turbulence considerations using the MN4006 rotor and Multistar Timber T-Style Propeller 13x4.4, the mapping described in Figure 6.22 is valid in a much smaller scope of use-cases. The flight controller used in this work was the Pixhawk flight controller flashed with a custom APM flight stack. The Pixhawk hardware abstraction layer (HAL) serves as an interface between user defined code and the signaling I/O hardware lines. HAL sets all servo lines to operate at 400Hz by default, though this is also programmable. While ESC communication varies by model, the ESCs used in this work were chosen to be the X-Rotor 40A. This ESC accepts servo signals at refresh rates of approximately 50-400Hz. The higher timings result smoother performance, while the lower timings provide more reliable data transmission. The length of logic voltage in μs is interpreted for use in generating the output timing, while the range of timings are mapped over a user controlled calibration. The data shown in Figure 6.22 was recorded using a raw control mode, where precise motor timings were tested over the ESC range of operation after ESC calibration, and the voltage level was set to 22.2V on the experimental setup shown in Figure 6.20. This result is specific to the designed platform's specification, and should be considered accordingly.

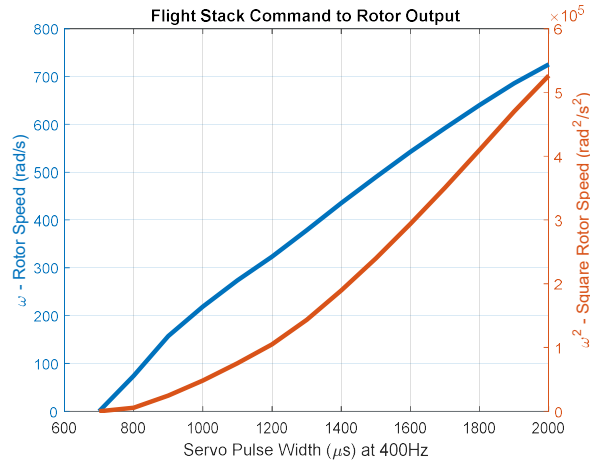


Figure 6.22. Experimental Pixhawk flight controller servo timing correlation to rotor speed using an MN4006, Multistar Timber T-Style Propeller 13x4.4, X-Rotor 40A ESC, and 6S Lipo Battery after Calibration.

Based on these results the chosen saturation limit for simulation was set to $\omega_{max} = 750 \frac{rad}{s}$ as stated in the relevant sections.

6.4.2 Force Saturation and the Planar Efficiency Metric

To verify the efficiency metric results, the experimental setup shown in Figure 6.23 and Figure 6.24 was used for all force testing of the completed prototype.

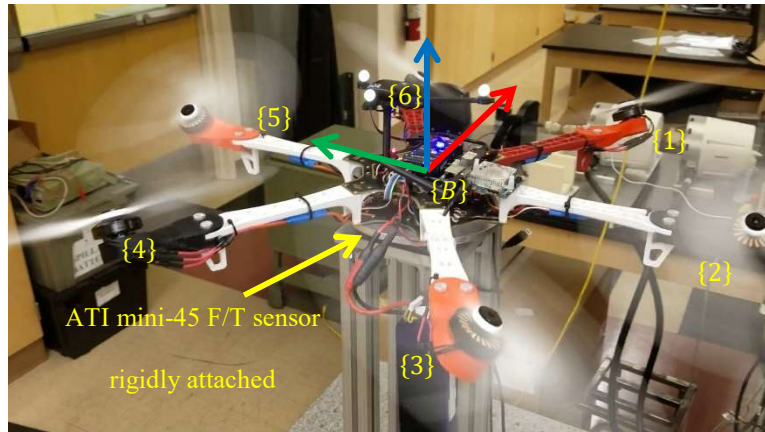


Figure 6.23. Experimental fully-actuated force/torque setup. An ATI min-45 6 axis F/T sensor was used to measure the prototype’s force/torque profiles.

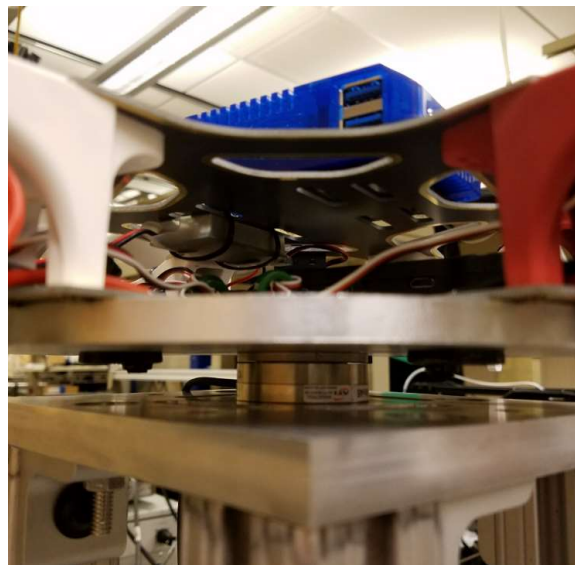


Figure 6.24. Side view of the airframe rigidly attached to the mini-45 6 axis ATI F/T sensor.

Further details on the development of the prototype are provided in the chapter titled “Prototype Development (refer to pg. 81)”. For this analysis it is sufficient to describe this design as conforming to Eq. (3.30) and Eq. (3.31), where the prototype utilized the MN4006 Antigravity rotors tested in Figure 6.21. The prototype was mounted rigidly to an ATI mini-45 6 axis F/T sensor, which recorded all force and torque measurements in this study.

The prototype design tilt was chosen to be $\beta = \frac{\pi}{6}$, the cross-span $L = 0.7024m$, the rotor configuration $\alpha = \frac{\pi}{2}$, and the rotor spin $q_1 = -1$. For the first test in this analysis, positive forward force efficiency $\epsilon_{n,x+}$ was tested at saturation. Utilizing ω_n a vertical force of $F_z = 11.2N$ was recorded and the forward force differential was pushed to saturation. That is forward differential was pushed until rotors {2} and {5} were forced into saturation at $0 \frac{rad}{s}$. The forces recorded during this test are shown in Figure 6.25.

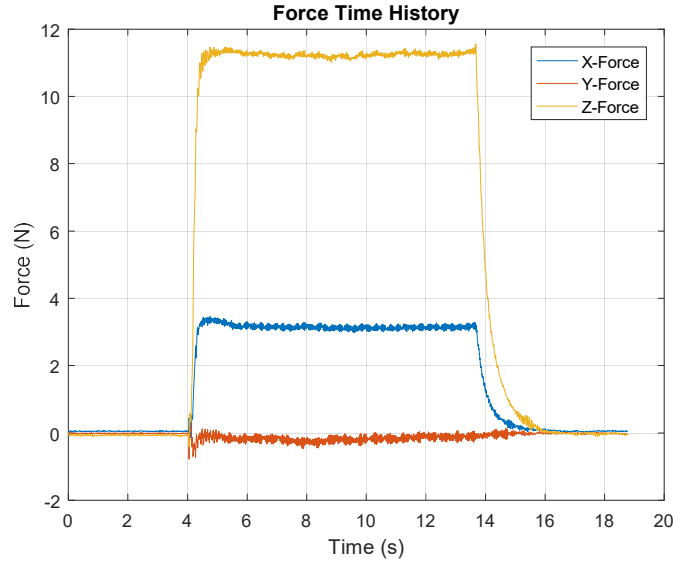


Figure 6.25. Forward force saturation test. All forces recorded.

The estimated maximum planar force projection was estimated to follow $\epsilon_{n,x+} = \frac{1}{4} t \beta^2$. For $\beta = \frac{\pi}{6}$, the theoretical maximum forward efficiency, denoted $(\epsilon_{n,x+})_t$, was calculated to be $(\epsilon_{n,x+})_t = 0.06501$. For the control test in Figure 6.25 the measured maximum forward force was measured to be 3.15 N, while the vertical throttle was again measured to be 11.2 N. Calculating the experimental forward efficiency, denoted $(\epsilon_{n,x+})_e = \frac{F_x^2}{F_z^2}$, resulted $(\epsilon_{n,x+})_e = 0.07910$. Finally, the percent error equation

$$E_{\epsilon_{n,x+}} = \frac{|(\epsilon_{n,x+})_e - (\epsilon_{n,x+})_t|}{(\epsilon_{n,x+})_t}. \quad (6.5)$$

provided high agreement with the estimate at 5.08%. It should be noted that this difference between theoretical and measured efficiency metric was likely caused by imperfections in the prototype design, user-introduced experiment error, and flexing due to nonrigid motor mounts. This experiment validated the planar force efficiency metric for a single data point concerning the constraint space in Figure 4.1, and this process can be repeated to validate the limiting efficiency metric in all directions.

The second experiment focused on the controller use-case. When developing a flight controller, appropriate safety regions for signal mixing must be established. For stable flight, UAV must be capable of arbitrary wrench production to counteract disturbances, thus saturation must be avoided for all times.

The custom flight controller written for use in flight applications originated from the underactuated APM flight stack, where a user can command a desired throttle, roll, pitch, and yaw to pilot a multirotor. For the development of the fully-actuated prototype, the controller mixer had to be changed in order to accommodate the 6 channel controller. The completed flight controller was tested first on the F/T setup described in Figure 6.23 and Figure 6.24. Once armed and actuated, throttle was increased to hover conditions, and maximum forward and lateral commands were tested. The force test is shown in Figure 6.26 was recorded for a free flight test with the completed controller. Details on flight stack development are provided in the Firmware and Reference Control section of this paper.

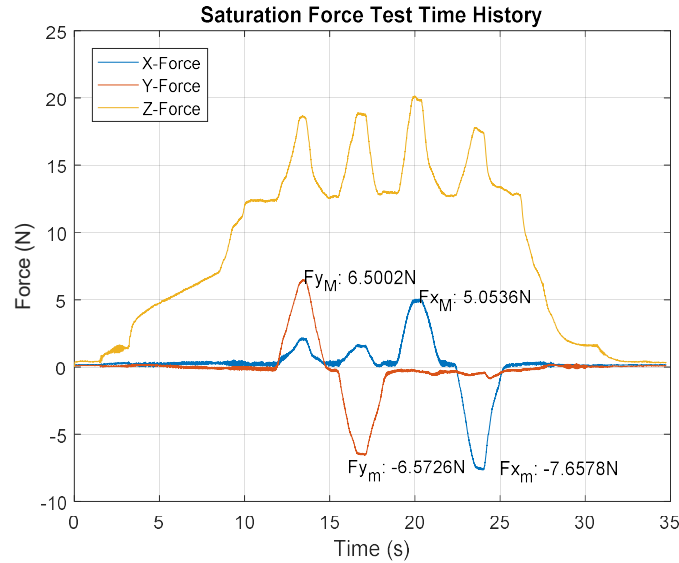


Figure 6.26. APM flight stack saturation test measured force outputs.

The forces indicated on Figure 6.26 correspond to maximum and minimum channel desired planar forces expressed by the prototype as restricted by the custom flight stack. In implementation, the output was reduced by a scaling factor of 0.5 statically. That is, before mixing occurs, the flight controller commands half of its maximum capability at any time. The reasoning was made apparent in Figure 6.27, where the power factor $c_p = 0.5$ corresponds to the maximum scaled constrained planar force output independent of direction. Because fully-actuated hexrotor are constrained by a triangular geometry, power factors above 0.5 imply directional considerations of saturation. Figure 6.27 illustrates the platforms maximum force constraints in light green, the controller-imposed force constraints in dark green, and the normed power factor metric of the scaled test shown in Figure 6.26. For the 15 seconds of the test shown, the planar efficiency metric is explicitly constrained by the triangular plane imposed by the controller. The airframe is effectively incapable of saturating the rotors due to pure planar force expressions in this configuration.

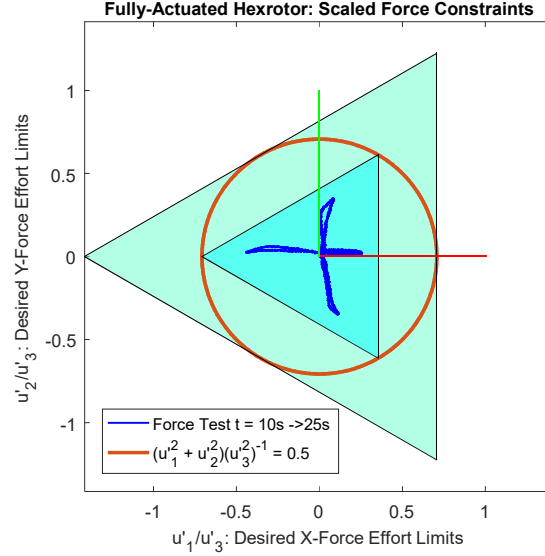


Figure 6.27. Evaluation of scaled efficiency metric in the APM flight stack test.

6.4.3 Cross-Span Compensation Case Study

In this section, cross-span compensation is discussed. The efficiency metrics for roll and pitch production in Eq. (4.5) will vary significantly depending on the design parameters. The metrics for roll and pitch, however, can be compensated via adjustment of the cross span. To demonstrate the scale of such a compensation, a simple case is presented in Table 6.2 for a hexrotor based on a parallel hexrotor of cross span $L_j = 550$ mm. The drag to thrust ratio was taken to be that of the prototype, thus, $\frac{d}{b} = 0.0155m$. The rotor tilt for comparison was also taken to be that of the prototype, where $\beta = \frac{\pi}{6}$. As was interpreted from Figure 6.21, the MN4006 Antigravity motor thrust and drag parameters were calculated with high correlation over the square rotor speed space. Since the flamewheel 550 hexrotor airframe was used as the basis for the custom platform, the comparator cross span L_j was chosen accordingly. In Table 6.2 the roll pitch efficiencies $\epsilon_{\tau_x} = \epsilon_{\tau_y}$ are presented for three design models, where the cross-span L_i was set equal to the comparator cross-span L_j , the cross-span L_i was set equal to the approximate model introduced in Eq. (4.18), and the cross-span was set to the exact compensation model in Eq. (4.17). As demonstrated in Eq.

(3.30) and Eq. (3.31), there are 4 distinct configurations parameterized by β , which make up all possible fully-actuated solutions of the hexrotor design. However, when it concerns torque production efficiency metrics, there are only two distinctions made between the two configurations delineated by $sgn(\alpha) = -q_1$ and $sgn(\alpha) = q_1$. This is because there are two components which determine torque production on all axes, torque produced by drag, and torque produced by the application of force about some distance from the origin of the body fixed frame. The ratio $\frac{d}{b}$ represents a relative weighting on drag and thrust contributions at $\frac{L_i}{2}$. The approximate model in Eq. (4.18) considers only the contribution of thrust at the rotor arm distance, as thrust is the major contributor of torque for nonparallel multirotor at smaller design β .

Table 6.2. Experimental platform efficiency compensation for a 550 mm class hexrotor with $\frac{d}{b}$ ratio 0.0155m, and a design tilt of $\beta = \frac{\pi}{6}$

	L_i (m)	$\epsilon_{\tau_x} = \epsilon_{\tau_y} (sgn(\alpha) = -q_1)$	$\epsilon_{\tau_x} = \epsilon_{\tau_y} (sgn(\alpha) = q_1)$
$L_i = L_j$	0.5500	0.7998	0.7018
$L_i = \left \frac{L_j}{c_\beta} \right $	0.6351	1.0573	0.9443
$L_i = \left \frac{L_j}{c_\beta} \pm \frac{2d}{b} t_\beta \right $	0.6530, 0.6172	1	1

As is demonstrated by the case study in Table 6.2, without compensation, stabilization of attitude becomes costly in terms of power consumption and torque production. While there are simply too many variables in this design to parameterize distinct efficiency metrics for all possible designs, it can be inferred that larger multirotors will be affected more heavily by thrust effects than by pure drag effects, implying that for

hexrotors and octocopters of class 550 and above, the approximate model is sufficient for reduction of losses. In the case study, the approximate model reduced losses to $\approx \pm 5\%$, where the full compensation model allowed for unity efficiency at the cost of defining a drag to thrust ratio in the design process. The full expression of torque efficiency metrics were shown in Table 6.3 for the designed prototype cross span $L_i = 0.7024 m$.

Table 6.3. Experimental platform efficiency calculations for a 550 mm class hexrotor with propellers of $\frac{d}{b}$ ratio 0.0155, and a design tilt of $\beta = \frac{\pi}{6}$

	$sgn(\alpha) = -q_1$		$sgn(\alpha) = q_1$	
	$\epsilon_{\tau_x} = \epsilon_{\tau_y}$	ϵ_{τ_z}	$\epsilon_{\tau_x} = \epsilon_{\tau_y}$	ϵ_{τ_z}
$\beta = \frac{\pi}{6}$	1.2727	147.8572	1.1747	108.7349
$\beta = \frac{\pi}{4}$	0.8730	278.1794	0.7599	233.0049

While the two data points presented in Table 6.3 correspond to the prototype cross span at two discrete tilt angles, the efficiency metrics can be presented as parameterized curves concerning roll/pitch and yaw torque production. The torque efficiency curves for the prototype at arbitrary $\beta \in [0, \pi]$ are shown in Figure 6.28, where the comparator class is again of the form $L_j = 0.550 m$.

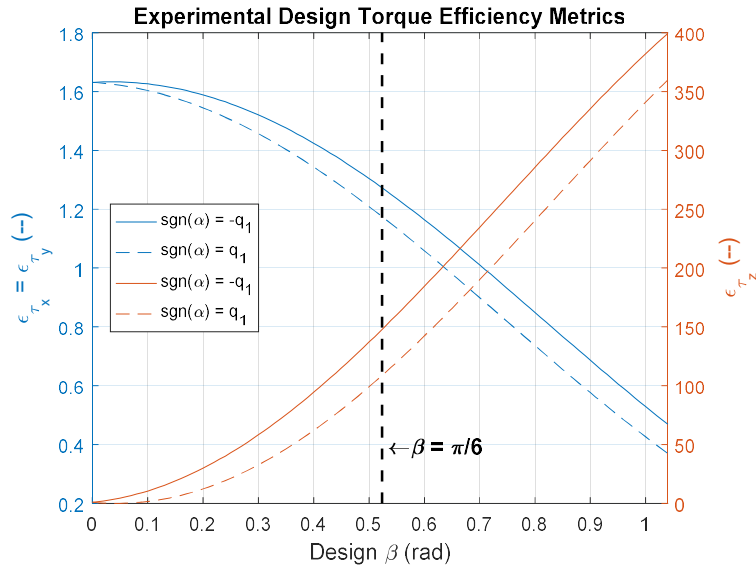


Figure 6.28. Torque efficiency metrics as a function of design β .

6.5 Firmware and Reference Control

The firmware for the developed fully-actuated hexrotor was developed from the open-source APM flight stack. The overarching function of the flight stack and its utilization in ROS applications is presented in this section.

6.5.1 APM Flight Stack Modification

The ArduPilot Mega (APM) firmware is an open-source project capable of real-time control of several types of radio controlled vehicles. Specifically, the code stack contains code bases for ground rovers, antenna trackers, fixed-wing aircraft, submersibles, and multicopter airframes. While the individual platform code bases are self-contained within their own directories, each code stack has access to various common libraries including generic attitude and altitude control definitions, sensor and navigation callbacks, and actuation and mixing defines.

For this project, the multirotor stack and its associated libraries were altered to accommodate the fully-actuated hexrotor prototype's unique flight mechanics. To allow the hexrotor to generate an arbitrary, both the airframe and controller definitions were modified.

At the time of this writing, the multicopter stack, called "ArduCopter", provided control options for quadcopters, hexrotors, octocopters, and helicopters in all manner of commercially available configurations. While it is not uncommon for contributors to add previously unsupported configurations to the stack, no airframe to date has supported control of fully-actuated UAV. To support fully-actuated flight, the code was altered by the addition of an airframe configuration, a new flight mode, and introduced definitions for forward and lateral mixing in the motor libraries.

By introducing new control definitions within a new flight mode, the multirotor maintains all functionality of traditional UAV, while possessing the capability of flying with six degrees of control via mode change. In testing, the UAV mode can be switched between any traditional flight mode such as STABILIZE, and the new definition called FULLY_ACT in the custom code through an external channel mid-flight. A generic parallel hexrotor is shown mid-flight in Figure 6.29. This platform was flashed with the modified APM flight stack, which supports fully-actuated flight. Since the modified code was written within the flight mode FULLY_ACT, it behaves as any parallel multirotor would in application using the STABILIZE mode. This type of modularity provides the platform with more desirable commercial prospects.



Figure 6.29. Hexrotor flight testing

STABILIZE is a flight mode which allows a user to control a UAV manually using 4 RC channels to affect throttle, roll, pitch, and yaw. Rather than control UAV actuation directly, STABILIZE modifies the user-requested effort to limit roll and pitch state deflection to within a stable range. The resulting flight performance is generally robust to inversion and can be controlled via RC transmitter or autonomously in a cascaded fashion.

Because the prototype was built compatible with existing control architecture, it can express decoupled roll, pitch, yaw, and throttle with the same differentials that all multirotor are expressly commanded to perform. As outlined in Figure 6.30, the prototype fully-actuated hexrotor was mounted to an ATI mini-45 F/T sensor in STABILIZE mode. Since the platform was rigidly mounted to the test bed, no close-loop control could be performed, thus mixing was disabled for this test. A mixed throttle and pitch command was issued resulting in the force and torque plots of Figure 6.31.

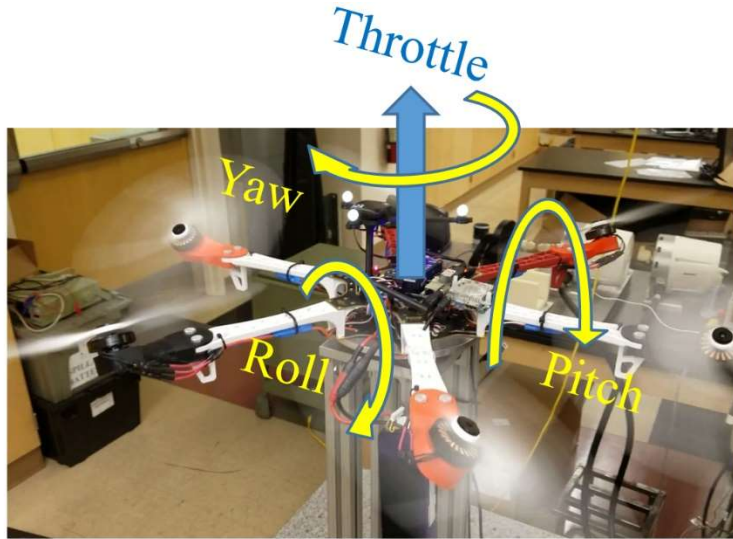


Figure 6.30. Fully-actuated hexrotor flashed with the custom APM firmware in STABILIZE mode.

As shown in Figure 6.31, pure pitch torque was produced along with vertical throttle.

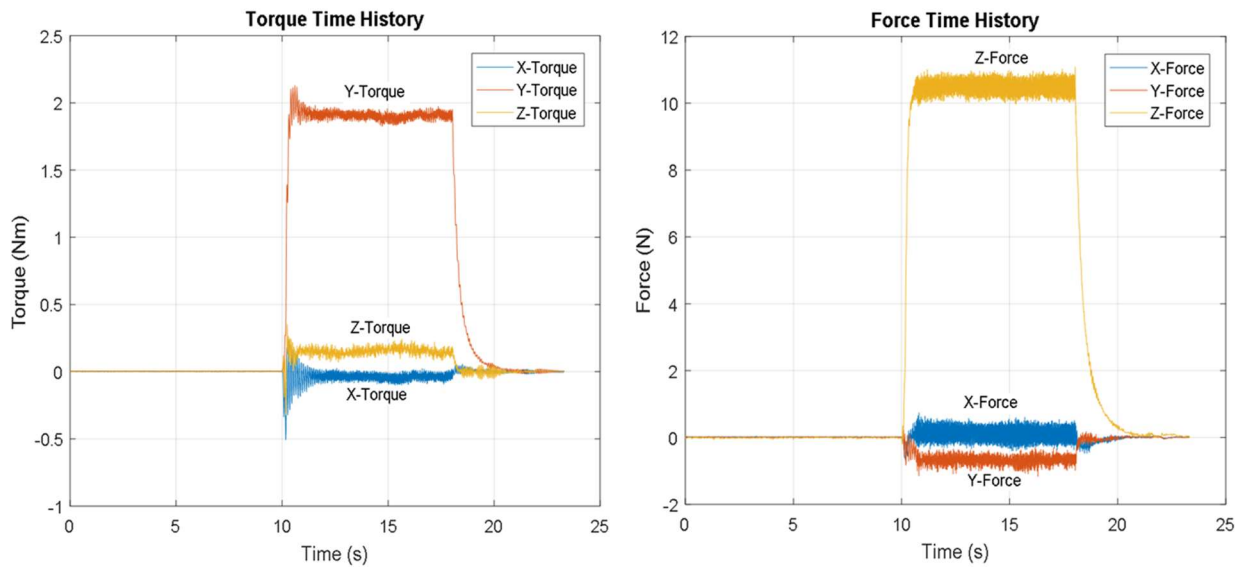


Figure 6.31. Unmixed force/torque time history for the fully-actuated hexrotor in STABILIZE.

While some output was detected in the forward, lateral, roll, and yaw directions, the dominating wrench features belong to throttle and pitch. The detected deviant output was likely caused by sensor error, and model deflection as rotor output caused slight flexing in the rotor arms. To test the platform's fully-actuated flight mode FULLY_ACT, the platform mode was changed via external RC command. The dominant wrench control in fully-actuated mode was designed to be controlled by 4 channels affecting the throttle, forward, lateral, and yaw directions. Since arbitrary roll/pitch deflections tend to saturate rotor output as demonstrated in the simulated output of Figure 6.13, roll and pitch were chosen to be regulated by default. The resulting configuration is outlined in Figure 6.32, where the force and torque output for a mixed throttle and forward command were recorded in Figure 6.33.

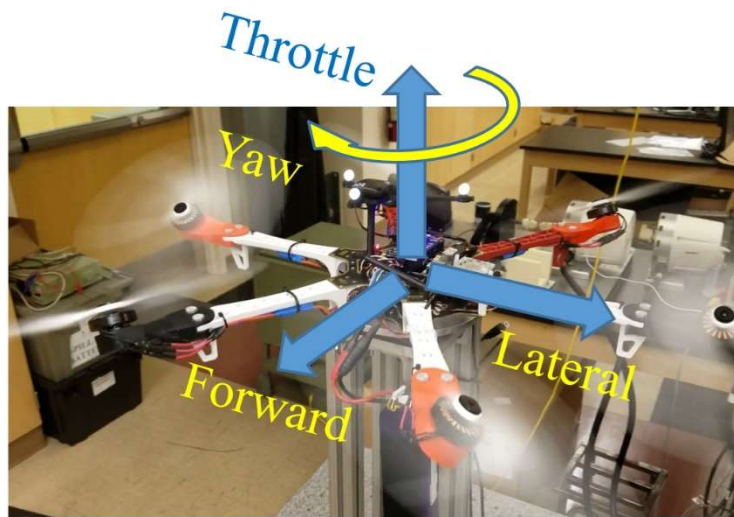


Figure 6.32. Fully-actuated hexrotor flashed with the custom APM firmware in FULLY_ACT mode.

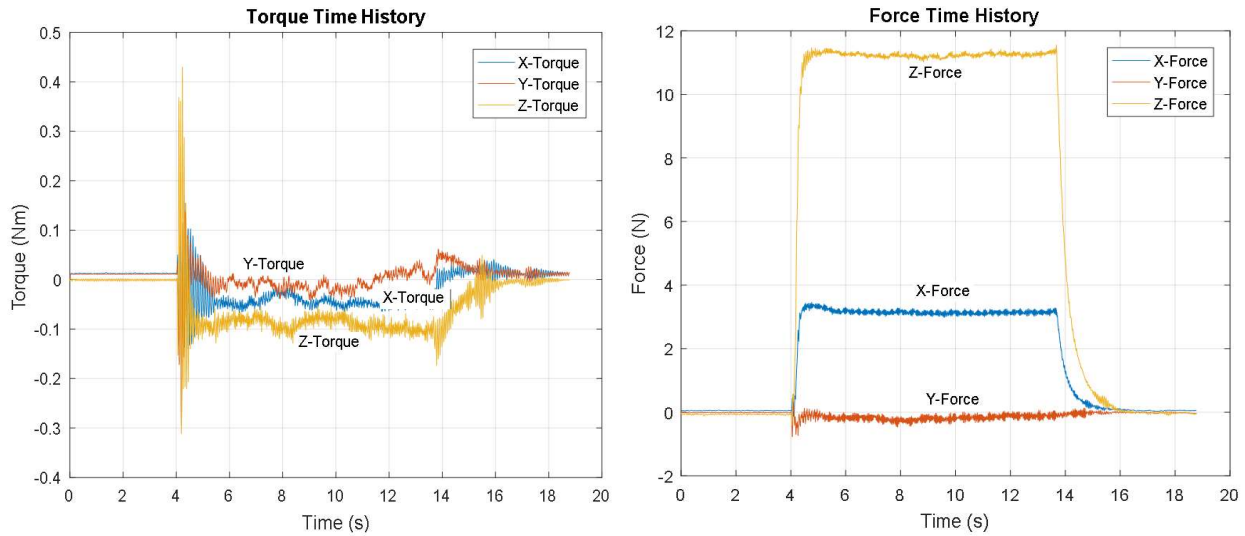


Figure 6.33. Unmixed force/torque time history for the fully-actuated hexrotor in FULLY_ACT mode.

The inclusion of the new flight mode FULLY_ACT allows a fully-actuated hexrotor designed as developed in this work to be controlled by either throttle, roll, pitch, and yaw in STABILIZE mode, or by throttle, forward, lateral, and yaw in FULLY_ACT mode. In the latter case, roll and pitch are regulated. Because most other flight modes defined in APM are built as subclasses of STABILIZE, each flight mode can easily be modified to accommodate the new flight mode. Often, as is the case with the flight mode ALT_HOLD, STABILIZE is used as the fundamental mode while accessing accessory definitions to achieve altitude hold. By adding FULLY_ACT to this definition, the fully-actuated flight mode attains access to this functionality. Concerning aerial manipulation, FULLY_ACT mode allows the platform to decouple roll/pitch dynamics from position tracking, thus its implementation is well-suited to aerial manipulation.

6.5.2 ROS Integration and Cascade Control

The Robot Operating System (ROS) has become the de-facto middleware for messaging and control in robotics applications [47]. For more details of its usage please refer to resources such as [48]. One core functionality of ROS is its anonymous messaging system. As shown in the example messaging network of Figure 6.34, a sensor or device supported by ROS drivers can publish data to what is known as a topic. In

the example shown a gas sensor is wired to device 2 of the network. As soon as the data is published, a master device will track that data and distribute it to any end-point requesting data associated with that topic. In this way, data is not directly linked to a specific device, rather, any device can publish or subscribe to any topic from any device. For the case in which device 2 becomes inaccessible or goes offline, the network remains intact. For all devices subscribing to a topic, the master node creates and maintains that topic.

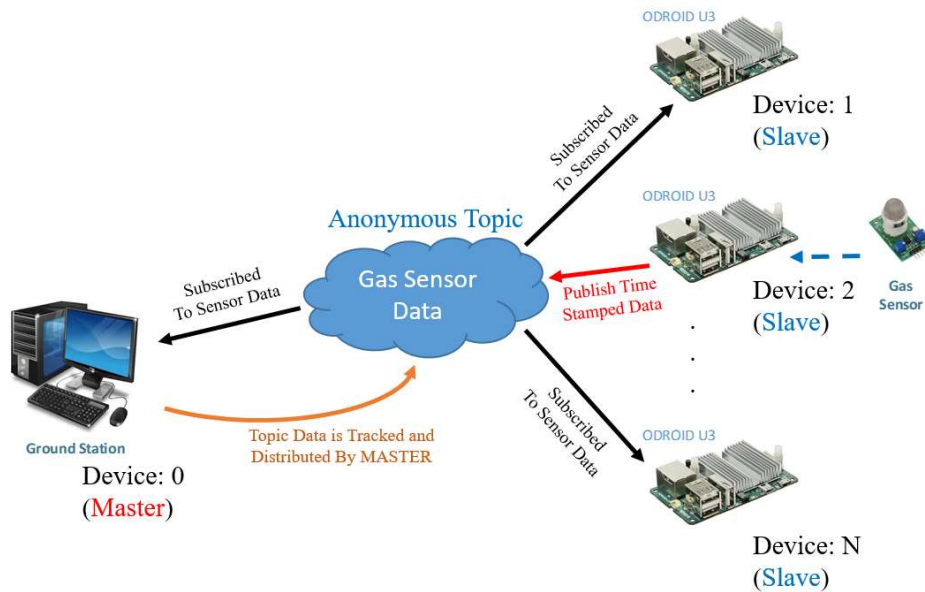


Figure 6.34. An example messaging diagram in simple ROS implementations.

In this work, ROS was utilized in a cascade setup for reference control of an internally stabilized subsystem such as is shown in Figure 6.35. For a UAV, the flight controller can implement real-time control of attitude and altitude. Overall positioning, however, cannot be controlled directly without external feedback or GPS. Often, as is the case with indoor applications, GPS is not available, and in practical application, GPS and barometer data are unreliable for precise positioning as is necessary in aerial manipulation.

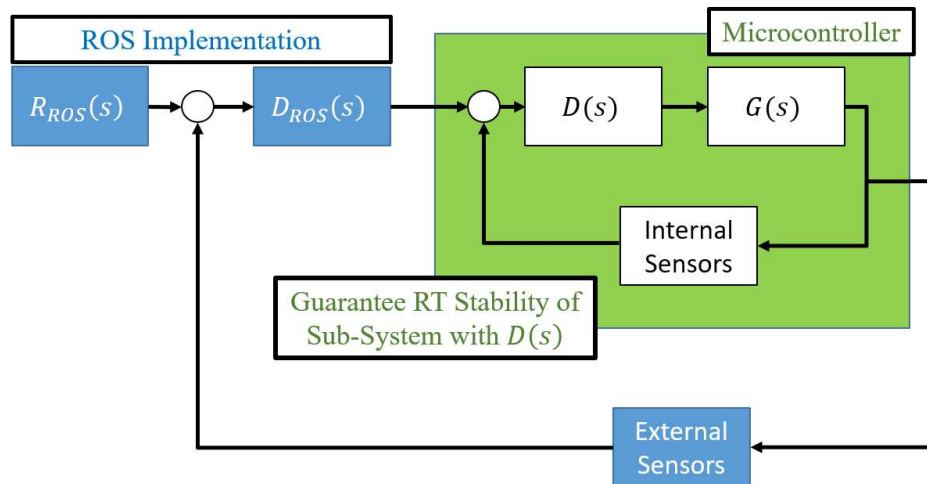


Figure 6.35. General framework for system control using ROS. Since ROS is not a real-time system, it cannot provide any stability guarantees in implementation.

One practical example of ROS implementation was performed using a webcam and a QR code to wirelessly localize the prototype in pseudo-real time. In the early stages of platform development, the aerial manipulator was suspended such that platform localization and manipulator target tracking could be tested. A webcam was mounted to the airframe as depicted in Figure 6.36. The webcam reported camera data to the attached ODROID XU4, where a ROS slave reported the data to an instance of a ground station ROS master over wifi. The ground station processed the camera data using ViSP libraries to report time stamped pose information. The pose information was then relayed back to the ODROID XU4 for use in localization. The output of the ViSP processing is shown in Figure 6.37. The reported pose was referenced in terms of the camera frame, thus, for a known camera pose relative to the body-fixed frame, the target QR code could be used to localize the platform in space with high precision. In the test shown in Figure 6.36, the manipulator was controlled via an Arbotix-M microcontroller. The manipulator was tasked with tracking the QR code for arbitrary placement of the target.

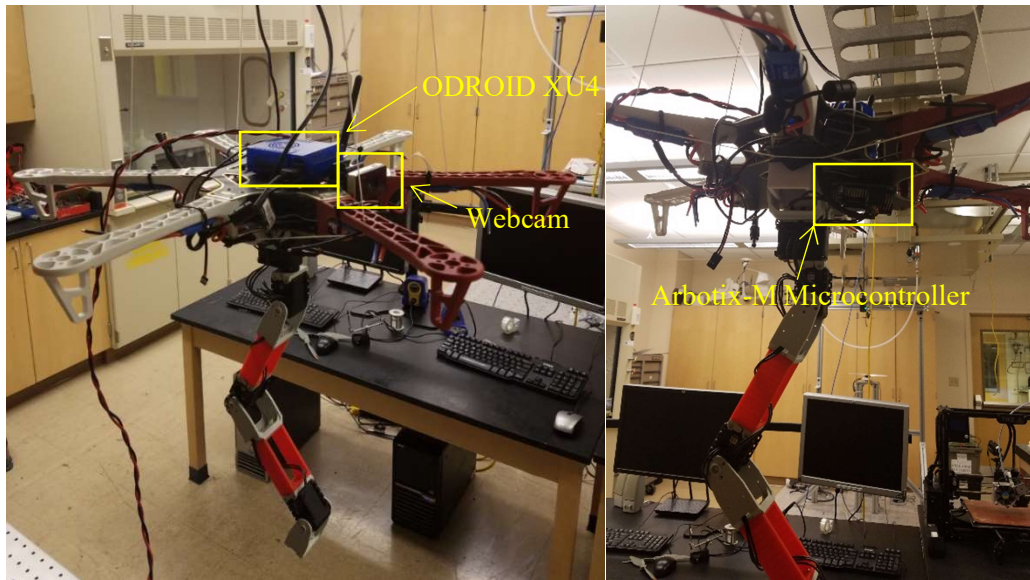


Figure 6.36. Early development of the prototype and localization using a camera.



Figure 6.37. QR code detection and pose estimation of the target.

The manipulator reference controller was customized to allow for ROS definition of cartesian, cylindrical, and joint space control of the end effector. Since the form of the manipulator was that of a 3R manipulator a unique explicit solution was resolved by defining the orientation and position of the end effector link. As

depicted in Figure 6.38, the end effector was tasked with performing a vertical maneuver along the aluminum target in a simple tracking test. The flexibility to control a manipulator via ROS in several spatial definitions allowed for convenient tracking and control of the manipulator in the aerial manipulation tests.



Figure 6.38. Cartesian control of a 3R manipulator. The manipulator is controlled via reference command of end-effector tip position.

When mounted to the parallel hexrotor model, aerial manipulation was shown to be possible using the ROS framework as was demonstrated in the test shown in Figure 6.39. In this test, an Optitrack system was used to affect autonomous position hold of the UAV, while the manipulator was actuated in cylindrical frame reference control. The extent to which the platform could reject forward and lateral force disturbances was severely limited, however, as the platform fought to maintain position via non-zero tracking of roll and pitch. The roll and pitch tracking affected the end effector position, thus, convergence of the system to a manipulator target frame was impractical.



Figure 6.39. Closed-loop parallel hexrotor aerial manipulation test.

The developed fully-actuated hexrotor is shown in Figure 6.40 mid-flight mounted with the same manipulator system. Not only is this platform stable in hover, it was capable of rejecting forward and lateral force disturbances without coupled roll/pitch maneuvers to affect forward and lateral motion.

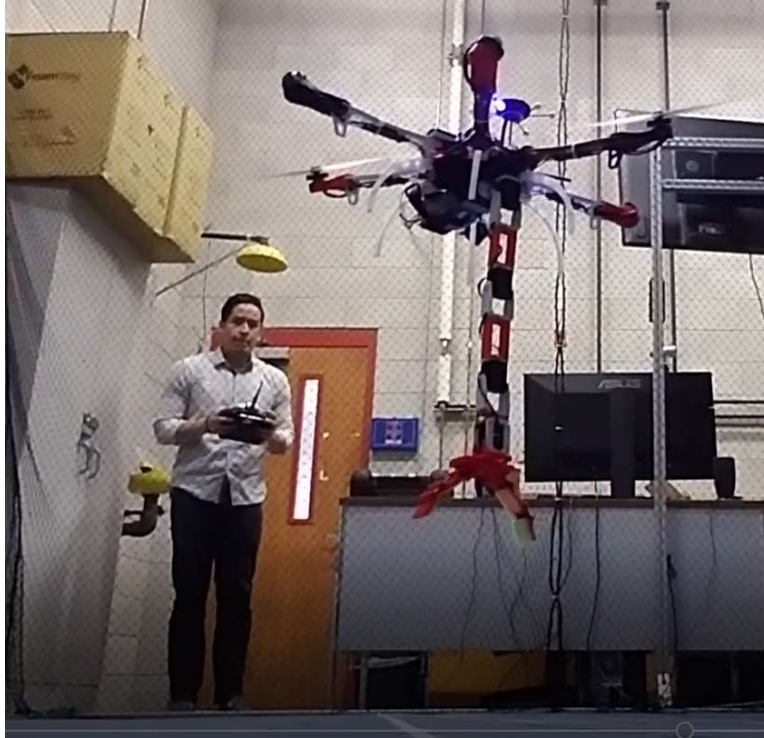


Figure 6.40. Nonparallel hexrotor flight test towards aerial manipulation.

The position and orientation plots shown in Figure 6.41 demonstrate the platform's ability to translate in the global x and y directions without intentional tracking of non-zero roll and pitch states.

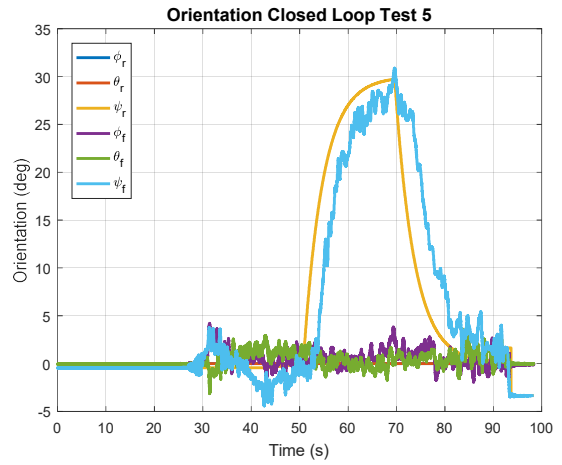
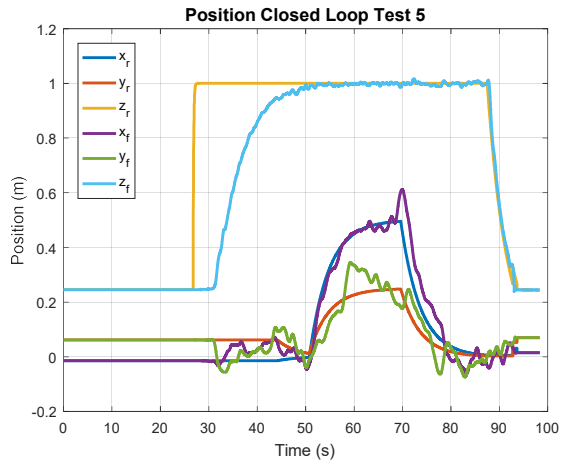


Figure 6.41 Position and orientation of the fully-actuated hexrotor in a closed-loop test.

7 Applications

In this section several applications are discussed concerning the usage of fully-actuated hexrotors. Historically, multirotor UAV have been used exclusively for passive remote sensing. Nonparallel fully-actuated hexrotors provide end-users with the opportunity to perform more robust active remote environment interactions. A project funded by Savannah River Nuclear Solutions LLC. was first described concerning such interactions, where the user interface and sensing network were discussed as they relate to radiation detection and sample collection applications. A nonlinear model reference adaptive controller (MRAC) was then introduced to inform the estimation of manipulator payload mass. Where passive sensing may allow for the detection and location of objects in-situ, the ability to estimate sample density or mass is not readily available under normal circumstances. The method of payload estimation discussed pertains to aerial manipulators and the interpretation of rotor effort when grasping an object.

7.1 Remote Sensing and Sample Collection

UAV implementation is often limited to remote sensing, but in the presented work a mixed implementation of passive sensing and active environment interaction is introduced. In the octocopter aerial manipulator setup shown in Figure 7.1, a gas sensor, radiation sensor, heat sensing FLIR camera, planar LIDAR sensor, and manipulator were mounted to the UAV. Because the ROS framework was utilized for sensor messaging, each device was developed in a plug-and-play network, where a device would automatically report data when plugged into the onboard computer. Each device was configured as shown in Figure 7.2, where a linux computer called an ODROID U3 was utilized to relay sensor and actuator data to a ground station, and receive global commands from the user. A Pixhawk flight controller and Arduino Mega were used to control the UAV and manipulator individually.



Figure 7.1. Octocopter aerial manipulator platform setup with plug-and-play sensor and manipulator peripherals.

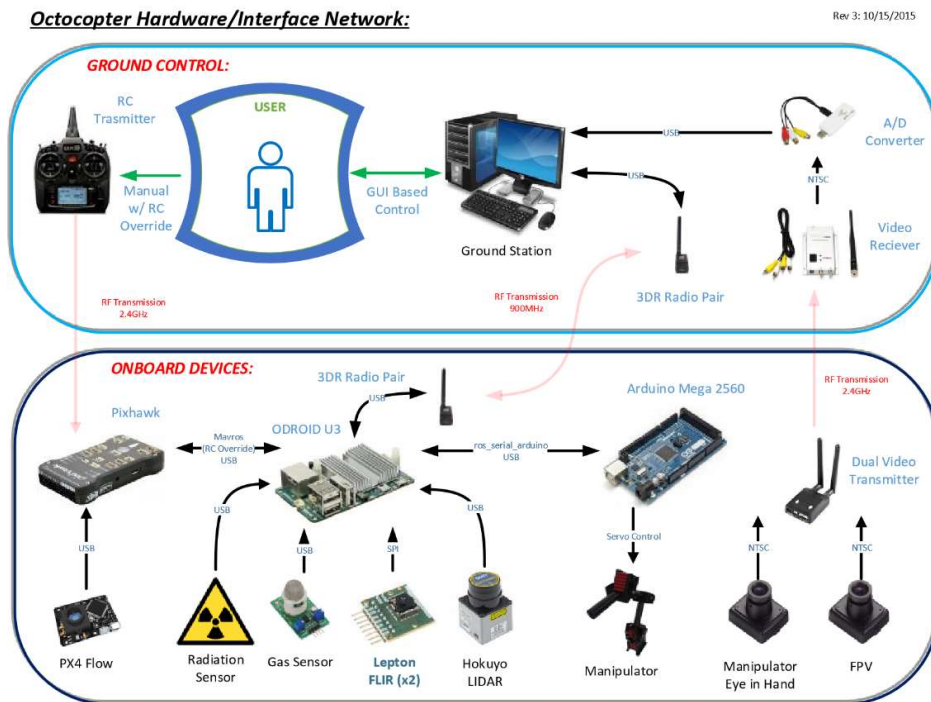


Figure 7.2. Sensor and manipulator communications network for the octocopter aerial manipulator.

While remotely deployed, the UAV was intended to collect soil and other samples from irradiated environments where human intervention was deemed too dangerous. The platform was designed to either grasp objects while perched or grasp objects from hover. By utilizing the camera transformations as described in Figure 7.3, a target object may be captured by the aerial manipulator.

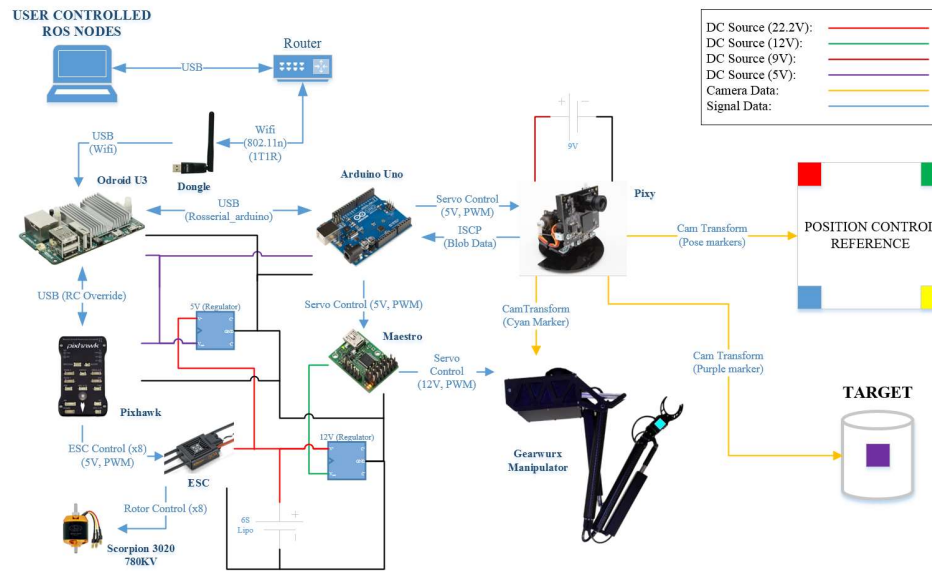


Figure 7.3. Manipulator power distribution and reference generation for the end-effector.

The custom GUI shown in Figure 7.4 depicts the user interface for the octocopter. A real-time camera feed is displayed to the GUI for user feedback and target tracking. The GPS data reported back to the ground station is relayed to the GUI and the user was given global control of each autonomous action of the multirotor.

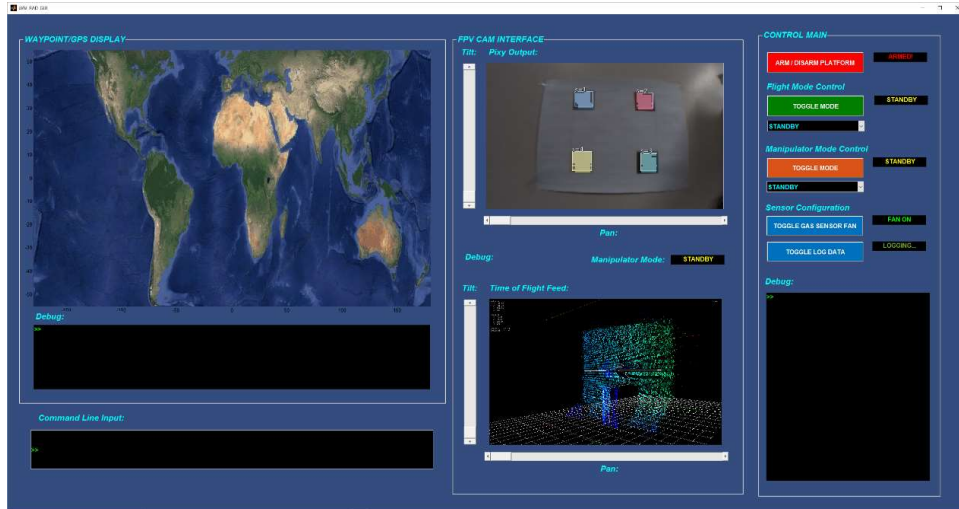


Figure 7.4. Custom GUI for remote control of the octocopter aerial manipulator.

To test position control and localization of the platform, a simulation was developed in V-Rep, where a color target was identified by a camera, and autonomous tracking was demonstrated. The method can be scaled to a real multirotor given adequate target identification.

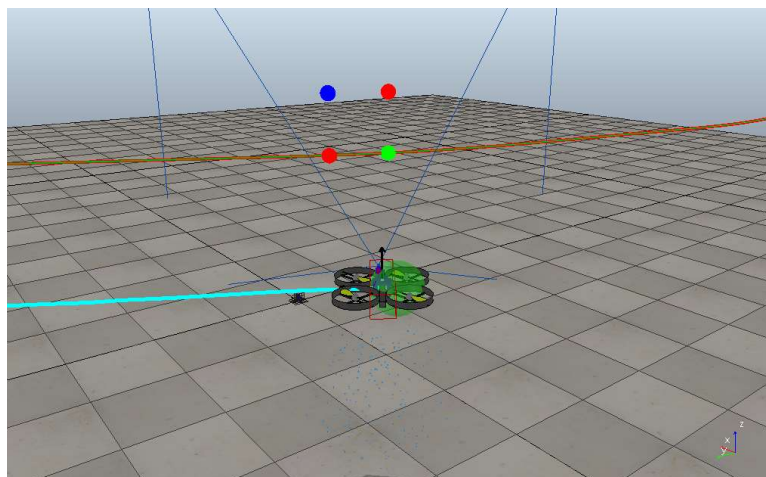


Figure 7.5. Flight simulation of UAV position localization and control using a moving color coded target.

The camera and overhead view of the simulation was displayed in Figure 7.6. The target path was shown in red, where the cyan path shows the UAV path in time. An arbitrary position offset was chosen such that the platform performed camera frame position regulation to converge the target reference position.

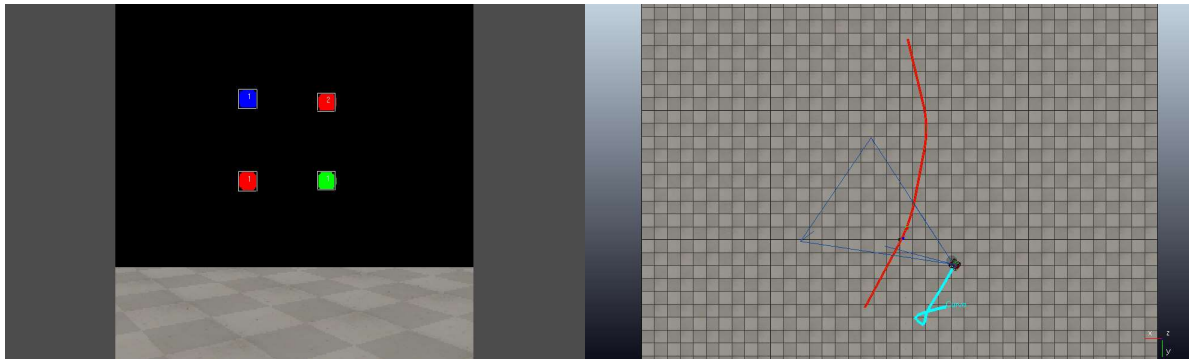


Figure 7.6. Camera and overhead view of the localization and positioning simulation.

7.2 Payload Mass Estimation

In this section an implementation of model reference adaptive control (MRAC) is derived for both stable control and parameter estimation of center of mass location. In this specific analysis, it is shown that the torque produced about the x and y axes for non-zero center of mass provides a persistently exciting torque function for the convergence of parameter estimates. To refresh the reader on the attitude dynamics of a multicopter, the dynamic Euler equations were redefined in

$${}^B\dot{\boldsymbol{\omega}} = f_2^*(\boldsymbol{\varepsilon}_{\Theta_B}, {}^B\boldsymbol{\omega}) + g_2^*{}^B\boldsymbol{\tau}.$$

$$f_2^*(\boldsymbol{\varepsilon}_{\Theta_B}, {}^B\boldsymbol{\omega}) := {}^B J^{*-1} (S({}^B J^* {}^B\boldsymbol{\omega}) {}^B\boldsymbol{\omega} + {}^B \mathbf{P}_C^* \times R_{\Theta}^T \mathbf{F}_g - \sum_{i=1}^6 J_r({}^B\boldsymbol{\omega} \times {}^B R_{S_1} S_1 \boldsymbol{\Omega}) + \boldsymbol{\tau}_w), \quad (7.1)$$

$$g_2^* := {}^B J^{*-1},$$

where the center of mass location ${}^B \mathbf{P}_C$ has been redefined as ${}^B \mathbf{P}_C^*$ to stress that the parameter used in this formulation represents the true value of ${}^B \mathbf{P}_C$. From the analysis backstepping, the designer's choice stable Euler dynamics were chosen to be of the form

$$\boldsymbol{\Lambda}_{u,2} = {}^B\dot{\boldsymbol{\omega}}_d + (D_{21} + D_{22}){}^B\tilde{\boldsymbol{\omega}} + (I + D_{22}D_{21}) \int_0^t {}^B\tilde{\boldsymbol{\omega}} dt, \quad (7.2)$$

$${}^B\tilde{\boldsymbol{\Theta}} := \int_0^t {}^B\tilde{\boldsymbol{\omega}} dt,$$

where ${}^B\tilde{\boldsymbol{\omega}}$ is known to be the body fixed angular velocity, and the variable ${}^B\tilde{\boldsymbol{\Theta}}$ is introduced for convenience. It should be reiterated that these states represent the inertial frame orientation and angular velocity as seen from the body-fixed frame. The definitions

$$Q({}^B\boldsymbol{\omega}) := -S({}^B J^* {}^B\boldsymbol{\omega}) {}^B\boldsymbol{\omega} + \sum_{S_1=\{1\}}^{\{n\}} J_r({}^B\boldsymbol{\omega} \times {}^B R_{S_1} S_1 \boldsymbol{\Omega}) - \boldsymbol{\tau}_w + {}^B J^* \boldsymbol{\Lambda}_{u,2}, \quad (7.3)$$

$$W_1(\boldsymbol{\varepsilon}_{\Theta_B}) := \begin{bmatrix} 0 & m^* g c_\theta c_\phi & -m^* g c_\theta s_\phi \\ -m^* g c_\theta c_\phi & 0 & -m^* g s_\theta \\ m^* g c_\theta s_\phi & m^* g s_\theta & 0 \end{bmatrix},$$

were then introduced to express the deterministic control law in the form

$${}^B\boldsymbol{\tau}^* = W_1(\boldsymbol{\varepsilon}_{\Theta_B}) \mathbf{k}_1^* + Q({}^B\boldsymbol{\omega}), \quad (7.4)$$

$$\mathbf{k}_1^* := {}^B \mathbf{P}_C^*.$$

Assuming the parameter of interest ${}^B\mathbf{P}_c^*$ is unknown, the estimate of ${}^B\mathbf{P}_c^*$, ${}^B\mathbf{P}_c(t)$, can be used to define an adaptive control law

$$\begin{aligned} {}^B\boldsymbol{\tau}(t) &= W_1({}^\varepsilon\boldsymbol{\Theta}_B)\mathbf{k}_1(t) + Q({}^B\boldsymbol{\omega}), \\ \mathbf{k}_1(t) &:= {}^B\mathbf{P}_c(t). \end{aligned} \tag{7.5}$$

Substituting the adaptive control law in Eq. (7.1) results

$${}^B\dot{\boldsymbol{\omega}} = f_2^*({}^\varepsilon\boldsymbol{\Theta}_B, {}^B\boldsymbol{\omega}) + g_2^*{}^B\boldsymbol{\tau}^* + g_2^*({}^B\boldsymbol{\tau}(t) - {}^B\boldsymbol{\tau}^*). \tag{7.6}$$

By applying the deterministic control law and utilizing the parameter estimate error $\tilde{\mathbf{k}}_1(t) := \mathbf{k}_1(t) - \mathbf{k}_1^*$, the Euler dynamics were determined to be of the form

$${}^B\dot{\boldsymbol{\omega}} = \boldsymbol{\Lambda}_{u,2} + g_2^*W_1({}^\varepsilon\boldsymbol{\Theta}_B)\tilde{\mathbf{k}}_1(t). \tag{7.7}$$

Again, it was determined from the backstepping analysis of the deterministic approach that ${}^B\dot{\boldsymbol{\omega}} = \boldsymbol{\Lambda}_{u,2}$ provide asymptotically stable error dynamics. The addition of $g_2^*W_1({}^\varepsilon\boldsymbol{\Theta}_B)\tilde{\mathbf{k}}_1(t)$ introduces some disruption to that stability, thus it should be inspected. The p.d. Lyapunov function

$$V_a = \frac{1}{2}{}^B\tilde{\boldsymbol{\Theta}}^T J^* {}^B\tilde{\boldsymbol{\Theta}} + \frac{1}{2}({}^B\tilde{\boldsymbol{\omega}} + D_{21}{}^B\tilde{\boldsymbol{\Theta}})^T J^* ({}^B\tilde{\boldsymbol{\omega}} + D_{21}{}^B\tilde{\boldsymbol{\Theta}}) + \frac{1}{2}G^{-1}\tilde{\mathbf{k}}_1^T\tilde{\mathbf{k}}_1 > 0, \tag{7.8}$$

is introduced to assess the effects of parameter estimation on stability. The derivative of the Lyapunov candidate was shown in

$$\begin{aligned} \dot{V}_a &= {}^B\tilde{\boldsymbol{\Theta}}^T J^* {}^B\dot{\tilde{\boldsymbol{\omega}}} + ({}^B\tilde{\boldsymbol{\omega}} + D_{21}{}^B\tilde{\boldsymbol{\Theta}})^T J^* ({}^B\dot{\tilde{\boldsymbol{\omega}}} - \boldsymbol{\Lambda}_{u,2} - g_2^*W_1({}^\varepsilon\boldsymbol{\Theta}_B)\tilde{\mathbf{k}}_1(t) + \\ &D_{21}{}^B\dot{\tilde{\boldsymbol{\omega}}}) + G^{-1}\dot{\tilde{\mathbf{k}}}_1^T\tilde{\mathbf{k}}_1, \end{aligned} \tag{7.9}$$

where the Euler dynamics were substituted in the formulation. After simplification of the equation, the derivative of the Lyapunov candidate was resolved to

$$\begin{aligned} \dot{V}_a = & -{}^B\tilde{\Theta}^T D_{21}^T {}^B J^* {}^B\tilde{\Theta} - ({}^B\tilde{\omega} + D_{21} {}^B\tilde{\Theta})^T {}^B J^* D_{22} ({}^B\tilde{\omega} + D_{21} {}^B\tilde{\Theta}) - ({}^B\tilde{\omega}^T {}^B J^* + \\ & {}^B\tilde{\Theta}^T D_{21}^T {}^B J^*) g_2^* W_1(\varepsilon_{\Theta_B}) \tilde{\mathbf{k}}_1(t) + G^{-1} \tilde{\mathbf{k}}_1^T \tilde{\mathbf{k}}_1. \end{aligned} \quad (7.10)$$

By choosing an adaptive control law for the unknown parameters

$$\dot{\tilde{\mathbf{k}}}_1^T = [G({}^B\tilde{\omega}^T + {}^B\tilde{\Theta}^T D_{21}^T)] W_1(\varepsilon_{\Theta_B}), \quad (7.11)$$

The derivative of the Lyapunov candidate was shown to be negative semi-definite

$$\dot{V}_a = -{}^B\tilde{\Theta}^T D_{21}^T {}^B J^* {}^B\tilde{\Theta} - ({}^B\tilde{\omega} + D_{21} {}^B\tilde{\Theta})^T {}^B J^* D_{22} ({}^B\tilde{\omega} + D_{21} {}^B\tilde{\Theta}) \leq 0. \quad (7.12)$$

or simply, V_a is bounded. This implies ${}^B\tilde{\Theta}, {}^B\tilde{\omega}, \tilde{\mathbf{k}}_1 \in L_\infty$ and $\lim_{t \rightarrow \infty} V_a(t) = V(\infty) \leq V(0)$. Taking the negative integral of the derivative of the Lyapunov function results

$$\begin{aligned} -\int_0^\infty \dot{V}_a dt = & \int_0^\infty {}^B\tilde{\Theta}^T D_{21}^T {}^B J^* {}^B\tilde{\Theta} dt + \int_0^\infty ({}^B\tilde{\omega} + D_{21} {}^B\tilde{\Theta})^T {}^B J^* D_{22} ({}^B\tilde{\omega} + D_{21} {}^B\tilde{\Theta}) dt = \\ & V(0) - V(\infty) < \infty. \end{aligned} \quad (7.13)$$

Because the error terms are square integrable, ${}^B\tilde{\Theta}, {}^B\tilde{\omega} \in L_2 \cap L_\infty$. Reevaluating Eq. (7.7) with this knowledge, assuming bounded W_1 provides ${}^B\ddot{\Theta} \in L_\infty$. Finally, Barbalat's Lemma guarantees ${}^B\tilde{\Theta}, {}^B\tilde{\omega} \rightarrow \mathbf{0}$ as $t \rightarrow \infty$.

The analysis using Barbalat's Lemma guarantees state convergence only, however, and guarantees nothing for the parameter estimate error $\tilde{\mathbf{k}}_1(t)$ other than boundedness. To prove any convergence of the parameter estimate, some continued analysis should be performed to show the input is persistently exciting. For a locally bounded square integrable vector function $F(t)$ the following holds

$$\exists a, T, s_0, \int_s^{s+T} F(t)F^T(t) dt \geq aI_{n \times n} > 0, \forall s > s_0 \Rightarrow F(t) \text{ is P.E.}, \quad (7.14)$$

where a matrix A is said to be greater than a matrix B if $A - B$ is p.d. [49]. That is, if the function $F(t)$ is bounded square integrable, there should exist a time s_0 such that for all intervals of time larger than s_0 the relationship given should hold. Because it was shown that that state error converges to $\mathbf{0}$ asymptotically, the limit definition for the input torque reduces to

$$\lim_{t \rightarrow \infty} {}^B\boldsymbol{\tau}(t) = W_1(\mathbf{0})\mathbf{k}_1(t) + Q(\mathbf{0}), \quad (7.15)$$

at $t \rightarrow \infty$. The condition for persistent excitation is such that there must simply exist a time s_0 such that Eq. (7.14) holds for all times greater than s . Thus, if t is chosen sufficiently large, the analysis is simplified. If a stable hover command is given to the platform, there should then exist a t_0 such that ${}^B\boldsymbol{\tau}(t_0) = W_1(\mathbf{0})\mathbf{k}_1(t_0)$. Consider then

$$W_1(\mathbf{0})\mathbf{k}_1(t_0)(W_1(\mathbf{0})\mathbf{k}_1(t_0))^T = \begin{bmatrix} {}^B p_{y_c}^2 & -{}^B p_{y_c} {}^B p_{x_c} & 0 \\ -{}^B p_{x_c} {}^B p_{y_c} & {}^B p_{x_c}^2 & 0 \\ 0 & 0 & 0 \end{bmatrix}. \quad (7.16)$$

This matrix is not positive definite as it is of deficient rank, thus the input cannot be considered persistently exciting. However, the subsystem concerning roll and pitch torque may be considered. Let the regressor corresponding to roll and pitch dimensions be considered as

$$W'_1(\mathbf{0})\mathbf{k}_1(t_0)(W'_1(\mathbf{0})\mathbf{k}_1(t_0))^T = \begin{bmatrix} {}^B p_{y_c}^2 & -{}^B p_{y_c} {}^B p_{x_c} \\ -{}^B p_{x_c} {}^B p_{y_c} & {}^B p_{x_c}^2 \end{bmatrix}, \quad (7.17)$$

where $W'_1 \in \mathbb{R}^{2 \times 3} = m^* g \begin{bmatrix} 0 & c_\theta c_\phi & -c_\theta s_\phi \\ -c_\theta c_\phi & 0 & -s_\theta \end{bmatrix}$. This subsystem can be proven to be conditionally positive definite using the arbitrary vector $\mathbf{z} = [z_1 \quad z_2]^T$

$$\forall {}^B p_{x_c}, {}^B p_{y_c} > 0, {}^B p_{y_c} \neq {}^B p_{x_c}, \mathbf{z}^T \begin{bmatrix} {}^B p_{y_c}^2 & -{}^B p_{y_c} {}^B p_{x_c} \\ -{}^B p_{x_c} {}^B p_{y_c} & {}^B p_{x_c}^2 \end{bmatrix} \mathbf{z} = ({}^B p_{y_c} z_1 - {}^B p_{x_c} z_2)^2 > 0. \quad (7.18)$$

Evaluating the integral definition for persistent excitation in Eq. (7.14)

$$\int_s^{s+T} \mathbf{W}'_1(\mathbf{0}) \mathbf{k}_1(t) (\mathbf{W}'_1(\mathbf{0}) \mathbf{k}_1(t))^T dt = T \begin{bmatrix} {}^B p_{y_c}^2 & -{}^B p_{y_c} {}^B p_{x_c} \\ -{}^B p_{x_c} {}^B p_{y_c} & {}^B p_{x_c}^2 \end{bmatrix} \geq a \mathbf{I}_{2 \times 2} > 0, \quad (7.19)$$

for s sufficiently large, proves the input torque governing roll and pitch are persistently exciting as long as the center of mass coefficients are non-zero and not equal to each other. Running the simulation for described in Figure 6.11 using an adaptive control law as derived in this section with a known ${}^B \mathbf{P}_c^* = [0.1 \ 0.2 \ 0]^T$ and initial guess of ${}^B \mathbf{P}_c(0) = 0.5 {}^B \mathbf{P}_c^*$ with an adaptive gain $G = 0.1$ provided the estimate and error of estimate plots shown in Figure 7.7. In this test a simple hover in place command was given.

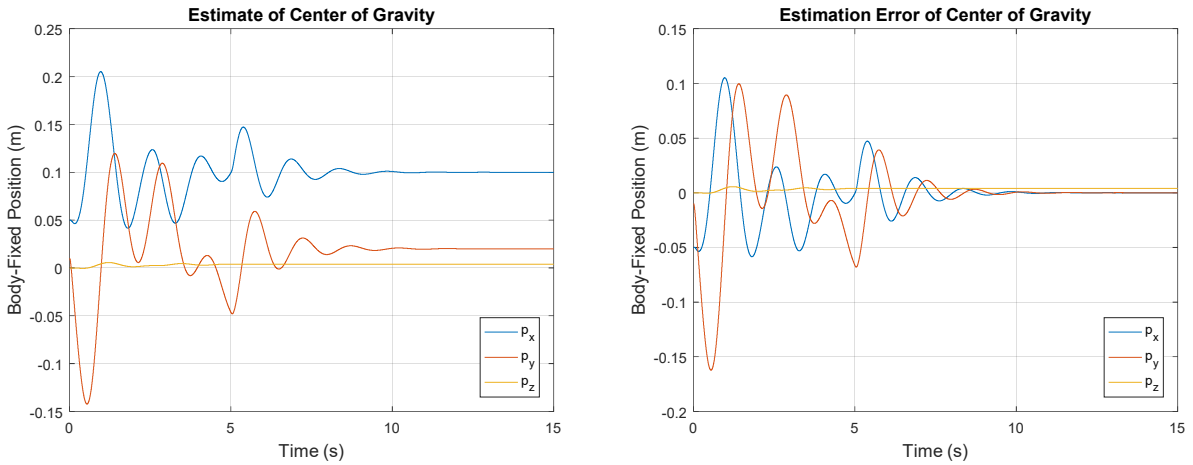


Figure 7.7. Center of mass estimation simulation.

As shown, the x and y estimates of center of gravity converge to 0. While there are a myriad of combinations of test conditions which demonstrate this, this set was chosen simply to verify the algorithm. Mathematically, the inertia tensor ${}^B J^*$ can also be considered for parameter estimation. The issue of convergence, however, prevents useful application of this, as all parameters are guaranteed only boundedness.

This estimator could be used to identify the mass properties of a point load grasped by the end effector of a manipulator, and stabilize the vehicle as the manipulator introduces disturbances. Clearly, if the joint positions are known, the location and center of mass of the UAV would be known. In combination with the total thrust produced, this adaptation could provide a more accurate assessment of payload mass. Careful consideration, however, should be considered as this analysis assumes static true value convergence. The algorithm should be performed in static hold only.

8 Conclusions

This work provided a unique design solution to the aerial manipulation problem through the development of a special class of fully-actuated hexrotor. Classification of the possible rotor rotation definitions led to the determination of two specific rotation models. These models uniquely identify the projection of planar and vertical thrust with only one design parameter for any given rotor. These definitions also maintained arbitrary rotor axis rotation, thus, their solution sets spanned that of any arbitrary non-parallel hexrotor model. These definitions provide a clear advantage over other Euler and quaternion definitions as those models require multiple design parameters to achieve the same result. Using one of the two identified rotation models, a unique solution to the design of a fully-actuated hexrotor was resolved.

The design metrics developed for the platform in this work provided a non-dimensional comparison of traditional multirotor and non-parallel hexrotor performance. It was shown that, while hover efficiency between a parallel and nonparallel multirotor model are related by c_β^2 , where β is the angle of projection of the rotors axis on the body fixed z-axis, roll and pitch torque could be compensated via form factor change. It was also found that the yaw produced by a nonparallel multirotor increases exponentially for larger β , and force production is heavily affected by the differential speed constraints of a hexrotor. Exploring the constraint spaces of other multirotor types suggested that an octocopter is the optimal airframe type for aerial manipulation as it possesses a uniform force speed constraint plane, and is already used heavily in commercial applications.

A backstepping controller was derived for use with the platform, and a novel approach for mass estimation was derived using Lyapunov principles. Because the UAV is fully-actuated, there is no need for direct coupling of multirotor attitude and manipulator dynamics. In this work, the manipulator effects were treated as external disturbances caused by base reactions from the manipulator mount. The Newton-Euler formalism was used to estimate wrench production to assist in attitude control. It was also shown that the

position of a platform's COM could be estimated accurately with an adaptive scheme, since a non-zero COG provides persistent excitation for the derived adaptive torque control law.

The developed multirotor firmware allows for both under-actuated and fully-actuated flight to be commanded through seamless mode transitions. Concerning dexterous flight, closed-loop control of the platform was performed and the results demonstrated decoupled position and orientation state control. With adequate firmware development, this platform can be used commercially. Since it can generate an arbitrary wrench, it is well-suited to aerial manipulation. By employing an airframe of the type developed in this work, the field of aerial manipulation may be expanded upon concerning multirotor implementation.

Appendix A: Kinematic Definitions

The kinematic definitions used to describe UAV flight utilize general Euler descriptors ϕ , θ , and ψ , which represent rigid body roll, pitch, and yaw, respectively. In this section, general rotation and Euler rates are discussed in terms of relative frame transformations. Vector and relative frame notation is consistent throughout this work, where a vector \mathbf{v} is assigned a single pre-superscript if the vector is measured with respect to its origin frame A , as $^A\mathbf{v}$, while that same vector measured with respect to another frame B is assigned a pre-superscript and post-subscript denoted $^B\mathbf{v}_A$.

A.1 Rotation

Euler notation describes rotations about cardinal axes X , Y , and Z in

$$R_x(\phi) = \begin{bmatrix} 1 & 0 & 0 \\ 0 & c_\phi & -s_\phi \\ 0 & s_\phi & c_\phi \end{bmatrix}, \quad (\text{A.1.1})$$

$$R_y(\theta) = \begin{bmatrix} c_\theta & 0 & s_\theta \\ 0 & 1 & 0 \\ -s_\theta & 0 & c_\theta \end{bmatrix}, \quad (\text{A.1.2})$$

$$R_z(\psi) = \begin{bmatrix} c_\psi & -s_\psi & 0 \\ s_\psi & c_\psi & 0 \\ 0 & 0 & 1 \end{bmatrix}, \quad (\text{A.1.3})$$

respectively. General rotation using Euler notation is described by

$$R_\Theta = R_z(\psi)R_y(\theta)R_x(\phi) = \begin{bmatrix} c_\psi c_\theta & c_\psi s_\theta s_\phi - s_\psi c_\phi & c_\psi s_\theta c_\phi + s_\psi s_\phi \\ s_\psi c_\theta & s_\psi s_\theta s_\phi + c_\psi c_\phi & s_\psi s_\theta c_\phi - c_\psi s_\phi \\ -s_\theta & c_\theta s_\phi & c_\theta c_\phi \end{bmatrix}. \quad (\text{A.1.4})$$

While sufficient for most UAV applications, quaternion rotation has also been utilized to control UAV [5].

Quaternion methods may take advantage of the general rotation matrix

$$R_k(\delta) = \begin{bmatrix} k_1 k_1 (1 - c_\delta) + c_\delta & k_2 k_1 (1 - c_\delta) - k_3 s_\delta & k_3 k_1 (1 - c_\delta) + k_2 s_\delta \\ k_1 k_2 (1 - c_\delta) + k_3 s_\delta & k_2 k_2 (1 - c_\delta) + c_\delta & k_3 k_2 (1 - c_\delta) - k_1 s_\delta \\ k_1 k_3 (1 - c_\delta) - k_2 s_\delta & k_2 k_3 (1 - c_\delta) + k_1 s_\delta & k_3 k_3 (1 - c_\delta) + c_\delta \end{bmatrix}, \quad (\text{A.1.5})$$

however, for regulated roll and pitch, this consideration is generally not necessary as gimbal lock is not a use-case issue.

A.2 Euler Rates

Euler Rates concerns the construction of the mapping between body fixed angular velocities and earth frame angular velocities. Velocities compound on previous axis rotation, thus a simple rotation is not sufficient for full definition. One Euler rate equation which defines Euler body-fixed angular velocity ${}^B\boldsymbol{\omega}$ in terms of inertial frame angular velocity ${}^E\boldsymbol{\omega}_B$ is

$${}^B\boldsymbol{\omega} = \begin{Bmatrix} \dot{\phi} \\ 0 \\ 0 \end{Bmatrix} + R_x^{-1}(\phi) \begin{Bmatrix} 0 \\ \dot{\theta} \\ 0 \end{Bmatrix} + R_x^{-1}(\phi) R_y^{-1}(\theta) \begin{Bmatrix} 0 \\ 0 \\ \dot{\psi} \end{Bmatrix}. \quad (\text{A.2.1})$$

Factoring inertial frame angular velocities from the right-hand side of Eq. (B.2.1) and inverting results the frame transformation T_Θ ,

$${}^E\boldsymbol{\omega}_B = \begin{bmatrix} 1 & 0 & s_\theta \\ 0 & c_\phi & -s_\phi c_\theta \\ 0 & s_\phi & c_\phi c_\theta \end{bmatrix}^{-1} {}^B\boldsymbol{\omega} = T_\Theta {}^B\boldsymbol{\omega}. \quad (\text{A.2.2})$$

For small angle deflections, this inversion is always possible. Since UAV will generally regulate roll and pitch, the matrix can be considered invertible in most use-cases, but the conditional invertibility should be noted when utilizing this transformation. The transformation from body-fixed angular velocity to inertial frame angular velocity is then

$$T_{\theta} = \begin{bmatrix} 1 & s_{\phi}t_{\theta} & -c_{\phi}t_{\theta} \\ 0 & c_{\phi} & s_{\phi} \\ 0 & -s_{\phi}/c_{\theta} & c_{\phi}/c_{\theta} \end{bmatrix}. \quad (\text{A.2.3})$$

Appendix B: Newton-Euler Dynamics

In this section frame transformations between body fixed and inertial frame force and torque definitions are derived for both Newton and Euler equations, and a special iterative algorithm called the Iterative Newton-Euler algorithm is discussed. As with Appendix A, a vector \mathbf{v} is assigned a single pre-superscript if the vector is measured with respect to its origin frame A , as ${}^A\mathbf{v}$, while that same vector measured with respect to another frame B is assigned a pre-superscript and post-subscript denoted ${}^B\mathbf{v}_A$.

B.1 Newton's Equation

Newton's equations describe the change in momentum with time of a body under applied external forces. For a rigid body, mass m is conserved, thus the sum of inertial frame forces ${}^E\mathbf{F}_B$ relate to inertial frame acceleration ${}^E\dot{\mathbf{V}}_B$ by

$${}^E\mathbf{F}_B = m{}^E\dot{\mathbf{V}}_B. \quad (\text{B.1.1})$$

Applying the Euler rotation matrix defined in Eq. (A.1.4), results

$${}^E\mathbf{F}_B = R_\Theta {}^B\mathbf{F} = m\widehat{R_\Theta} \dot{{}^B\mathbf{V}}. \quad (\text{B.1.2})$$

Since the rotation matrix is orthonormal, its inverse is its transpose, thus it holds that

$${}^B\mathbf{F} = mR_\Theta^T (R_\Theta {}^B\dot{\mathbf{V}} + \dot{R}_\Theta {}^B\mathbf{V}). \quad (\text{B.1.3})$$

Further simplification yields

$${}^B\mathbf{F} = m{}^B\dot{\mathbf{V}} + (R_\Theta^T \dot{R}_\Theta) m{}^B\mathbf{V}, \quad (\text{B.1.4})$$

To reduce the term $R_\Theta^T \dot{R}_\Theta$ in this formulation, the rotation matrix identity is introduced, where

$$R_{\Theta}^T R_{\Theta} = I_{3 \times 3}. \quad (\text{B.1.5})$$

deriving each side yields a useful transformation which proves the term to be skew-symmetric

$$\dot{R}_{\Theta}^T R_{\Theta} + R_{\Theta}^T \dot{R}_{\Theta} = \mathbf{0}_{3 \times 3}, \quad (\text{B.1.6})$$

$$R_{\Theta}^T \dot{R}_{\Theta} = -(R_{\Theta}^T \dot{R}_{\Theta})^T, \quad (\text{B.1.7})$$

[50] further shows that this quantity can be defined using body-fixed angular velocities in what is known as the S -operator $S({}^B \boldsymbol{\omega})$ in

$$S({}^B \boldsymbol{\omega}) = R_{\Theta}^T \dot{R}_{\Theta} = \begin{bmatrix} 0 & -r & q \\ r & 0 & -p \\ -q & p & 0 \end{bmatrix}. \quad (\text{B.1.8})$$

Substituting the S -operator in Eq. (B.1.4) results

$${}^B \mathbf{F} = m {}^B \dot{\mathbf{V}} + S({}^B \boldsymbol{\omega})(m {}^B \mathbf{V}). \quad (\text{B.1.9})$$

A useful property of the S -operator is its relation to the cross product. It can be shown that for any two vectors $\mathbf{Q}, \mathbf{Z} \in \mathbb{R}^3$ the following holds true

$$\forall \mathbf{Q}, \mathbf{Z} \in \mathbb{R}^3, S(\mathbf{Z})\mathbf{Q} = \mathbf{Z} \times \mathbf{Q}. \quad (\text{B.1.10})$$

Finally, body-fixed frame forces applied to a rigid body relate to body fixed angular velocity by

$${}^B \mathbf{F} = m {}^B \dot{\mathbf{V}} + {}^B \boldsymbol{\omega} \times (m {}^B \mathbf{V}). \quad (\text{B.1.11})$$

B.2 Euler's Equation

Euler's equation relates inertial frame applied torques ${}^E \boldsymbol{\tau}_B$ to inertial frame angular momentum ${}^E \mathbf{L}_B$ by

$${}^E\boldsymbol{\tau}_B = {}^E\dot{\mathbf{L}}_B. \quad (\text{B.2.1})$$

Applying the rotation matrix R_Θ to the Euler equations to transform all quantities in reference of the body-fixed frame B yields

$${}^E\boldsymbol{\tau}_B = R_\Theta {}^B\boldsymbol{\tau} = \widehat{R_\Theta} {}^B\mathbf{L}, \quad (\text{B.2.2})$$

$${}^B\boldsymbol{\tau} = R_\Theta^T (R_\Theta {}^B\dot{\mathbf{L}} + \dot{R}_\Theta {}^B\mathbf{L}). \quad (\text{B.2.3})$$

substituting angular momentum for angular velocity via the definition ${}^B\mathbf{L} = J^B\boldsymbol{\omega}$ yields

$${}^B\boldsymbol{\tau} = J^B\dot{\boldsymbol{\omega}} + (R_\Theta^T \dot{R}_\Theta) J^B\boldsymbol{\omega}. \quad (\text{B.2.4})$$

As with the Newton equation derivation the S -operator can be used to replace the rotation matrix term $R_\Theta^T \dot{R}_\Theta$ in Eq. (B.2.4) resulting

$${}^B\boldsymbol{\tau} = J^B\dot{\boldsymbol{\omega}} + S({}^B\boldsymbol{\omega})(J^B\boldsymbol{\omega}). \quad (\text{B.2.5})$$

Utilizing the property defined in Eq. (B.1.10) provides the torque definition in terms of the cross product

$${}^B\boldsymbol{\tau} = J^B\dot{\boldsymbol{\omega}} + {}^B\boldsymbol{\omega} \times (J^B\boldsymbol{\omega}). \quad (\text{B.2.6})$$

B.3 Iterative Newton-Euler Dynamic Formulation

The iterative Newton-Euler Dynamic Formulation is an efficient tool for online determination of serial manipulator dynamics. The method relies on consistent actuator and frame definitions using Denavit-Hartenberg form. In the formulation all prismatic and revolutive actuation is expressed along the i^{th} frame ${}^i\mathbf{Z}$ axis. The formulation discussed here was adapted from [39], for use in estimation of the aerial manipulator force torque expression.

For a serial manipulator, frame dynamics can be propagated iteratively along well-defined frame transformations ${}^i T_{i+1} \in \mathbb{R}^{4 \times 4}$, where the i^{th} frame is transformed to the $(i + 1)^{\text{th}}$ frame. In classic Denavit-Hartenberg notation, the parameters a_i and α_i are introduced to represent the distance and angle measured about the x-axis of the i^{th} frame ${}^i \mathbf{X}$ as the frame is transformed from the z-axis of the i^{th} considered frame ${}^i \mathbf{Z}$ to the z-axis of the newly transformed frame ${}^{i+1} \mathbf{Z}$, respectively. The parameters d_i and θ_i are introduced to represent the distance and angle measured along the z-axis of the i^{th} frame ${}^i \mathbf{Z}$ as the frame is transformed from the x-axis of the previously transformed frame ${}^{i-1} \mathbf{X}$ to the x-axis of the i^{th} frame ${}^i \mathbf{X}$, respectively. Link propagated frames can then be described as is depicted in Figure B.1 or more formally using x- and z- screw transforms.

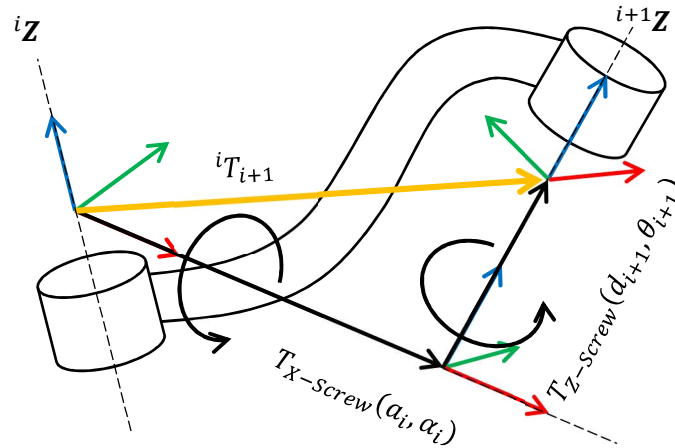


Figure B.1. Denavit-Hartenberg propagated link transformation

Screw transforms are transforms which describe a rotation and translation along and about a single axis. A general x-screw and z-screw transformation utilizing the defined Denavit-Hartenberg parameters a_i , α_i , d_{i+1} , and θ_{i+1} are defined in

$$T_{X-screw}(a_i, \alpha_i) = \begin{bmatrix} R_x(\alpha_i) & a_i \mathbf{X} \\ \mathbf{0}_{1 \times 3} & 1 \end{bmatrix} = \begin{bmatrix} 1 & 0 & 0 & a_i \\ 0 & c_{\alpha_i} & -s_{\alpha_i} & 0 \\ 0 & s_{\alpha_i} & c_{\alpha_i} & 0 \\ 0 & 0 & 0 & 1 \end{bmatrix}, \quad (\text{B.3.1})$$

$$T_{Z-screw}(d_{i+1}, \theta_{i+1}) = \begin{bmatrix} R_z(\theta_i) & d_i \mathbf{Z} \\ \mathbf{0}_{1 \times 3} & 1 \end{bmatrix} = \begin{bmatrix} c_{\theta_{i+1}} & -s_{\theta_{i+1}} & 0 & 0 \\ s_{\theta_{i+1}} & c_{\theta_{i+1}} & 0 & 0 \\ 0 & 0 & 1 & d_{i+1} \\ 0 & 0 & 0 & 1 \end{bmatrix}.$$

Combining the two screw transforms allows for the definition of serial manipulator frames using Denavit-Hartenberg notation, where

$${}^i T_{i+1} = T_{X-screw}(a_i, \alpha_i) T_{Z-screw}(d_{i+1}, \theta_{i+1}) = \begin{bmatrix} {}^i R_{i+1} & {}^i \mathbf{P}_{i+1} \\ \mathbf{0}_{1 \times 3} & 1 \end{bmatrix} = \begin{bmatrix} c_{\theta_{i+1}} & -s_{\theta_{i+1}} & 0 & a_i \\ c_{\alpha_i} s_{\theta_{i+1}} & c_{\alpha_i} c_{\theta_{i+1}} & -s_{\alpha_i} & -d_{i+1} s_{\alpha_i} \\ s_{\alpha_i} s_{\theta_{i+1}} & s_{\alpha_i} c_{\theta_{i+1}} & c_{\alpha_i} & d_{i+1} c_{\alpha_i} \\ 0 & 0 & 0 & 1 \end{bmatrix}. \quad (\text{B.3.2})$$

The rotation and displacement from i^{th} to $(i+1)^{th}$ link frame ${}^i R_{i+1}$ and ${}^i \mathbf{P}_{i+1}$ can be determined from the transform formulation for use in the iterative Newton-Euler algorithm as

$${}^i \mathbf{P}_{i+1} = \begin{bmatrix} a_i \\ -d_{i+1} s_{\alpha_i} \\ d_{i+1} c_{\alpha_i} \end{bmatrix}, \quad (\text{B.3.3})$$

$${}^i R_{i+1} = \begin{bmatrix} c_{\theta_{i+1}} & -s_{\theta_{i+1}} & 0 \\ c_{\alpha_i} s_{\theta_{i+1}} & c_{\alpha_i} c_{\theta_{i+1}} & -s_{\alpha_i} \\ s_{\alpha_i} s_{\theta_{i+1}} & s_{\alpha_i} c_{\theta_{i+1}} & c_{\alpha_i} \end{bmatrix}.$$

Aside from the designed Denavit-Hartenberg parameters, the algorithm requires the knowledge of several other parameters. It should be assumed that the base frame velocities are always known. This is reasonable for an aerial manipulator as these quantities would be shared by the body-fixed frame of the UAV to which the manipulator is mounted. Assuming a known 0^{th} frame angular velocity ${}^0 \boldsymbol{\omega}$, angular acceleration ${}^0 \dot{\boldsymbol{\omega}}$,

and linear acceleration ${}^0\dot{\mathbf{v}}$, dynamic propagation is possible for an aerial manipulator. It should be assumed that the link translation ${}^i\mathbf{P}_{i+1}$, translation from frame i to link center of mass C_i , ${}^{i+1}\mathbf{P}_{C(i+1)}$, i^{th} frame mass m_i , and i^{th} frame inertia J_i are known and static for all links in the serial manipulator. Actuator revolute angular displacement, velocity, and acceleration θ_i , $\dot{\theta}_i$, and $\ddot{\theta}_i$ about the i^{th} frame z-axis ${}^i\mathbf{Z}$ are assumed to be known for all actuators in this approach. Since servos are used in the design, each servo internally regulates position, and it is assumed that position can be tracked to a satisfactory degree such that these quantities can be approximated with low error. Without any means of direct force and torque feedback, this approach utilizes a direct dynamics approach. The propagated $(i + 1)^{th}$ frame angular velocity ${}^{i+1}\boldsymbol{\omega}$ was then defined to be

$${}^{i+1}\boldsymbol{\omega} = {}^iR_{i+1}{}^i\boldsymbol{\omega} + \dot{\theta}_{i+1}{}^{i+1}\mathbf{Z}, \quad (\text{B.3.4})$$

The linear and angular acceleration vectors for the $(i + 1)^{th}$ frame, ${}^{i+1}\dot{\mathbf{v}}$ and ${}^{i+1}\dot{\boldsymbol{\omega}}$ were defined using the known i^{th} link quantities

$${}^{i+1}\dot{\mathbf{v}} = {}^iR_{i+1}({}^i\dot{\boldsymbol{\omega}} \times {}^i\mathbf{P}_{i+1} + {}^i\boldsymbol{\omega} \times ({}^i\boldsymbol{\omega} \times {}^i\mathbf{P}_{i+1}) + {}^i\dot{\mathbf{v}}), \quad (\text{B.3.5})$$

$${}^{i+1}\dot{\boldsymbol{\omega}} = {}^iR_{i+1}{}^i\dot{\boldsymbol{\omega}} + ({}^iR_{i+1}{}^i\boldsymbol{\omega}) \times \dot{\theta}_{i+1}{}^{i+1}\mathbf{Z} + \ddot{\theta}_{i+1}{}^{i+1}\mathbf{Z}.$$

While the motion of all frames is necessary to compute manipulator kinematics, the acceleration of the center of mass is necessary for dynamic consideration of forces and torques. To calculate these accelerations, the center of mass translation vector ${}^{i+1}\mathbf{P}_{C(i+1)}$ was utilized in defining the acceleration of each link's center of mass ${}^{i+1}\dot{\mathbf{v}}_{C(i+1)}$

$${}^{i+1}\dot{\mathbf{v}}_{C(i+1)} = {}^{i+1}\dot{\boldsymbol{\omega}} \times {}^{i+1}\mathbf{P}_{C(i+1)} + {}^{i+1}\boldsymbol{\omega} \times ({}^{i+1}\boldsymbol{\omega} \times {}^{i+1}\mathbf{P}_{C(i+1)}) + {}^{i+1}\dot{\mathbf{v}}. \quad (\text{B.3.6})$$

Lastly, each link is prescribed a body-fixed force and torque ${}^{i+1}\mathbf{F}$ and ${}^{i+1}\mathbf{N}$ defined in

$$\begin{aligned}
{}^{i+1}\mathbf{F} &= m_{i+1} {}^{i+1}\dot{\mathbf{v}}_{C(i+1)}, \\
{}^{i+1}\mathbf{N} &= J_{i+1} {}^{i+1}\dot{\boldsymbol{\omega}} + {}^{i+1}\boldsymbol{\omega} \times (J_{i+1} {}^{i+1}\boldsymbol{\omega}).
\end{aligned}
\tag{B.3.7}$$

These quantities represent each link's internal force and torque expression, and define the Iterative Newton-Euler algorithms outward propagation steps. For n frames which define a serial manipulator in an aerial manipulator system, the manipulator dynamic propagation is useful for estimating the 0^{th} frame forces and torques which can be interpreted as disturbances applied to the UAV body-fixed frame. The n^{th} frame corresponds to the system's end-effector, and allow for force and torque propagation of all environment interactions between the manipulator and some foreign body. The Iterative Newton-Euler algorithm's inward steps are described by the joint force ${}^i\mathbf{f}$ and torque ${}^i\mathbf{n}$

$$\begin{aligned}
{}^i\mathbf{f} &= {}^iR_{i+1}^T {}^{i+1}\mathbf{f}_{i+1} + {}^i\mathbf{F}, \\
{}^i\mathbf{n} &= {}^i\mathbf{N} + {}^iR_{i+1}^T {}^{i+1}\mathbf{n}_{i+1} + {}^i\mathbf{P}_{C_i} \times {}^i\mathbf{F} + {}^i\mathbf{P}_{i+1} \times ({}^iR_{i+1}^T {}^{i+1}\mathbf{f}_{i+1}).
\end{aligned}
\tag{B.3.8}$$

Using this algorithm, an external end-effector force and torque ${}^n\mathbf{f}$ and ${}^n\mathbf{n}$ can be propagated to the base frame force and torque ${}^0\mathbf{f}$ and ${}^0\mathbf{n}$.

Appendix C: Backstepping in \mathbb{R}^n

Backstepping is a technique by which a virtual input is used to affect higher order dynamics via careful manipulation of lower order states. For an underactuated system, this technique may be used to ensure stability in the sense of Lyapunov. In this section 2nd order and 3rd order backstepping schema are introduced pertaining to the construction of proper virtual inputs as a function of state error.

C.1 Backstepping 2nd Order

Let some error of state $\mathbf{e}_1 \in \mathbb{R}^n$ be composed of some state vector $\mathbf{x} \in \mathbb{R}^n$ and desired state $\mathbf{x}_d \in \mathbb{R}^n$ such that $\mathbf{e}_1 = \mathbf{x}_d - \mathbf{x}$. To drive $\mathbf{e}_1 \rightarrow \mathbf{0}$ as time $t \rightarrow \infty$, a positive definite Lyapunov function V_1 is first introduced

$$V_1 = \frac{1}{2} \mathbf{e}_1^T \mathbf{e}_1 > 0. \quad (\text{C.1.1})$$

If it can be shown that \dot{V}_1 is negative definite, then the system is said to be locally asymptotically stable.

Deriving the Lyapunov function V_1 provides

$$\dot{V}_1 = \mathbf{e}_1^T \dot{\mathbf{e}}_1 = \mathbf{e}_1^T (\dot{\mathbf{x}}_d - \dot{\mathbf{x}}). \quad (\text{C.1.2})$$

The method of backstepping involves the forcing of the derivative of state to some virtual control \mathbf{v}_1 . That is, if the system is controllable such that the derivative of state $\dot{\mathbf{x}} \rightarrow \mathbf{v}_1$, where

$$\mathbf{v}_1 = \dot{\mathbf{x}}_d + Q_1 \mathbf{e}_1, \quad (\text{C.1.3})$$

and $Q_1 > 0$ is some square positive definite gain matrix, then the derivative of the Lyapunov function becomes negative definite

$$\dot{V}_1 = -\mathbf{e}_1^T Q_1 \mathbf{e}_1 < 0. \quad (\text{C.1.4})$$

If the system were controllable as such then the system would be stable, however, most mechanical and electrical systems are of 2nd order, thus the driving principle in the shaping of $\dot{\mathbf{x}} \rightarrow \mathbf{v}_1$ is not guaranteed and the system is not stable. Thus, a second error term $\mathbf{e}_2 = \mathbf{v}_1 - \dot{\mathbf{x}}$ may be introduced, which quantifies the error of the 1st order derivative of state with respect to the virtual control \mathbf{v}_1 . One Lyapunov candidate V_2 of order 2nd is then

$$V_2 = \frac{1}{2} \mathbf{e}_1^T \mathbf{e}_1 + \frac{1}{2} \mathbf{e}_2^T \mathbf{e}_2 > 0, \quad (\text{C.1.5})$$

Taking the derivative of the Lyapunov candidate V_2 returns

$$\dot{V}_2 = \mathbf{e}_1^T \dot{\mathbf{e}}_1 + \mathbf{e}_2^T \dot{\mathbf{e}}_2 = \mathbf{e}_1^T (\dot{\mathbf{x}}_d - \dot{\mathbf{x}}) + \mathbf{e}_2^T (\mathbf{v}_1 - \ddot{\mathbf{x}}). \quad (\text{C.1.6})$$

By substituting the derivative of state terms with the appropriate definitions, the system may be reduced to the form

$$\dot{V}_2 = -\mathbf{e}_1^T Q_1 \mathbf{e}_1 + \mathbf{e}_1^T \mathbf{e}_2 + \mathbf{e}_2^T (\ddot{\mathbf{x}}_d - Q_1 Q_1 \mathbf{e}_1 + Q_1 \mathbf{e}_2 - \ddot{\mathbf{x}}). \quad (\text{C.1.7})$$

A second virtual input is then generated to ensure $\dot{V}_2 < 0$. By assuming a control input which can shape the second order dynamics such that $\ddot{\mathbf{x}} \rightarrow \mathbf{v}_2$, where

$$\mathbf{v}_2 = \ddot{\mathbf{x}}_d + (I - Q_1 Q_1) \mathbf{e}_1 + (Q_1 + Q_2) \mathbf{e}_2, \quad (\text{C.1.8})$$

and $Q_2 > 0$ is a square positive definite gain matrix, local asymptotic stability may be guaranteed.

Substitution into the derivative of V_2 proves this explicitly, where

$$\dot{V}_2 = -\mathbf{e}_1^T Q_1 \mathbf{e}_1 - \mathbf{e}_2^T Q_2 \mathbf{e}_2 < 0. \quad (\text{C.1.9})$$

While this is a reasonable approach to driving 2nd order dynamics to some reference signal, it is often easier to utilize these control forms using only the state error, not the mixed error terms \mathbf{e}_1 and \mathbf{e}_2 . The state error and derivative of state error were denoted $\tilde{\mathbf{x}}$ and $\dot{\tilde{\mathbf{x}}}$, respectively in the formulation

$$\begin{aligned}\tilde{\mathbf{x}} &= \mathbf{x}_d - \mathbf{x} = \mathbf{e}_1, \\ \dot{\tilde{\mathbf{x}}} &= \dot{\mathbf{x}}_d - \dot{\mathbf{x}} = \mathbf{e}_2 - Q_1 \mathbf{e}_1.\end{aligned}\tag{C.1.10}$$

The state error terms can then be rewritten as

$$\begin{aligned}\mathbf{e}_1 &= \tilde{\mathbf{x}}, \\ \mathbf{e}_2 &= \dot{\tilde{\mathbf{x}}} + Q_1 \tilde{\mathbf{x}},\end{aligned}\tag{C.1.11}$$

and substituted into the 2nd order general virtual input

$$\mathbf{v}_2 = \ddot{\mathbf{x}}_d + (Q_1 + Q_2)\dot{\tilde{\mathbf{x}}} + (I + Q_2 Q_1)\tilde{\mathbf{x}}.\tag{C.1.12}$$

This formulation is useful for the development of stable error dynamics. For a second order system with arbitrary wrench control, for example, the acceleration of the system is directly affected by the control signal, thus, there is a means to affect $\ddot{\mathbf{x}} \rightarrow \mathbf{v}_2$.

C.2 Extension to 3rd Order and Integration of Error

While 2nd order backstepping is useful for determination of stable error dynamics, there is no direct integral term in the formulation. This type of control is effectively a PD controller. Any inconsistencies in the measured and expressed states will result some running sum error. To that end, 3rd order backstepping may be used. First an error term is created to relate the 2nd order virtual input to acceleration dynamics $\mathbf{e}_3 = \mathbf{v}_2 - \ddot{\mathbf{x}}$. A 2rd order Lyapunov candidate is then

$$V_3 = \frac{1}{2} \mathbf{e}_1^T \mathbf{e}_1 + \frac{1}{2} \mathbf{e}_2^T \mathbf{e}_2 + \frac{1}{2} \mathbf{e}_3^T \mathbf{e}_3 > 0. \quad (\text{C.2.1})$$

Taking the derivative \dot{V}_3 results the system

$$\dot{V}_3 = \mathbf{e}_1^T \dot{\mathbf{e}}_1 + \mathbf{e}_2^T \dot{\mathbf{e}}_2 + \mathbf{e}_3^T \dot{\mathbf{e}}_3 = \mathbf{e}_1^T (\dot{\mathbf{x}}_d - \dot{\mathbf{x}}) + \mathbf{e}_2^T (\dot{\mathbf{v}}_1 - \dot{\mathbf{x}}) + \mathbf{e}_3^T (\dot{\mathbf{v}}_2 - \ddot{\mathbf{x}}). \quad (\text{C.2.2})$$

Reducing the derivative of the Lyapunov candidate yields

$$\begin{aligned} \dot{V}_3 = & -\mathbf{e}_1^T Q_1 \mathbf{e}_1 - \mathbf{e}_2^T Q_2 \mathbf{e}_2 + \mathbf{e}_2^T \mathbf{e}_3 + \mathbf{e}_3^T ((\ddot{\mathbf{x}}_d + (-2Q_1 - Q_2 + Q_1 Q_1 Q_1) \mathbf{e}_1 + (I - \\ & Q_1 Q_1 - Q_1 Q_2 - Q_2 Q_2) \mathbf{e}_2 + (Q_1 + Q_2) \mathbf{e}_3) - \ddot{\mathbf{x}}). \end{aligned} \quad (\text{C.2.3})$$

To facilitated backstepping, a virtual input \mathbf{v}_3 is introduced where $\ddot{\mathbf{x}} \rightarrow \mathbf{v}_3$ implies stable dynamics, where

$$\begin{aligned} \mathbf{v}_3 = & \ddot{\mathbf{x}}_d + (-2Q_1 - Q_2 + Q_1 Q_1 Q_1) \mathbf{e}_1 + (2I - Q_1 Q_1 - Q_1 Q_2 - Q_2 Q_2) \mathbf{e}_2 + (Q_1 + \\ & Q_2 + Q_3) \mathbf{e}_3, \end{aligned} \quad (\text{C.2.4})$$

and $Q_3 > 0$ is some square positive definite gain matrix. The Lyapunov candidate derivative was then calculated to be

$$\dot{V}_3 = -\mathbf{e}_1^T Q_1 \mathbf{e}_1 - \mathbf{e}_2^T Q_2 \mathbf{e}_2 - \mathbf{e}_3^T Q_3 \mathbf{e}_3 < 0. \quad (\text{C.2.5})$$

Lastly, the form of the virtual control is rewritten in terms of pure error dynamics, where the acceleration error was determined to be $\ddot{\tilde{\mathbf{x}}}$ in the formulation

$$\ddot{\tilde{\mathbf{x}}} = \ddot{\mathbf{x}}_d - \ddot{\mathbf{x}} = -(I - Q_1 Q_1) \mathbf{e}_1 - (Q_1 + Q_2) \mathbf{e}_2 + \mathbf{e}_3. \quad (\text{C.2.6})$$

The 3rd order error term can then be rewritten as

$$\mathbf{e}_3 = \ddot{\tilde{\mathbf{x}}} + (I + Q_2 Q_1) \dot{\tilde{\mathbf{x}}} + (Q_1 + Q_2) \tilde{\mathbf{x}}, \quad (\text{C.2.7})$$

and the 3rd order virtual input can be written as

$$\mathbf{v}_3 = \ddot{\mathbf{x}}_d + (Q_1 + Q_2 + Q_3)\ddot{\tilde{\mathbf{x}}} + (2I + Q_2Q_1 + Q_3Q_1 + Q_3Q_2)\dot{\tilde{\mathbf{x}}} + (Q_1 + Q_3 + Q_3Q_2Q_1)\tilde{\mathbf{x}}. \quad (\text{C.2.8})$$

Taken as expressed in a general mechanical system, one may be tempted to interpret this controller as a high order virtual control of jerk. While possible, it is generally impractical due to the need for accurate acceleration error readings. By considering a reduced order state, however, may facilitate a new definition of 2nd order virtual control. Let a new state $\mathbf{z} \in \mathbb{R}^n$ and desired state $\mathbf{z}_d \in \mathbb{R}^n$ be defined as $\dot{\mathbf{z}} = \mathbf{x}$ and as $\dot{\mathbf{z}}_d = \mathbf{x}_d$, respectively. Applying 3rd order backstepping for $\tilde{\mathbf{z}} = \mathbf{z}_d - \mathbf{z}$ results

$$\mathbf{v}'_3 = \ddot{\mathbf{z}}_d + (Q_1 + Q_2 + Q_3)\ddot{\tilde{\mathbf{z}}} + (2I + Q_2Q_1 + Q_3Q_1 + Q_3Q_2)\dot{\tilde{\mathbf{z}}} + (Q_1 + Q_3 + Q_3Q_2Q_1)\tilde{\mathbf{z}}. \quad (\text{C.2.9})$$

This schema is essentially a 2nd order controller which ensures local asymptotic stability, where integral error is utilized. The final form of the augmented 2nd order backstepping controller \mathbf{v}'_3 is

$$\mathbf{v}'_3 = \ddot{\mathbf{x}}_d + (Q_1 + Q_2 + Q_3)\dot{\tilde{\mathbf{x}}} + (2I + Q_2Q_1 + Q_3Q_1 + Q_3Q_2)\tilde{\mathbf{x}} + (Q_1 + Q_3 + Q_3Q_2Q_1) \int_0^t \tilde{\mathbf{x}} dt. \quad (\text{C.2.10})$$

Bibliography

- [1] T. Hamel, R. Mahony, R. Lozano, and J. Ostrowski, *Dynamic modelling and configuration stabilization for an X4-flyer*, vol. 15, no. 1. IFAC, 2002.
- [2] P. Pounds, R. Mahony, P. Hynes, and J. Roberts, “Design of a four-rotor aerial robot,” in *Australasian Conference on Robotics and Automation*, 2002, no. November, pp. 145–150.
- [3] S. Bouabdallah and R. Siegwart, “Backstepping and Sliding-mode Techniques Applied to an Indoor Micro Quadrotor,” in *Proceedings - IEEE International Conference on Robotics and Automation*, 2005, no. April, pp. 47–52.
- [4] S. Bouabdallah, “Design and Control of Quadrotors With Application To Autonomous Flying,” *Techniques*, vol. 3727, no. 3727, p. 61, 2007.
- [5] E. Fresk and G. Nikolakopoulos, “Full Quaternion Based Attitude Control for a Quadrotor,” *Eur. Control Conf.*, pp. 3864–3869, 2013.
- [6] P. Bristeau, P. Martin, E. Salaün, and N. Petit, “The role of propeller aerodynamics in the model of a quadrotor UAV,” *Eur. Control Conf. Proc.*, no. November, pp. 683–688, 2009.
- [7] G. J. J. Ducard and M.-D. Hua, “DISCUSSION AND PRACTICAL ASPECTS ON CONTROL ALLOCATION FOR A MULTI-ROTOR HELICOPTER,” *ISPRS - International Archives of the Photogrammetry, Remote Sensing and Spatial Information Sciences*, vol. XXXVIII-1/. Sophia Antipolis, pp. 95–100, 2012.
- [8] P. Moore, “The Moore-Penrose Pseudoinverse,” vol. 1, no. 1, pp. 1–5, 1972.
- [9] K. S. Pratt, R. R. Murphy, and J. L. Burke, “Use of Tethered Small Unmanned Aerial System at Berkman Plaza II Collapse (iecAR) Unmanned Asearchia SytheWiremU S) urv byd GRiche work

- prsten (Ave through thoroughnumru,” no. October, 2008.
- [10] F. Muttin, “Umbilical deployment modeling for tethered UAV detecting oil pollution from ship,” *Appl. Ocean Res.*, vol. 33, no. 4, pp. 332–343, Oct. 2011.
- [11] M. W. Mueller and R. D’Andrea, “Stability and control of a quadrocopter despite the complete loss of one, two, or three propellers,” in *Proceedings - IEEE International Conference on Robotics and Automation*, 2014, pp. 45–52.
- [12] N. Michael *et al.*, “Collaborative Mapping of an Earthquake-Damaged Building via Ground and Aerial Robots,” *J. F. Robot.*, vol. 29, no. 5, pp. 832–841, 2012.
- [13] M. Bisgaard, A. la Cour-Harbo, and J. Dimon Bendtsen, “Adaptive control system for autonomous helicopter slung load operations,” *Control Eng. Pract.*, vol. 18, no. 7, pp. 800–811, 2010.
- [14] I. Palunko, R. Fierro, and P. Cruz, “Trajectory generation for swing-free maneuvers of a quadrotor with suspended payload: A dynamic programming approach,” *Robot. Autom. (ICRA)*, ..., 2012.
- [15] G. Antonelli, E. Cataldi, P. R. Giordano, S. Chiaverini, and A. Franchi, “Experimental validation of a new adaptive control scheme for quadrotors MAVs,” *2013 IEEE/RSJ Int. Conf. Intell. Robot. Syst.*, pp. 2439–2444, 2013.
- [16] A. Chovancová, T. Fico, E. Chovanec, and P. Hubinsk, “Mathematical Modelling and Parameter Identification of Quadrotor (a survey),” *Procedia Eng.*, vol. 96, pp. 172–181, 2014.
- [17] A. Albers, S. Trautmann, T. Howard, T. A. Nguyen, M. Frietsch, and C. Sauter, “Semi-autonomous flying robot for physical interaction with environment,” *2010 IEEE Conf. Robot. Autom. Mechatronics, RAM 2010*, pp. 441–446, 2010.
- [18] V. Ghadiok, J. Goldin, and W. Ren, “Autonomous indoor aerial gripping using a quadrotor,” *IEEE*

- Int. Conf. Intell. Robot. Syst.*, pp. 4645–4651, 2011.
- [19] P. E. I. Pounds, D. R. Bersak, and A. M. Dollar, “Grasping from the air: Hovering capture and load stability,” *Proc. - IEEE Int. Conf. Robot. Autom.*, pp. 2491–2498, 2011.
- [20] P. E. I. Pounds, D. R. Bersak, and A. M. Dollar, “Practical aerial grasping of unstructured objects,” *Technol. Pract. Robot Appl. (TePRA), 2011 IEEE Conf.*, pp. 99–104, 2011.
- [21] C. M. Korpela, T. W. Danko, and P. Y. Oh, “MM-UAV: Mobile manipulating unmanned aerial vehicle,” *J. Intell. Robot. Syst. Theory Appl.*, vol. 65, pp. 93–101, 2012.
- [22] C. Korpela, M. Orsag, M. Pekala, and P. Oh, “Dynamic stability of a mobile manipulating unmanned aerial vehicle,” *2013 IEEE Int. Conf. Robot. Autom.*, pp. 4922–4927, May 2013.
- [23] C. Korpela, M. Orsag, Y. Jun, P. Brahmbhatt, and P. Oh, “A hardware-in-the-loop test rig for aerial manipulation,” in *2013 International Conference on Unmanned Aircraft Systems, ICUAS 2013 - Conference Proceedings*, 2013, pp. 982–987.
- [24] J. L. J. Scholten, M. Fumagalli, S. Stramigioli, and R. Carloni, “Interaction control of an UAV endowed with a manipulator,” in *IEEE International Conference on Robotics and Automation*, 2013, pp. 4910–4915.
- [25] A. E. Jimenez-Cano, J. Martin, G. Heredia, A. Ollero, and R. Cano, “Control of an aerial robot with multi-link arm for assembly tasks,” *Proc. - IEEE Int. Conf. Robot. Autom.*, pp. 4916–4921, 2013.
- [26] F. Huber *et al.*, “First analysis and experiments in aerial manipulation using fully actuated redundant robot arm,” in *IEEE International Conference on Intelligent Robots and Systems*, 2013, pp. 3452–3457.
- [27] S. Kim, S. Choi, and H. J. Kim, “Aerial manipulation using a quadrotor with a two DOF robotic

- arm,” *IEEE Int. Conf. Intell. Robot. Syst.*, pp. 4990–4995, 2013.
- [28] M. Orsag, C. Korpela, S. Bogdan, and P. Oh, “Lyapunov based model reference adaptive control for aerial manipulation,” in *2013 International Conference on Unmanned Aircraft Systems (ICUAS)*, 2013, pp. 966–973.
- [29] S. Driessens and P. Pounds, “The Triangular Quadrotor: A More Efficient Quadrotor Configuration,” *IEEE Trans. Robot.*, vol. 31, no. 6, pp. 1517–1526, 2015.
- [30] C. Papachristos, K. Alexis, and A. Tzes, “Efficient force exertion for aerial robotic manipulation: Exploiting the thrust-vectoring authority of a tri-tiltrotor UAV,” in *Proceedings - IEEE International Conference on Robotics and Automation*, 2014.
- [31] M. Ramp and E. Papadopoulos, “On modeling and control of a holonomic vectoring tri-copter,” in *IEEE International Conference on Intelligent Robots and Systems*, 2015, vol. 2015–Decem.
- [32] D. Langkamp *et al.*, “An engineering development of a novel hexrotor vehicle for 3D applications,” in *Proc. the International Micro Air Vehicles conference*, 2011.
- [33] G. Jiang and R. Voyles, “A nonparallel hexrotor UAV with faster response to disturbances for precision position keeping,” in *the Proc. of the 12th IEEE International Symposium on Safety, Security and Rescue Robotics*, 2014.
- [34] A. Nikou, G. C. Gavridis, and K. J. Kyriakopoulos, “Mechanical Design, Modelling and Control of a Novel Aerial Manipulator.” pp. 1–8, 2015.
- [35] S. Park, J. Her, J. Kim, and D. Lee, “Design, modeling and control of omni-directional aerial robot,” in *IEEE International Conference on Intelligent Robots and Systems*, 2016, vol. 2016–Novem.
- [36] S. Rajappa, M. Ryll, H. H. Bulthoff, and A. Franchi, “Modeling , Control and Design Optimization

- for a Fully-actuated Hexarotor Aerial Vehicle with Tilted Propellers,” in *International Conference on Robotics and Automation*, 2015, pp. 4006–4013.
- [37] D. Kotarski and M. Engineering, “Mathematical Modelling of Multirotor UAV,” *Int. J. Theor. Appl. Mech.*, vol. 1, pp. 233–238, 2016.
- [38] M. Ryll, D. Bicego, and A. Franchi, “Modeling and Control of FAST-Hex : a Fully – Actuated by Synchronized – Tilting Hexarotor,” *Proc. IEEE/RSJ Int’l Conf. Intell. Robot. Syst.*, pp. 1689–1694, 2016.
- [39] J. J. Craig, *Introduction to Robotics: Mechanics and Control 3rd Edition*, vol. 1, no. 3. 2004.
- [40] T. Bresciani, “Modelling , Identification and Control of a Quadrotor Helicopter,” Lund University, 2008.
- [41] G. Matič, M. Topič, and M. Jankovec, “Mathematical Model of a Monocopter Based on Unsteady Blade-Element Momentum Theory,” *J. Aircr.*, vol. 52, no. 6, pp. 1905–1913, 2015.
- [42] H. Lee *et al.*, “Design Optimization, Modeling and Control of Unmanned Aerial Vehicle Lifted By Coandă Effect,” *IEEE/ASME Trans. Mechatronics*, vol. 4435, no. c, pp. 1–1, 2017.
- [43] “DJI Store.” [Online]. Available: https://store.dji.com/?gclid=EAIaIQobChMIna2FipWV2QIVF5d-Ch13sghWEAAYASAAEgJsVPD_BwE.
- [44] “MAVLink Micro Air Vehicle Protocol.” [Online]. Available: <https://github.com/mavlink>.
- [45] “Mathworks Matlab.” [Online]. Available: <https://www.mathworks.com/products/matlab.html>.
- [46] “Coppelia Robotics.” [Online]. Available: <http://www.coppeliarobotics.com/index.html>.

- [47] L. Nogueira, “Comparative Analysis Between Gazebo and V-REP Robotic Simulators,” p. 5, 2014.
- [48] J. M. O’Kane, *A Gentle Introduction to ROS*, 2.0.3. Columbia: O’Kane, Jason M., 2014.
- [49] I. M. Y. Mareels and M. Gevers, “Persistency of excitation criteria for linear, multivariable, time-varying systems,” *Math. Control. Signals, Syst.*, vol. 1, no. 3, pp. 203–226, 1988.
- [50] A. A. Shabana, *Computational Dynamics*, 3rd ed. Wiley, 2010.

Curriculum Vitae

Jameson Yau Sung Lee
4505 S. Maryland
Department of Mechanical Engineering
University of Nevada, Las Vegas
Las Vegas, NV, 89154
jameson.lee@unlv.edu

Education:

Ph.D. – University of Nevada, Las Vegas, Las Vegas, NV, USA Jan. 2014 – May 2018

- Doctor of Philosophy (Ph.D.) in Mechanical Engineering
- Advisor: Woosoon Yim, Ph.D.
- Major Focus: Dynamics and Control
- Minor Focus: Solid Mechanics and Mechanical Design
- Research Areas: Robotics, UAV, UGV, Aerial Manipulation

B.S. – University of Nevada, Las Vegas, Las Vegas, NV, USA Aug. 2008 – Dec. 2013

- Bachelor of Science (B.S.) in Mechanical Engineering
- Minor: Mathematical Sciences
- Graduated Magna Cum Laude
- Cumulative G.P.A: 3.8/4.00

Research Experience:

Intelligent Structures and Control Laboratory (ISCL) Dec. 2014 – Present

- University of Nevada, Las Vegas – Las Vegas, NV, USA
- Research Assistant, Department of Mechanical Engineering
- Supervisor/Advisor: Woosoon Yim, Ph.D.
- Research Topic: Design optimization and control of a fully actuated hexrotor UAV for use in aerial manipulation applications. Adaptive controller design.

Intelligent Robotics and Mechatronic System (IRMS) Laboratory Jun. 2016 – Aug. 2016

- Sungkyunkwan University (SKKU) – Suwon, Republic of Korea
- Visiting Scholar, Department of Mechanical Engineering
- Supervisor/Advisor: Hyouk Ryeol Choi, Ph.D.
- Research Topic: Modeling and control of a saucer type Coandă effect UAV. Autonomous navigation of a Coandă drone towards participation in the 2016 IROS Autonomous Drone Race Challenge.

Professional Experience:

Instructor: Dynamics of Machine

Jan. 2017 – May 2018

- University of Nevada, Las Vegas – Las Vegas, NV, USA
- Department of Mechanical Engineering, Class Des. ME320-1002
- Catalog Description: In this class, topics covered include the algebraic and graphical methods for synthesis of cam, gear, and linkage, mechanisms, methods of planar motion analysis, characteristics of plane motion, and kinematics.

Teaching Assistant: Automatic Control Laboratory

Aug. 2017 – Dec. 2017

- University of Nevada, Las Vegas – Las Vegas, NV, USA
- Department of Mechanical Engineering, Class Des. ME421L-1003&1004
- Catalog Description: Control system identification. Controller design, experimentation, computer simulation, and analysis of position and speed control systems. Control system performance optimization.

Mathematics, Physics, and Engineering Mentor

Aug. 2011 – Dec. 2013

- University of Nevada Las Vegas – Las Vegas, NV, USA
- Academic Success Center
- Description: Tutored all undergraduate levels of mathematics, physics, and mechanical engineering courses offered at UNLV. Mentored new tutors and developed educational workshops related to specific engineering topics.

National Science Foundation (NSF), Partnerships for International Research and Education (PIRE) 2017 Fellow

Aug. 2017

- Sungkyunkwan University (SKKU) – Suwon, Republic of Korea
- Korea Institute of Science and Technology (KIST) – Seoul, Republic of Korea
- National Institute of Advanced Science and Technology (AIST) – Osaka, Japan
- Simulation of a Coandă Blimp within V-Rep
- Workshops presentation on a fully-actuated hexrotor design
- Workshop attendance on active materials modelling and processing methods

National Science Foundation (NSF), East Asia and Pacific Summer Institutes (EAPSI) 2016 Fellow

Jun. 2016 – Aug. 2016

- National Science Foundation (NSF) – Arlington, VA, USA
- Pre-Departure Orientation
- Sungkyunkwan University (SKKU) – Suwon, Republic of Korea
- Visiting Scholar in the Intelligent Robotics and Mechatronics (IRMS) Laboratory towards publication in ICRA 2017 and

participation in the IROS 2016 Autonomous Drone Race Challenge
in Daejeon, Republic of Korea

Oak Ridge National Laboratory (ORNL), Power Electronics and Electric Machinery Research Center Intern Jun. 2015 – Aug. 2015

- Oak Ridge, TN, USA
- Supervisors: Burak Ozpineci, Ph.D. and Madhu Chinthavali, Ph.D.
- Research Topic: Development of a magnetic resonant wireless power transfer system for mid-air charging of UAS

NV Energy Transmission and Generation Intern II Senior May 2013 – Nov. 2013

- Las Vegas, NV, USA
- Description: AutoCAD and Inventor CAD drawings for the rebuild of a 69kV substation. Prepared recommendations and justifications for various FM Global projects. Interacted with contractors and scheduled their site inspections.

Las Vegas Convention and Visitors Authority Engineering Intern May 2012 – Aug. 2012

- Las Vegas, NV, USA
- Description: Shadowed project managers, HVAC technicians, and electricians. OSHA Forklift Operation & Safety Training. Assembled bay lighting fixtures for the refurbishment of convention space.

Publications:

Jameson YS Lee, Kam K Leang, Woosoon Yim, “Modular design and control of a fully-actuated hexrotor for aerial manipulation applications”, ASME Journal of Mechanisms and Robotics, Paper Number: JMR-17-1361

J. Y. Lee, S. H. Song, H. W. Shon, H. R. Choi, W. Yim, “Modeling and Control of a Saucer Type Coandă Effect UAV”, in *Proceedings of the IEEE International Conference on Robotics and Automation 2017*, Republic of Singapore, May 2017. DOI: 10.1109/ICRA.2017.7989316

J. Y. Lee, Z. Cook, A. Barzilov, W. Yim, “Control of an Aerial Manipulator with an On-Board Balancing Mechanism”, in *Proceedings of the ASME 2016 International Mechanical Engineering Congress and Exposition*, Phoenix, AZ, USA, Nov. 2016. DOI: 10.1115/IMECE2016-66976

Z. Cook, J. Y. Lee, J. Hartman, W. Yim, A. Barzilov, “Contour Mapping Based Radiation Source Localization by UAS Swarm”, in *Proceedings of the 2016 ANS Winter Meeting and Technology Expo*, Las Vegas, NV, USA, Nov. 2016

J. Y. Lee, J. Hartman, Z. Cook, J. S. Lee, W. S. Yim, A. Barzilov, “Development of Plug – and – Play Interchangeable Components for Unmanned Aerial System with Mobile Manipulation Capability”, in *Proceedings of the 2016 ANS Winter Meeting and Technology Expo*, Las Vegas, NV, USA, Nov. 2016

Qi Shen, V. Palmre, J. Lee, K. J. Kim, “A Physics Model of the Multi-Degree Freedom Ionic Polymer-Metal Composite Cylinder Actuator”, in *Proceedings of the SPIE Behavior and Mechanics of Multifunctional Materials and Composites 2016*, San Diego, CA, USA, Apr. 2016. DOI: 10.1117/12.2220440

Z. Cook, L. Zhao, J. Lee, W. Yim, “Unmanned Aerial Systems for First Responders”, in *Proceedings of the 12th International Conference on Ubiquitous Robots and Ambient Intelligence 2015*, Goyang, Republic of Korea, Oct. 2015. DOI: 10.1109/URAI.2015.7358959

Z. Cook, L. Zhao, J. Lee, W. Yim, “Unmanned Aerial Vehicle for Hot-spot Avoidance with Stereo FLIR Cameras”, in *Proceedings of the 12th International Conference on Ubiquitous Robots and Ambient Intelligence 2015*, Goyang, Republic of Korea, Oct. 2015. DOI: 10.1109/URAI.2015.7358962

Professional Affiliations & Activities:

National Society of Professional Engineers	Member since 2017
American Nuclear Society	Member since 2016
Nevada State Board of Professional Engineers and Land Surveyors	Certified: May 17, 2013
Classification – Engineer Intern (EI) (Cert. Number 0T7123)	
<i>Phi Kappa Phi</i> – Honors Society	Inducted Apr. 22, 2013
<i>Tau Beta Pi</i> – The Engineering Honors Society	Inducted Dec. 3, 2011

Honors and Funding:

- National Science Foundation (NSF) Partnerships for International Research and Education (PIRE) 2017 Fellowship Jul. 2017
- Savannah River Nuclear Solutions, LLC contract No. 0000217400 Jan. 2017 - present
- Spring 2017 UNLV Differential Fees Tuition Scholarship Jan. 2017
- National Science Foundation (NSF) and National Research Foundation of Korea (NRF) EAPSI 2016 Fellowship Jun. 2016
- National Science Foundation (NSF), Partnerships for Innovation (PFI) Program, Grant No. 1430328 Jan. 2014 – Dec. 2017
- Nevada NASA Space Grant Consortium 2015 Fellowship Jan. 2015
- Nevada Professional Facility Managers Association Scholarship Jan. 2015